


Spring 2019

# Effect of Alkali on the Efficiency and Reliability of Cu(In,Ga)Se<sub>2</sub> Solar Cells

Shankar Karki

*Old Dominion University*, shankarjung@gmail.com

Follow this and additional works at: [https://digitalcommons.odu.edu/physics\\_etds](https://digitalcommons.odu.edu/physics_etds)

 Part of the [Materials Science and Engineering Commons](#), and the [Physics Commons](#)

---

## Recommended Citation

Karki, Shankar. "Effect of Alkali on the Efficiency and Reliability of Cu(In,Ga)Se<sub>2</sub> Solar Cells" (2019). Doctor of Philosophy (PhD), dissertation, Physics, Old Dominion University, DOI: 10.25777/q1y5-zw05  
[https://digitalcommons.odu.edu/physics\\_etds/99](https://digitalcommons.odu.edu/physics_etds/99)

This Dissertation is brought to you for free and open access by the Physics at ODU Digital Commons. It has been accepted for inclusion in Physics Theses & Dissertations by an authorized administrator of ODU Digital Commons. For more information, please contact [digitalcommons@odu.edu](mailto:digitalcommons@odu.edu).

**EFFECT OF ALKALI ON THE EFFICIENCY AND  
RELIABILITY OF Cu(In,Ga)Se<sub>2</sub> SOLAR CELLS**

by

Shankar Karki  
B.Sc., Tribhuvan University, Nepal  
M.S., Old Dominion University

A Dissertation Submitted to the Faculty of  
Old Dominion University in Partial Fulfillment of the  
Requirements for the Degree of

DOCTOR OF PHILOSOPHY

PHYSICS

OLD DOMINION UNIVERSITY  
May 2019

Approved by:

Desmond Cook (Co-Director)

Sylvain Marsillac (Co-Director)

Colm T. Whelan (Member)

Gon Namkoong (Member)

Sebastian Kuhn (Member)

# ABSTRACT

## EFFECT OF ALKALI ON THE EFFICIENCY AND RELIABILITY OF $\text{Cu}(\text{In,Ga})\text{Se}_2$ SOLAR CELLS

Shankar Karki

Old Dominion University, 2019

Co-Directors: Dr. Desmond Cook

Dr. Sylvain Marsillac

The incorporation of alkali metal has contributed tremendously in a bid to realize greater than 20% efficient  $\text{Cu}(\text{In,Ga})\text{Se}_2$  (CIGS) solar cells. Achieving high efficiency is one key parameter for the success of a photovoltaic technology but so is its long-term stability. In this thesis, the relationship between the performance of alkali treated  $\text{Cu}(\text{In,Ga})\text{Se}_2$  solar cells and their physicochemical, electronic and structural properties are explored through a comparative study between standard devices and alkali (K, Rb) treated devices. The alkali treated devices tend to have a lower concentration of  $E_v+0.98$  eV trap, higher majority carrier concentration and improved minority carrier lifetime, contributing to the experimentally observed improvement in open circuit voltage. Critical changes in alkali elemental profile occur throughout the film, while no other major physicochemical or structural properties are modified. Furthermore, we explored the long-term stability of CIGS solar cells due to damp heat treatment. We specifically study the influence on the molybdenum back contact and the CIGS absorber layer itself, with an emphasis on the role played by sodium. Molybdenum thin films showed drastic micro-structural, surface morphology, electrical and optical properties deterioration leading to the degradation of the solar cell performance. In the case of bare CIGS thin films, we observed surface oxidation and degraded electronic properties, also leading to degradation of solar cell performance. In both cases, alkali migration is responsible for the most part of the degradation, along with surface oxidation.

Copyright, 2019, by Shankar Karki, All Rights Reserved.

## ACKNOWLEDGEMENTS

I would like to thank my co-advisor Dr. Sylvain Marsillac for giving me the opportunity to do my Ph.D. thesis in his research group. I highly appreciate his support, guidance, and freedom to work on this project.

I am very thankful to the dissertation committee: Dr. Colm Whelan, Dr. Desmond Cook, Dr. Gon Namkoong, and Dr. Sebastian Kuhn.

I would like to thank all the present and former research group members for their support in this work. I especially would like to thank Grace Rajan for her support in both research and personally. I am also grateful for the staff (Lisa Okun, Delicia Malin, Annette Guzamn-Smith and Romina Samson) for their help and support.

I would like to thank our collaborators Dr. Angus Rockett at Colorado School of Mines, Dr. Robert Collins from the University of Toledo, Dr. Aaron Arehart and Dr. Tyler Grassman from The Ohio State University. I highly appreciate the help from Pran Paul for DLTS/DLOS measurements, Julia Deitz and Sina Soltanmohammad for STEM measurements, Dr. Evgeny Danilov for PL/TRPL measurements and Dr. Wei Cao for training me on XRD, AFM, and SEM measurements.

I am grateful to my family and my friends for their continuous support and help. I am indebted to my uncle and aunt, Prem Dhoj Karki and Kamala Karki, for their support and assistance throughout my educational career. Finally, I would like to thank my wife, Gandhari Bhandari, for her understanding and care.

## TABLE OF CONTENTS

	Page
LIST OF TABLES .....	vii
LIST OF FIGURES .....	xiii
Chapter	
1. INTRODUCTION .....	1
1.1 PHOTOVOLTAIC TECHNOLOGY .....	1
1.2 EFFICIENCY IMPROVEMENT IN CIGS SOLAR CELLS .....	2
1.3 RELIABILITY ISSUES IN CIGS SOLAR CELLS .....	4
1.4 THE SCOPE OF THIS THESIS .....	5
2. THEORITICAL BACKGROUND .....	7
2.1 PN JUNCTION .....	7
2.2 CURRENT VOLTAGE CHARACTERISTICS OF A SOLAR CELL .....	9
2.3 GENERATION AND RECOMBINATION .....	13
2.4 CIGS SOLAR CELLS DEVICE STRUCTURE .....	18
3. SAMPLE PREPARATION AND CHARACTERIZATION METHODS .....	26
3.1 SAMPLE PREPARATION .....	26
3.2 CHARACTERIZATION METHODS .....	28
4. KF POST DEPOSITION TREATMENT ON CIGS SOLAR CELLS .....	33
4.1 EXPERIMENTAL DETAILS .....	35
4.2 RTSE ANALYSIS OF CIGS FILMS BEFORE AND AFTER KF PDT .....	35
4.3 COMPOSITION AND ELEMENTAL DISTRIBUTION .....	40
4.4 FORMATION OF DEFECT LEVELS .....	44
4.5 DEVICE RESULTS .....	49
4.6 SUMMARY .....	53
5. RbF POST DEPOSITION TREATMENT IN CIGS SOLAR CELLS .....	55
5.1 EXPERIMENTAL DETAILS .....	56
5.2 COMPOSITION AND ELEMENTAL DISTRIBUTION .....	57
5.3 DEVICE RESULTS .....	59
5.4 CHARACTERIZATION OF DEEP LEVEL TRAPS .....	62
5.5 PHOTOLUMINESCENCE MEASUREMENT .....	66
5.6 SCAPS SIMULATION RESULTS .....	67
5.7 SUMMARY .....	69

6. IMPACT OF DAMP HEAT STRESS ON MOLYBDENUM BACK CONTACT.....	70
6.1 SAMPLE PREPARATION .....	71
6.2 CHARACTERIZATION OF Mo THIN FILM ON SLG SUBSTRATE .....	72
6.3 EFFECTS OF Mo DEGRADATION IN CIGS FILM.....	76
6.4 SOLAR CELL DEVICE RESULTS .....	84
6.5 SUMMARY .....	87
7. IMPACT OF DAMP HEAT STRESS ON CIGS THIN FILM .....	88
7.1 SAMPLE PREPARATION .....	89
7.2 MATERIAL CHARACTERIZATION .....	90
7.3 SOLAR CELL DEVICE RESULTS .....	100
7.4 SUMMARY .....	103
8. CONCLUSIONS .....	104
REFERENCES.....	106
APPENDICES	
A. ....	125
VITA.....	131

## LIST OF TABLES

Table	Page
1. Highest reported efficiency for different kinds of solar cells [4] . . . . .	2
2. Coefficient of thermal expansion and the density of the substrate materials used in CIGS solar cell[85]. . . . .	21
3. The elemental composition of the CIGS thin films deposited on Mo coated alumina substrate with and without KF PDT from XRF measurement. . .	41
4. The elemental composition of the CIGS thin films deposited on Mo coated SLG substrate with and without KF PDT from the XRF measurement. . .	43
5. Best cell parameters of the CIGS solar cells with and without KF PDT prepared on SLG with anti-reflective coating. . . . .	52
6. The elemental composition of the CIGS film with and without RbF PDT from XRF measurement. . . . .	58
7. Photovoltaic characteristics of the best cell studied in this experiment. . . .	60
8. Parameters used in the SCAPS simulation . . . . .	68
9. Summary of the CIGS samples used in this study. . . . .	72
10. Calculated CIGS film texture from XRD measurement. . . . .	78
11. J-V parameters of a representative solar cell device from each catagory listed in Table 9. . . . .	86



## LIST OF FIGURES

Figure	Page
1. Schematic diagram of energy band of a (a) P-type semiconductor, (b) N-type semiconductor and (c) the PN-junction at equilibrium. This image is motivated from reference [80]. . . . .	7
2. Schematic of (a) the charge distribution and (b) electric field of an abrupt pn-junction. This image is adopted from reference [80]. . . . .	8
3. An equivalent circuit diagram of a solar cell. . . . .	10
4. Spectral irradiance for AM0, AM1.5 Global and AM1.5 Direct solar spectrum after reference [81]. . . . .	11
5. A typical current-voltage curve (I-V) and power-voltage (P-V) curve of a solar cell. . . . .	13
6. Schematic diagram of the trap assisted non-radiative recombination, band to band recombination and the auger recombination [81]. . . . .	15
7. Schematic diagram of Shockley Read Hall recombination process in semiconductor. . . . .	17
8. Schematic diagram of a typical CIGS solar cell device. . . . .	19
9. Band diagram of a CIGS solar cell device. . . . .	19
10. A unit cell of the Cu(In,Ga)Se <sub>2</sub> crystal lattice based on reference [79]. . . . .	22
11. A pseudo-binary Cu <sub>2</sub> Se- In <sub>2</sub> Se <sub>3</sub> equilibrium phase diagram based on reference [98]. . . . .	23
12. Lattice constant versus bandgap for some I-III-VI <sub>2</sub> compounds [81]. . . . .	24
13. The evolution of $\Psi$ parameter measured by ellipsometer as a function of deposition time (black) and the substrate temperature change during the CIGS deposition(red) [36]. . . . .	36
14. Schematic of the optical models for a) the IGS film in stage 1; b) IGS to CIGS conversion, Cu <sub>2-x</sub> Se formation and Cu <sub>2-x</sub> Se to CIGS conversion in stage 2 and 3; c) the CIGS before and after KF PDT at 350°C [36]. . . . .	38
15. Bulk thickness (black) and surface roughness thickness(red) of CIGS deduced from RTSE as a function of time [36]. . . . .	38

16.	Dielectric function of the CIGS film before and after KF PDT [36]. . . . .	39
17.	The bandgap of the CIGS thin film extracted from the ellipsometry analysis. Absorption coefficient as a function of photon energy is shown in the insert. . . . .	40
18.	Elemental depth profile of the CIGS film prepared on alumina/Mo substrate with no post deposition alkali halide treatment measured by SIMS [73]. . . . .	41
19.	Elemental depth profile of the CIGS film prepared on alumina/Mo substrate with KF post deposition treatment measured by SIMS [73]. . . . .	42
20.	Elemental depth profile of the CIGS film prepared on SLG/Mo substrate without KF post deposition treatment measured by SIMS [36]. . . . .	43
21.	Elemental depth profile of the CIGS film prepared on SLG/Mo substrate with KF post deposition treatment measured by SIMS [36]. . . . .	44
22.	Comparison of DLTS spectra of CIGS sample with and without KF PDT deposited on alumina/Mo substrate [73]. . . . .	45
23.	Comparison of DLOS spectra of CIGS sample with and without KF PDT deposited on alumina/Mo substrate [73]. . . . .	45
24.	Comparison of DLTS spectra of CIGS sample with and without KF PDT deposited on SLG/Mo substrate [36]. . . . .	46
25.	(a) Scanning-DLTS map and (b) topography image of the CIGS sample without KF PDT. (c) Scanning-DLTS map and (d) topography image of the CIGS sample with KF PDT. The two green lines represent the approximate area where the depletion region is modulated [36]. . . . .	47
26.	Comparison of DLOS spectra of CIGS samples with and without KF PDT deposited on SLG/Mo substrate [36]. . . . .	49
27.	Comparison of CIGS devices parameters with and without KF PDT prepared on alumina substrates without an anti-reflective coating. The overall gain in efficiency was observed in the KF treated samples mostly due to improvement in open circuit voltage and fill factor and a small increase in short circuit current. . . . .	50
28.	Comparison of external quantum efficiency in the CIGS devices with and without KF PDT prepared on alumina substrates. A small variation in EQE response in the 400 nm-500 nm range is due to the small variation in the CdS thickness. . . . .	50

29.	Comparison of a current density-voltage plot of the CIGS devices with and without KF PDT prepared on alumina substrates. The roll-over effect seen in the device without KF treatment is corrected after KF post-deposition treatment [73]. . . . .	51
30.	Comparison of device parameters in the CIGS devices with and without KF PDT prepared on SLG substrates after MgF <sub>2</sub> anti-reflective coating. . . . .	52
31.	Comparison of current density-voltage plot of the CIGS devices with and without KF PDT prepared on SLG substrates. The J-V curve shows the improvement in open-circuit voltage for the KF PDT sample [36]. . . . .	53
32.	Comparison of external quantum efficiency in the CIGS devices with and without KF PDT prepared on SLG substrates after MgF <sub>2</sub> anti-reflective coating. . . . .	53
33.	Elemental depth profile of the CIGS film prepared on SLG/Mo substrate with no post deposition alkali halide treatment measured by SIMS (reference sample) [74]. . . . .	58
34.	Elemental depth profile of the CIGS film prepared on SLG/Mo substrate with RbF post deposition treatment measured by SIMS [74]. . . . .	59
35.	Summary of the photovoltaic parameters of the device without (black) and with (red) RbF PDT[74]. . . . .	60
36.	Representative current density-voltage curves for the reference and the RbF treated CIGS device[75]. . . . .	61
37.	Representative external quantum efficiency curves of the reference and the RbF treated CIGS device [74]. . . . .	61
38.	Light temperature dependent J-V plot for reference device and the RbF treated device [74]. . . . .	62
39.	Doping concentration measured by C-V measurement on reference and RbF PDT devices[74]. . . . .	64
40.	Comparison of DLTS signal of the reference cell with RbF PDT CIGS solar cell. An E <sub>v</sub> +0.55 eV trap was observed in the reference cell, while a E <sub>v</sub> +0.57 eV trap was observed in the RbF treated cell [74]. . . . .	64
41.	Comparison of DLOS signal of the reference cell with RbF PDT CIGS solar cell. The E <sub>v</sub> +0.99 eV trap was observed in both samples [74]. . . . .	66

42.	TRPL decays for the reference sample (black square box) and the RbF treated sample (red circle). Dotted lines show the measured data while the solid lines show the corresponding single exponential fit to the decay curve [74]. . . . .	67
43.	The measured and simulated J-V curves of the reference and RbF treated CIGS solar cells [74]. . . . .	68
44.	The GIXRD pattern of the reference Mo film and the water-soaked Mo film (insert: XRD measurements). . . . .	73
45.	AFM images for the reference Mo (a) and water-soaked Mo (b). . . . .	74
46.	Model used to study the dielectric properties of the Mo film in the spectroscopic ellipsometry analysis. The surface roughness layer was modeled using the Bruggeman EMA with 50-50% Mo-voids. . . . .	75
47.	Dielectric function $\epsilon = \epsilon_1 + i\epsilon_2$ of the reference and the water-soaked Mo film. . . . .	76
48.	Reflectance of the reference and the water-soaked Mo film. . . . .	76
49.	The XRD pattern of the CIGS samples as listed in Table 9. . . . .	77
50.	STEM-HAADF image of the devices prepared on reference Mo (a) and water soaked Mo (b) on SLG substrate. . . . .	79
51.	The elemental distribution of Mo, O, Se and Na in oxidized Mo measured by EDS in STEM. . . . .	80
52.	Elemental distribution in the CIGS devices deposited on reference Mo ((a)-positive SIMS). . . . .	81
53.	Elemental distribution in the CIGS devices deposited on water-soaked Mo ((b)-positive SIMS). . . . .	81
54.	Elemental distribution in the CIGS devices deposited on reference Mo ((c)-negative SIMS). . . . .	82
55.	Elemental distribution in the CIGS devices deposited on water-soaked Mo ((d)- negative SIMS). . . . .	82
56.	Box plot of the CIGS devices in each category of the devices listed in Table 9. . . . .	84
57.	Dark J-V characteristics of a representative device with double diode model fit (symbols) from each category listed in Table 9. . . . .	85

58.	The reverse bias QE(-1V)/QE(0V) characteristics of a representative device from each category listed in Table 9. ....	86
59.	STEM-HAADF cross-section image of reference CIGS device.....	90
60.	STEM-HAADF cross-section image of CIGS device with water-soaked CIGS layer. ....	91
61.	Comparative XPS peak of Cu 2P <sub>3/2</sub> between reference (black) and water soaked (red) CIGS thin film. ....	92
62.	Comparative XPS peak of In 3d <sub>5/2</sub> between reference (black) and water soaked (red) CIGS thin film. ....	92
63.	Comparative XPS peak of Ga 2P <sub>3/2</sub> between reference (black) and water soaked (red) CIGS thin film. ....	93
64.	Comparative XPS peak of Se 3d between reference (black) and water soaked (red) CIGS thin film. ....	93
65.	Comparative XPS peak of O 1s between reference (black) and water soaked (red) CIGS thin film. ....	94
66.	Comparative XPS peak of Na 1s between reference (black) and water soaked (red) CIGS thin film. ....	94
67.	SIMS depth profile of Na <sup>+</sup> , K <sup>+</sup> and CsCs <sup>+</sup> in reference CIGS layer. ....	95
68.	SIMS depth profile of Na <sup>+</sup> , K <sup>+</sup> and CsCs <sup>+</sup> in the water soaked CIGS layer. ....	96
69.	DLTS spectra comparison of CIGS water soaked solar cell and reference solar cell from 100K to 365K. The concentration of E <sub>v</sub> +0.65 eV trap is ≈ 2.5 times higher in CIGS water soaked solar cell [184]. ....	97
70.	Comparison of the DLOS spectra of the reference cell and WS CIGS solar cell [184]. ....	97
71.	PL spectrum of CIGS/CdS junction of the reference and the water soaked CIGS.....	98
72.	TRPL dynamics of the reference (left) and the water soaked CIGS(right). ....	99
73.	Comparison of the device characteristics of the water-soaked CIGS film with the reference device. ....	100

74. Temperature dependence of the open circuit voltage for the WS sample and the reference sample (Insert: Dark current-voltage curve for a water-soaked sample measured in the temperature range  $-70^{\circ}\text{C}$  to  $80^{\circ}\text{C}$ )..... 101
75. Representative current density versus voltage curve of the reference and water-soaked CIGS solar cell device. .... 101
76. Representative external quantum efficiency curves for the reference and water-soaked CIGS solar cell. .... 102

# CHAPTER 1

## INTRODUCTION

### 1.1 PHOTOVOLTAIC TECHNOLOGY

Solar energy in the form of heat (solar thermal) or photovoltaics (PV) is one of the best sources of renewable energy in terms of availability, cost effectiveness, accessibility, capacity and efficiency to meet the increasing global energy demand [1]. Photovoltaics refers to the direct conversion of sunlight into electricity. According to the Renewables 2018 Global Status Report [2], the PV industry is growing fast globally every year. About 98 GW (in direct current) of solar PV was installed both on and off the grid in 2017, with a cumulative total of approximately 402 GW by the end of the same year. The cost competitiveness of PV together with a growing demand for clean energy was identified as main contributors for this success. Cost efficient PV requires high power conversion efficiency and low production cost. Silicon-based photovoltaics currently has the largest share of the solar cell market [3]. Although crystalline-Si (c-Si) based solar cells have high power conversion efficiency [see Table 1] (after [4]), further cost reduction requires minimizing production cost, which needs to overcome limitations of the existing technology [5, 6, 7]. Alternatively, there is a growing interest in thin film solar cells based on materials such as amorphous silicon (a-Si), cadmium telluride (CdTe), copper indium gallium selenide (Cu(In,Ga)Se<sub>2</sub> or CIGS) due to their favorable low cost and high-efficiency [8, 9, 10]. These three materials are direct bandgap semiconductor with a high optical absorption coefficient compared to indirect bandgap materials, such as c-Si, so that less material needs to be used to absorb most of the sunlight. Besides the use of much less material, thin film solar cells offer roll to roll manufacturing capability on flexible substrates (such as metal foil, plastics, etc.) which allows them to be suitable for applications such as building integrated photovoltaics.

TABLE 1: Highest reported efficiency for different kinds of solar cells [4]

Technology	Efficiency(%)	Cell Area (cm <sup>2</sup> )
Si (crystalline cell)	26.7 ± 0.5	79.0
Si (multicrystalline cell)	22.3 ± 0.4	3.923
GaAs (thin film cell)	28.8 ± 0.9	0.9927
CIGS (cell)	22.9 ± 0.5	1.041
CdTe (cell)	21.0 ± 0.4	1.0623
Si (amorphous cell)	10.2 ± 0.3	1.001
Perovskite (cell)	20.9 ± 0.7	0.991

## 1.2 EFFICIENCY IMPROVEMENT IN CIGS SOLAR CELLS

Among the commercial thin-film technology, CIGS is the most efficient solar cell technology with record power conversion efficiency of 22.9% [4]. The quality of the CIGS absorber layer and the interfacial properties in the multilayer structure of CIGS solar cell play a crucial role in the performance of the solar cell. For CIGS growth, many vacuum and non-vacuum methods have been applied [9, 11, 12]. The suitable addition of Ga across the CIGS film thickness, on the one hand, is key to achieving high efficiency, the other being alkali metal addition. The band gap of CIGS can be tuned between 1.02 eV (CuInSe<sub>2</sub>) to 1.67 eV (CuGaSe<sub>2</sub>) depending on the Ga concentration. The adjustable bandgap (1.02 eV-1.67 eV) of CIGS makes it an attractive candidate for tandem devices (two junctions). Recently, record efficiency of 18% with a narrow bandgap of 1.02 eV CIGS has been demonstrated and applied as a low bandgap partner in the perovskite/CIGS four terminal tandem configuration [13]. Theoretical calculations show that the ideal bandgap of single junction CIGS device for maximum efficiency under AM1.5 spectrum is 1.4 eV [14]. However, the highest efficiency CIGS solar cells have been obtained at the bandgap of about 1.15 eV, which corresponds to gallium to gallium plus indium ratio of  $\approx 0.3$  [12, 15]. It has been experimentally challenging to obtain a good CIGS solar cell with high gallium content since the open circuit voltage does not increase proportionally to the increase in bandgap energy and degradation of the fill factor occurs with the increase in gallium content. The performance loss in the wide bandgap CIGS is linked to the deterioration of material quality, recombination losses, increase in mid-band gap



defect states and increase in band offset at the CdS/CIGS interface, leading to interfacial recombination [16, 17, 18]. Bandgap engineering in the form of double gallium grading with the average bandgap of  $\approx 1.15$  eV within the CIGS film thickness is commonly applied [12, 19] to obtain a highly efficient CIGS solar cell devices. The advantage of back grading is the creation of a back surface field, which assists in the drift of the minority carrier towards the front junction, while the front grading enhances the junction quality [20, 21]. The carrier collection efficiency can also be enhanced due to the double gallium grading since a bandgap minimum exists in the graded profile permitting absorption of photons in the infrared region of the solar spectrum. However, a drastic change in the gallium notch is suggested to act as a detrimental recombination region that induces a strong barrier for electrons, especially in the forward bias case, resulting in a performance loss [20].

Besides bandgap engineering, incorporation of alkali species in the CIGS absorber layer is very crucial for high performing CIGS solar cells. Historically, the diffusion of Na from the soda lime glass (SLG) substrate was found to promote the device performance of the CIGS solar cells in the early nineties [22]. Since then, not only Na diffusion from SLG but pre-deposition and post-deposition incorporation of Na after CIGS growth has been reported to enhance the device performance [23, 24, 25, 26]. A diffusion barrier such as aluminum oxide, silicon dioxide or silicon nitride is sometimes used on SLG glass substrate to prevent the Na diffusion and allows to apply a controlled amount of sodium in the CIGS film, using sodium containing precursor such as NaF [24, 27]. Na was found to influence the structural, optical and electronic properties of CIGS films [25, 27, 28, 29]. There are contradicting reports on the role of sodium on the grain growth of CIGS. Some studies have shown that the presence of Na during CIGS deposition promotes the growth of larger grains [24, 30] with modified film texture, while other study show different behaviors [25, 26, 31]. The composition investigations show that Na primarily resides at the grain boundaries; however, a small amount was found in the grain interiors [32, 33, 34]. Elemental depth profiling has shown higher concentrations of Na in the front and the back interfacial regions of the CIGS films [35, 36, 37]. Although a direct link between microstructural changes due to Na for enhanced performance has not been well established, an improvement in the electronic properties of the CIGS films with Na incorporation has been clearly demonstrated [24, 25, 38]. Sodium mainly increases the p-type conductivity of the CIGS film and leads to increased open circuit voltage and fill factor. To explain the

increase in p-type conductivity, several mechanisms have been put forward. One argument is that Na passivates at the grain boundaries donor like defects such as  $\text{In}_{\text{Cu}}$  or promotes the formation of  $\text{O}_{\text{Se}}$  reducing Se vacancies which are active donors [39]. It is also argued that Na occupies the Cu vacancies ( $V_{\text{Cu}}$ ), responsible for p-type conductivity, at the grain boundaries inhibiting the formation of compensating  $\text{In}_{\text{Cu}}$  defects [39, 40]. This argument is supported by the presence of sodium mostly at the grain boundaries. The second mechanism is the direct creation of acceptors, such as  $\text{Na}_{\text{In}}$  anti-site defects [41]. Yuan et al. [42] proposed the formation of  $\text{Na}_{\text{Cu}}$  defects at high temperature followed by out-diffusion of Na during cooling and water rinsing, which leads to the formation of high concentration of Cu vacancies,  $V_{\text{Cu}}$ . Until recently, Na incorporation in the CIGS film was observed to be the best compared to the other alkali (Li, K, Cs) [24, 43]. However, a breakthrough was made with additional heavier alkali metal (K, Rb, Cs) incorporation in the form of post-deposition treatment (PDT) resulting in successive record efficiency CIGS devices [4, 44, 45]. While sodium was found to modify mainly bulk electronic properties (increased hole concentration, grain boundaries passivation, decreased trap concentration, enhanced minority carrier lifetime, increase in diffusion length), heavier alkali metals  $M=(\text{K}, \text{Rb}, \text{Cs})$  post-deposition treatment show additional significant surface modification [44, 46, 47, 48]. The improved junction due to heavier alkali metals has allowed reducing the CdS (hetero-junction partner) thickness without loss of device performance [12, 45]. It has been argued that the depletion of Cu due to KF PDT promotes the diffusion of Cd to occupy the Cu vacancy acceptors and form  $\text{Cd}_{\text{Cu}}$  donor during the deposition of the CdS layer by chemical bath deposition, creating a buried homo-junction and improving the junction quality. Several publications have indicated the formation of an alkali- $\text{In}_x\text{Se}_y$  layer at the surface of CIGS with respective heavier alkali PDT, which have higher bandgap compared to CIGS [49], thus reducing the interface recombination velocity [46, 50, 51, 52]. Furthermore, the lighter alkali metals were found to decrease after the heavier alkali metal incorporation [45, 48].

### 1.3 RELIABILITY ISSUES IN CIGS SOLAR CELLS

Device stability of the alkali incorporated CIGS devices under various stressors such as heat, light, moisture, electrical bias, etc. that come into play during the working condition in the field is a vital concern for the PV module reliability [53, 54, 55, 56, 57, 58, 59, 60, 61, 62]. Out of the various stressors, here we focus our

attention on the behavior of alkali when the CIGS thin film and solar cell undergo damp heat treatment. Studies show that the oxidation of bare CIGS film at elevated temperature is less detrimental than the oxidation in the humid air at room temperature in terms of their electrical performance [63]. It was also reported that the more oxidized species of Se or elemental Se and less In and Ga oxides were found in the CIGS containing Na compared to the Na less CIGS when they were exposed to the humid air [63]. In the same study, H<sub>2</sub>O catalyzed reaction was proposed for the incomplete oxidation of Na<sub>2</sub>Se<sub>x</sub> as well as the partial oxidation of the elemental Se to support the experimental observation. In another study, the formation of Na-O-CIGS complex was reported to be induced by H<sub>2</sub>O [64], but no solar cell device results were presented. The vacuum oxidation of CIGS surfaces was reported to mainly contain the oxides of In or Ga elements and SeO<sub>2</sub> in a lesser amount, but the thermal and native oxidation also contained additional Na<sub>x</sub>O and Na<sub>2</sub>CO<sub>3</sub> [65]. The reduction of minority carrier lifetime was observed in the air exposed bare CIGS film [66, 67]. Reference [68] reported Na migration caused the degradation in the CIGS device. CIGS device containing comparatively higher Na content was reported to show more noticeable degradation due to damp heat exposure (85% relative humidity at 85°C). A more recent study showed higher initial power conversion efficiency in the CIGS device containing a relatively higher amount of (Na, K), but unfortunately, the same device showed rapid degradation in the performance under exposure of damp heat and illumination [56]. The physical defects in the form of sodium rich spots in the device surface were observed in the degraded devices, which was concluded to form due to Na ion migration via grain boundaries [56, 69].

#### 1.4 THE SCOPE OF THIS THESIS

The objectives of this work are to expand the knowledge base on the alkali effect in the CIGS thin film and solar cells. As discussed in the previous section, progress in conversion efficiencies of CIGS-based device was driven by incorporation of alkali metals (Na, K, Rb, Cs). However, the mechanism behind the alkali treatment is not well understood yet. Here we apply multiscale optoelectronic, chemical and physical characterizations to understand the effects of potassium and rubidium post-deposition treatment in the CIGS thin films and devices.

On the other hand, alkali metals are also identified as participating in the device instability under the influence of stressors such as humidity, voltage bias, and light

bias [53, 54, 70, 71, 72]. Therefore, changes in the properties of the molybdenum and CIGS thin film under damp heat condition were assessed, and their subsequent effect on the device degradation analyzed. Particular attention was paid to the role of sodium in such degradation characteristics.

This thesis is organized as follows: In chapter 2, we present an overview of the basic device physics of a PN-junction diode and use it to explain the working principle of photovoltaic devices. The key metric used to characterize the photovoltaic properties will also be introduced. Furthermore, we discuss the device structure of the Cu(In,Ga)Se<sub>2</sub> solar cell. In chapter 3, the experimental details of Cu(In,Ga)Se<sub>2</sub> solar cell fabrication is presented, and the various characterization methods used in this thesis are briefly explained. Within chapter 4, we describe the application of a very specific tool we use, real-time in-situ ellipsometry(RTSE), for process monitoring of three-stage deposition of Cu(In,Ga)Se<sub>2</sub> thin films. We then describe the various characterization results on KF post-deposition effects on the CIGS thin films and devices. This chapter is based on the publications in references [36, 73]. In chapter 5, the effects of RbF post-deposition treatment on the electronic properties and composition of Cu(In,Ga)Se<sub>2</sub> thin films and solar cells are presented. This chapter is based on the publications in references [74, 75]. Chapter 6 and chapter 7 covers the damp heat stress of molybdenum back contact and Cu(In,Ga)Se<sub>2</sub> absorber layer and their effects on the photovoltaic performance of the Cu(In,Ga)Se<sub>2</sub> solar cell devices, respectively. Some of the results in chapter 6 and chapter 7 have been reported in the conference proceedings in references [76, 77].

## CHAPTER 2

### THEORITICAL BACKGROUND

In this chapter, the solar cell device physics will be briefly reviewed followed by a brief introduction of the CIGS solar cell device structure. The function of each layer and commonly used materials for the various layer in the multilayer CIGS solar cell devices are presented. Nelson’s “The Physics of Solar Cells” [78] and Luque’s “Handbook of Photovoltaic Science and Engineering” [79] are valuable resources for further information.

#### 2.1 PN JUNCTION

The PN-junction and associated characteristics provide a basis of operation of the solar cells. A PN-junction is established by contacting an N-type semiconductor with a P-type semiconductor. A P-type (N-type) semiconductor is formed by doping pure (intrinsic) semi-conductor with acceptor atoms (donor atoms). If the N-type and P-type semiconductor are made up of the same material, the junction is a homo-junction. However, if the N-type and P-type semiconductor are made up of dissimilar materials, the junction is a hetero-junction. In the case of hetero-junctions, the energy bandgap of the materials in contact is different.

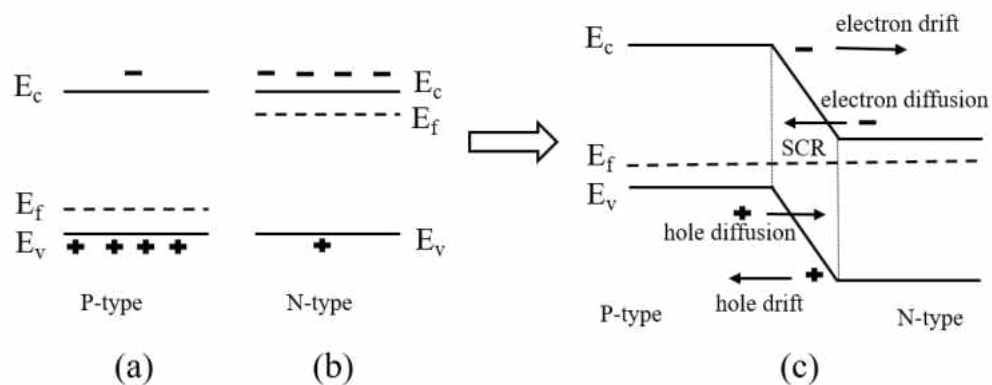


FIG. 1: Schematic diagram of energy band of a (a) P-type semiconductor, (b) N-type semiconductor and (c) the PN-junction at equilibrium. This image is motivated from reference [80].

When a junction is formed, the charge carriers diffuse across the junction. In particular, electrons diffuse from N-side to P-side leaving behind a positively charged ionized atoms and holes diffuse from P-side to N-side leaving behind a negatively charged ionized atoms. Consequently, a negative space charge forms near the P-side and a positive space charge forms near the N-side, both of which are lacking free mobile charges. This is known as the depletion region or the space charge region (SCR) as shown in Figure 1. Due to the charge displacement, an electrostatic field sets up which opposes the diffusion of the charge carriers across the junction. A schematic of the charge distribution and the electric field of an abrupt PN-junction is shown in Figure 2. When the diffusion of majority carriers is balanced by the drift of the minority charge carriers (due to the built-in electrostatic field), an equilibrium is established. At this point, the fermi level throughout the sample is constant. Subsequently, an internal built-in potential ( $V_{bi}$ ) is established at the junction, which is given by equation (1)[80],

$$V_{bi} = \frac{kT}{q} \ln \left( \frac{N_A N_D}{n_i^2} \right) \quad (1)$$

where  $N_{A,D}$  is the acceptor and donor concentration in the P-type and N-type semiconductor respectively,  $n_i$  is intrinsic carrier concentration,  $k$  is Boltzmann constant,  $T$  is the temperature and  $q$  is the electronic charge.

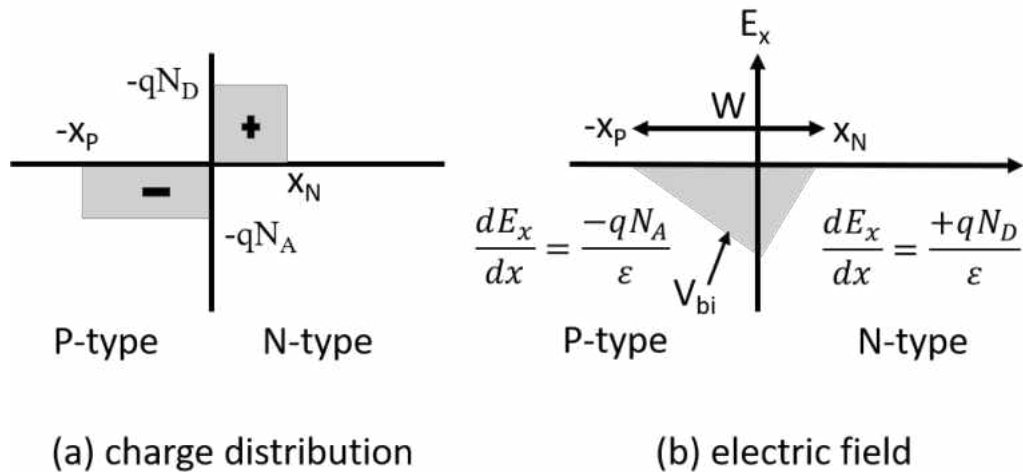


FIG. 2: Schematic of (a) the charge distribution and (b) electric field of an abrupt pn-junction. This image is adopted from reference [80].

And the width of the depletion region as a function of  $V_{bi}$  is given by equation(2),

$$W = |l_n| + |l_p| = \sqrt{\frac{2\epsilon}{q} \left( \frac{1}{N_A} + \frac{1}{N_D} \right)} \quad (2)$$

where  $\epsilon$  is the permittivity of the semiconductor material.

In the absence of externally applied voltage, there is no net current flowing across the PN-junction because the diffusion current and the drift current cancel each other for both types of carriers, electrons, and holes. By applying a forward bias, in which case the P-side of the diode is connected to the positive terminal, and the N-side of the diode is connected to the negative terminal of the voltage source, the potential barrier is reduced thereby increasing the diffusion currents of both holes and electrons. However, the drift current barely changes. On the other hand, by applying a reverse bias, the potential barrier is increased. In this case, the holes are pushed further back into the P-region and the electrons are pushed back into the N-region. The diffusion currents are greatly reduced, while the drift currents are unchanged and eventually reach a saturation value( $I_o$ ) due to increase in the electrostatic potential across the depletion region. The current voltage behavior of the PN-junction ideal diode is expressed by the well-known Shockley equation (3),

$$I = I_o \left( e^{\frac{qV}{kT}} - 1 \right) \quad (3)$$

where  $I_o$  is the reverse saturation current density expressed as in equation (4),

$$I_o = \frac{qD_n p_{po}}{L_n} + \frac{qD_p p_{no}}{L_p} \quad (4)$$

where,  $D_{n,p}$  is the diffusion coefficient for electrons and holes,  $L_{n,p}$  is the diffusion length of electrons and holes,  $n_{po}$  is the equilibrium electron density in the P-side and  $p_{no}$  is the equilibrium hole density in the N-side. When the reverse saturation current in the diode is small, it performs as a good rectifier.

## 2.2 CURRENT VOLTAGE CHARACTERISTICS OF A SOLAR CELL

A photovoltaic (or solar) cell converts the energy of light directly into the electricity. A solar cell is essentially a PN-junction which operates when illuminated with light. An equivalent circuit diagram of a solar cell is shown in Figure 3. The power conversion from sunlight to electricity by solar cell involves generation

of electron–hole (e–h) pairs due to absorption of incoming photons by the absorber layer, separation of these light-generated e-h pairs and the collection of these carriers by the external electrodes.

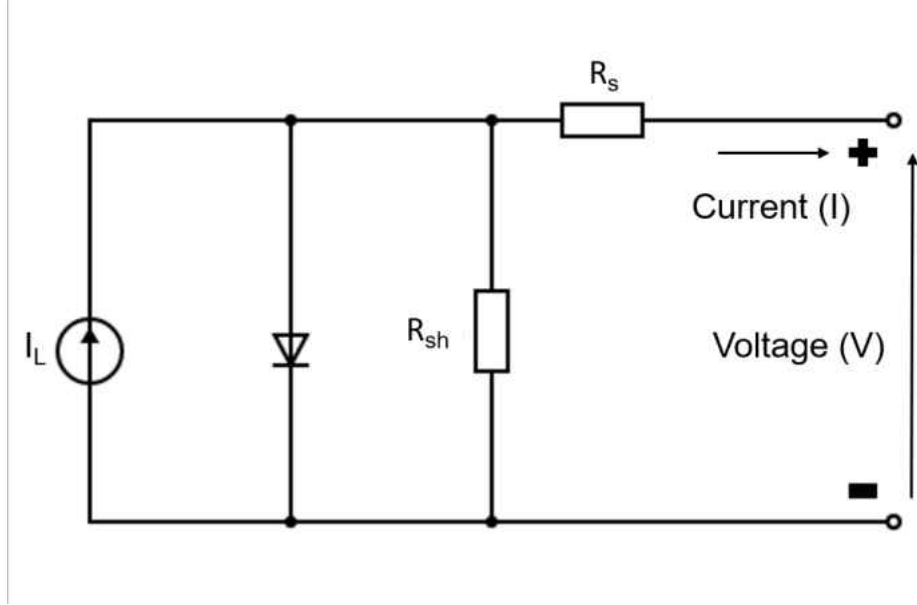


FIG. 3: An equivalent circuit diagram of a solar cell.

Current-voltage (I-V) characteristics of a solar cell are represented by the ideal diode equation shifted by the light generated current  $I_L$ . Including series resistance ( $R_s$ ) and shunt resistance ( $R_{sh}$ ), the solar cell equation takes the following form (equation (5)),

$$I = I_o \left( e^{\frac{q(V-IR_s)}{AkT}} - 1 \right) + \frac{V - IR_s}{R_{sh}} - I_L \quad (5)$$

where  $A$  is called the diode ideality factor. An ideal diode has  $A=1$ .

I-V characteristics of the solar cells are often used to compare the performance of different solar cells and therefore require references. The light I-V for a solar cell is obtained by using an illumination source with an approximately AM 1.5 Global (AM: air mass) spectrum having an intensity of  $100 \text{ mW/cm}^2$  at the temperature of  $25^\circ\text{C}$ . Three different types of solar spectrum are shown in Figure 4. The solar radiation outside the earth's atmosphere (AM0) differs slightly from the radiation seen at the earth's surface (AM1.5) due to absorption and scattering of photons of specific



wavelengths due to atmospheric species such as H<sub>2</sub>O, CO<sub>2</sub> and O<sub>3</sub> [78, 81]. Air mass calculations are used to quantify the power loss as the light passes through the atmosphere. Air mass is defined as the path length that light travels through the atmosphere to the surface of the earth and is expressed as in equation (6) by,

$$AM = \frac{1}{\cos(\theta)} \quad (6)$$

where,  $\theta$  is the angle of the sun's position with respect to its vertical (sun directly overhead). For example, when  $\theta$  is 48.2° with respect to earth's vertical,  $AM = 1.5$ . Since the efficiency of the solar cell is dependent on both the power and the spectrum of the intensity of light, the solar spectrum and the power density was standardized to facilitate for an accurate comparison. The standard spectrum at the earth's surface is AM1.5 Global which includes both direct and diffused radiation or AM1.5 Direct which includes direct radiation only. The power density for AM1.5 Global and AM0 are 1000 Watt/m<sup>2</sup> and 1366.1 Watt/m<sup>2</sup> respectively.

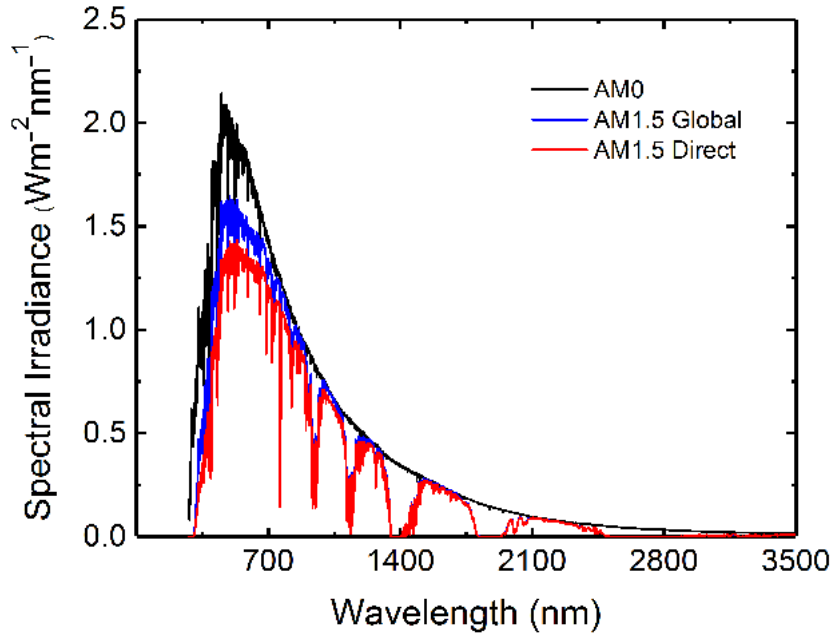


FIG. 4: Spectral irradiance for AM0, AM1.5 Global and AM1.5 Direct solar spectrum after reference [81].

A typical I-V curve of the solar cell is shown in Figure 5. The three important parameters in Figure 5 are the short circuit current ( $I_{sc}$ ), open circuit voltage ( $V_{oc}$ )

and the maximum power point ( $V_{mp}$ ,  $I_{mp}$ ). The short circuit current is the current of the solar cell under standard illumination when applied voltage goes to zero. If the series resistance is sufficiently low and shunt resistance is sufficiently high,  $I_{sc}$  is equivalent to the light generated current  $I_L$ , i.e.,  $I_{sc} \approx I_L$ . The photocurrent essentially depends on the bandgap of the absorber material, space charge width and transport properties [78]. The open circuit voltage ( $V_{oc}$ ) is the voltage between the terminals of the solar cell under standard illumination when current goes to zero. In an ideal case, the  $V_{oc}$  can be expressed as in equation (7) by,

$$V_{oc} \approx \frac{kT}{q} \ln \left( \frac{I_L}{I_o} + 1 \right) \quad (7)$$

This relation shows that variation in  $I_o$  which in turn depends on minority carrier densities, minority carrier lifetime, and carrier mobility as indicated by equation 4 causes the variation in  $V_{oc}$ . The Maximum Power Point ( $V_{mp}, I_{mp}$ ) represents the point at which the power generated is maximum. The Fill Factor (FF) of the solar cell which is a measure of the squareness of the I-V curve, is defined as in equation (8) by,

$$FF = \frac{V_{mp} \times I_{mp}}{V_{oc} \times I_{sc}} \quad (8)$$

The power conversion efficiency ( $\eta$ ) of a solar cell is the ratio of the output electric power divided by the input solar radiation power under standard test condition is defined by equation (9),

$$\eta = \frac{V_{mp} \times I_{mp}}{P_{in}} = \frac{FF \times V_{oc} \times J_{sc}}{P_{in}} \quad (9)$$

where  $P_{in}$  is the power density of the incident radiation which is equal to  $100 \text{ mW/cm}^2$  and  $J_{sc}$  is the short circuit current density which is the ratio of short circuit current ( $I_{sc}$ ) to the effective area of a solar cell under test.

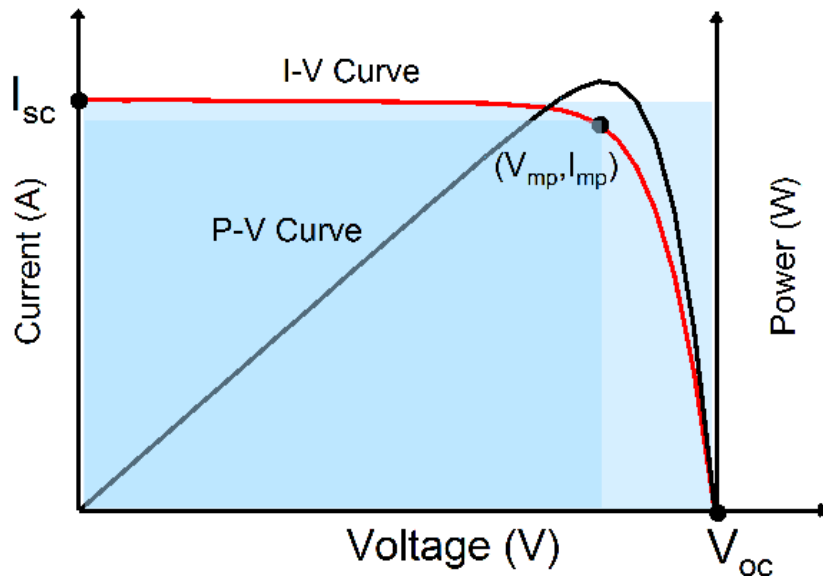


FIG. 5: A typical current-voltage curve (I-V) and power-voltage (P-V) curve of a solar cell.

## 2.3 GENERATION AND RECOMBINATION

Generation refers to the movement of an electron from the valence band to the conduction band in a semiconductor by creating an electron-hole pair; while in the recombination process, an electron drops from the conduction band to the valence band thereby annihilating an electron-hole pair [82]. These competing processes maintain the constant electron or hole concentration in a semiconductor at thermal equilibrium. In the presence of external factors such as illumination or applied voltage, generation and recombination processes act to bring the system back to an equilibrium.

### 2.3.1 GENERATION

Basically, there are four different types of generation processes namely impact ionization, thermal generation, impurity-mediated generation, and photo-generation [82]. Photo-generation is the most critical process in a solar cell, and involves the generation of electrons and holes by absorption of the incident photons with energy greater than the bandgap of the semiconductor. The probability of absorption of

a photon of energy  $E(\text{eV})$  depends on the material property, the absorption coefficient  $\alpha(E)$  ( $\text{cm}^{-1}$ ) which is related to the complex index of refraction through the extinction coefficient  $\kappa(\lambda)$  as in equation (10),

$$\alpha(\lambda) = \frac{4\pi\kappa(\lambda)}{\lambda} \quad (10)$$

where,  $\lambda$  is the wavelength (in cm) of the photon.

The absorption coefficient is higher in direct bandgap semiconductors such as GaAs, InP, CdTe, Cu(In,Ga)Se<sub>2</sub> [82]. In this class of semiconductors, the conduction band minimum and the valence band maximum are aligned in the energy- wave vector space. As a result, there is no change in crystal momentum from the initial state to the final state, so the photon can directly excite an electron from the valence band to the conduction band [78]. However, in the case of indirect bandgap semiconductors (such as Ge, Si), the valence band maximum and the conduction band minimum are not aligned in the energy-wave vector space. Thus, the excitation of an electron requires the participation of a phonon (particle of lattice vibration) in order to conserve the momentum. Therefore, the absorption coefficient of indirect bandgap semiconductor is low [78]. Assuming all the photons are absorbed to generate free carriers then the generation rate of electron-hole pairs per unit volume per second as a function of position within the solar cell is given by equation (11),

$$G(x) = \int_{\lambda} [1 - R(\lambda)] f(\lambda)\alpha(\lambda)e^{-\alpha(\lambda)x} d\lambda \quad (11)$$

where,  $R(\lambda)$  is the reflectivity of the surface to normally incident light of wavelength  $\lambda$ , and  $f(\lambda)$  is the incident photon flux (number of photons per unit area per second per wavelength) [78].

### 2.3.2 RECOMBINATION

The main recombination mechanisms in the photovoltaic device is radiative (band to band) recombination, non-radiative (Shockley-Read-Hall) recombination via trap state and auger recombination as illustrated in the Figure 6.

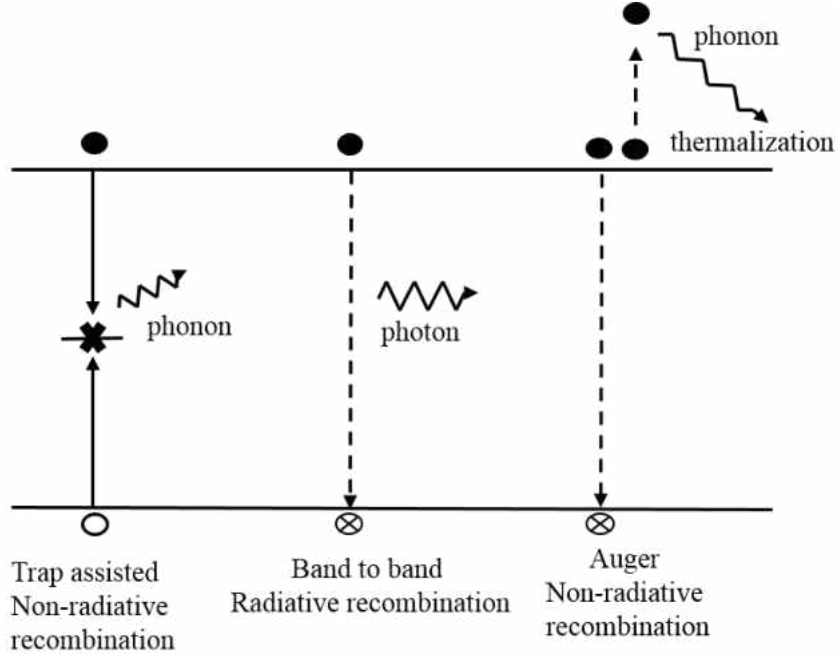


FIG. 6: Schematic diagram of the trap assisted non-radiative recombination, band to band recombination and the auger recombination [81].

### Radiative Recombination

In this recombination process, an electron drops from the conduction band to the valence band resulting in the emission of a photon. In a simplified case, (see [78]) the net recombination rate due to radiative process ( $R_{rad}$ ) is (equation 12),

$$R_{rad} = B (np - n_i^2) \quad (12)$$

where  $B$  is known as the radiative recombination coefficient and depends on the property of the material,  $n$  and  $p$  are the densities of electrons and holes in the non-equilibrium condition. In case of N-type material with a doping density  $N_D$  ( $n \approx n_o \gg p_o$ ), where  $n_o$  and  $p_o$  are the densities of electron and hole respectively at thermal equilibrium), when the excess electron-hole pair ( $\Delta n$  and  $\Delta p$ ) is significantly lower than the majority charge carrier,  $R_{rad}$  can be expressed as [82] (equation 13 and equation 15),

$$R_{rad} \approx B \Delta p N_D = \frac{p - p_o}{\tau_{p,rad}} \quad (13)$$

$$\tau_{p,rad} = \frac{1}{B N_D} \quad (14)$$

Similarly, for P-type material,

$$R_{rad} \approx B\Delta n N_A = \frac{n - n_o}{\tau_{n,rad}} \quad (15)$$

$$\tau_{n,rad} = \frac{1}{BN_A} \quad (16)$$

where  $N_A$  is the acceptor density in a P-type semiconductor. The net radiative recombination rate is proportional to excess minority carrier density. The radiative recombination coefficient  $B$  can be obtained from variation of  $\tau_{(p,rad)or(n,rad)}$  (electron and hole minority carrier radiative lifetime) with doping density.  $B$  is larger for the direct bandgap materials and the radiative lifetime is short. Thus, the radiative processes are much more crucial in the direct bandgap semiconductor.

### Auger Recombination

In this recombination process, the electron-hole pair recombines, and the energy of photogenerated carrier is imparted to another carrier, either a free electron near the conduction band edge or a free hole near the valence band edge which then relaxes through the process of thermalization as shown in the Figure 6. In the case of lower injection condition, the electron lifetime in P-type semiconductor ( $\tau_{(n,Aug)}$ ) and the hole lifetime in N-type material ( $\tau_{(p,Aug)}$ ) for Auger recombination is given as (equation (17) and equation (18)) [78],

$$\tau_{n,Aug} = \frac{1}{A_n N_A^2} \quad (17)$$

$$\tau_{p,Aug} = \frac{1}{A_p N_D^2} \quad (18)$$

The Auger process is most pronounced in materials with high carrier densities or at high temperature [78]. Auger recombination strongly depends on the doping density as shown by above equation (17) and (18).

### Non-radiative Recombination

Trap-assisted non-radiative recombination or Shockley Read Hall (SRH) recombination occurs through spatially localized defect or trap states within the bandgap of the bulk semiconductor. In this case, the excess energy is transferred to phonons. Trap states mainly serve to capture and emit either holes or electrons as shown in

Figure 7. Hole emission followed by electron emission generates an electron-hole pair. However, electron capture followed by hole capture recombines the electron-hole pair. The trap states which lie close to the middle of the bandgap are often called recombination centers because they capture both types of carriers.

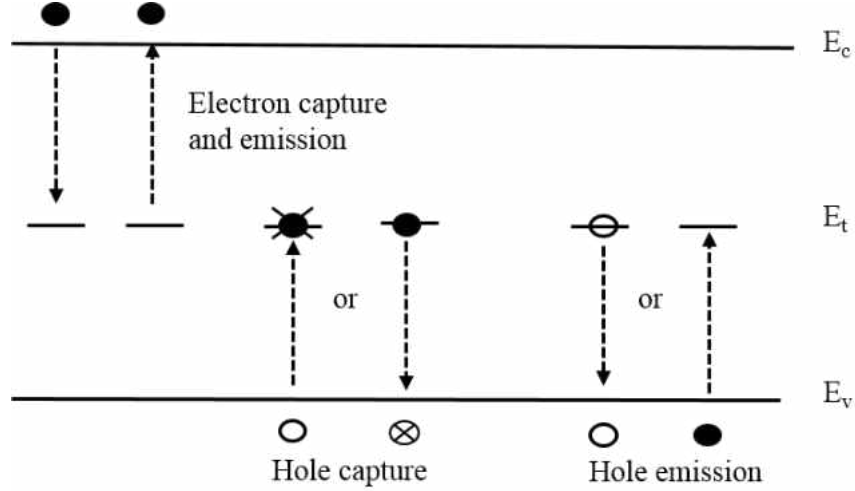


FIG. 7: Schematic diagram of Shockley Read Hall recombination process in semiconductor.

Based on SRH statistics (refer[83]), the net recombination rate through a single trap state can be written as (equation (19)),

$$R_{SRH} = \frac{pn - n_i^2}{\tau_p \left[ n + n_i e^{\left(\frac{E_t - E_i}{kT}\right)} \right] + \tau_n \left[ p + n_i e^{\left(\frac{E_i - E_t}{kT}\right)} \right]} \quad (19)$$

$$\tau_p = \frac{1}{N_t v_{th} \sigma_n} \quad (20)$$

$$\tau_n = \frac{1}{N_t v_{th} \sigma_p} \quad (21)$$

where,  $N_t$  is the density of trap,  $V_{th}$  is the thermal velocity of the charge carriers,  $\sigma_n$  and  $\sigma_p$  are the electron and hole capture cross-sections respectively.  $\tau_{n,SRH}$  and  $\tau_{p,SRH}$  defined by equation (20) and equation (21) are the electron and hole lifetimes. Equation (19) shows that when the difference between intrinsic energy level ( $E_i$ ) and trap energy level ( $E_t$ ) is small, the net recombination rate is maximized. Thus, the traps close to the middle of the bandgap are the most effective recombination centers. Similarly, the recombination in the semiconductor devices can occur at the interfaces

between the contacting layers such as back and front contacts of the solar cell. The semiconductor surfaces have a high concentration of defects because of the termination of the crystal lattice. The non-passivated interface defects introduce the energy levels within the forbidden gap of the semiconductor and enhance recombination.

## 2.4 CIGS SOLAR CELLS DEVICE STRUCTURE

The CIGS devices are manufactured almost exclusively in the substrate configuration in which the light travels via the top window layer to the absorber layer, where the electron-hole pairs are formed. Figure 8 shows the typical CIGS device structure. A corresponding band diagram is shown in Figure 9. A standard CIGS solar cell consists of the following layers in sequence: a piece of soda lime glass (SLG) used as substrate, Mo layer used as back contact, the CIGS absorber layer, CdS buffer layer (heterojunction partner), intrinsic ZnO, Al:ZnO (or  $\text{In}_2\text{O}_3:\text{Sn}$ ) transparent conducting oxide and Ni/Al/Ni grids used as a front contact. SLG is a commonly used substrate as it is thermally stable during high-temperature CIGS growth, chemically inert, has a matching coefficient of thermal expansion to CIGS and acts as a source of beneficial Na ions during the growth. However, various other alternative substrates are also used (further described in the next section). Mo is the preferred back contact usually deposited by dc magnetron sputtering which forms an ohmic contact with the CIGS layer by formation of an interfacial  $\text{MoSe}_2$  layer. The P-type CIGS is grown usually by a co-evaporation method. The chemical deposition of CdS layer on top of the P-type CIGS layer forms the necessary PN-junction for a solar cell. The undoped ZnO which is usually deposited by rf magnetron sputtering from ceramic target eliminates the negative impacts due to defects such as pinholes. The transparent conducting Al:ZnO layer is deposited on top of i-ZnO and acts as a front contact. The metal grids are used to make an external connection.



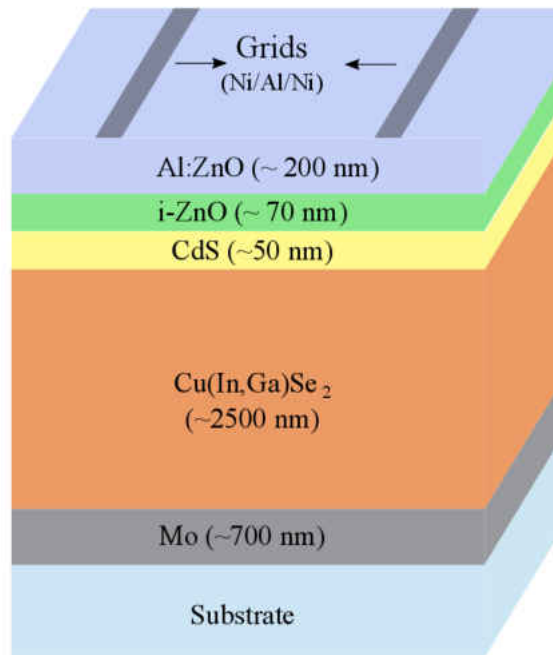


FIG. 8: Schematic diagram of a typical CIGS solar cell device.

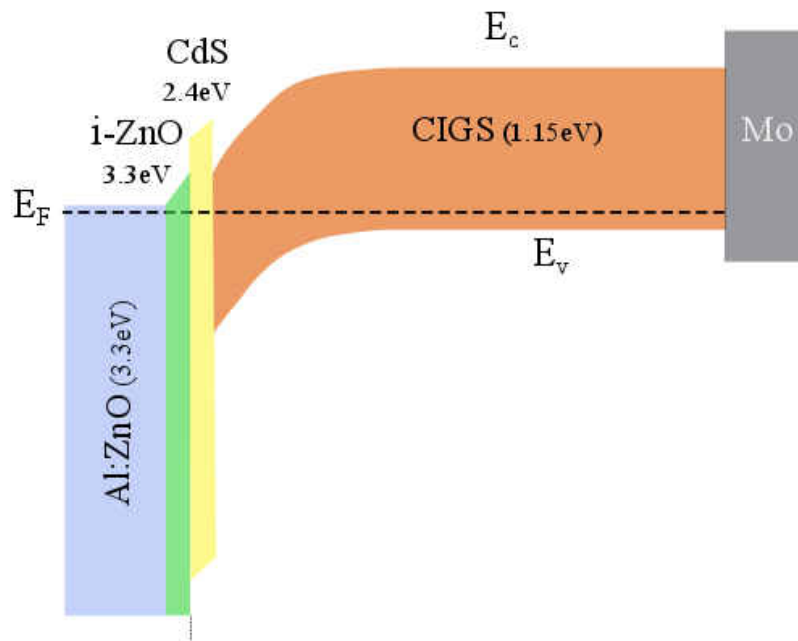


FIG. 9: Band diagram of a CIGS solar cell device.

### 2.4.1 SUBSTRATE

A variety of substrates such as soda lime glass (SLG), polymers, and metal foils have been used to produce CIGS solar [20, 45, 84]. SLG is a widely used substrate material for CIGS and has produced the record efficiency devices. SLG has a similar coefficient of thermal expansion (CTE) to CIGS as shown in Table 2 after reference [85]. When the CTE of the substrate does not match with the CIGS, adhesion failure occurs during the cooling down process, after the CIGS growth at high temperature (550°C-600°C). SLG substrate also supplies sodium to the growing CIGS film, which induces  $V_{oc}$  and FF improvement in the device [86].

Using metal foils such as stainless steel or Ti substrates, however, require a barrier layer in order to prevent the diffusion of detrimental impurities.  $Al_2O_3$  or  $SiO_2$  barrier layers are typically used to stifle the diffusion of detrimental impurities in case of metal foils or deliberate prevention of alkali diffusion in the CIGS layer from SLG [84, 87]. Polyimide foils, which can only withstand temperatures of about 450°C, have been successfully used to produce 18.7% efficient CIGS solar cells [20].

### 2.4.2 BACK CONTACT

Molybdenum is widely used as a back contact for CIGS solar cells. Mo is the preferred back contact for CIGS solar cells for multiple reasons, such as low contact resistance with CIGS layer, mechanical stability during high temperature growth process, formation of beneficial  $MoSe_2$  interfacial layer, chemical inertness with Cu, In and Ga, good adhesion with soda lime glass (SLG) substrate and providing pathways for Na diffusion from SLG substrate [88, 89]. However, sputter deposition of single layer Mo thin film with optimum quality is non-trivial because the Mo thin films exhibit excellent adhesion, porous morphology and poor conductivity at relatively high deposition pressure but poor adhesion, dense morphology and better conductivity at relatively low deposition pressure [90, 91]. Additionally, other experimental parameters such as power, substrate temperature and throw distance between target and substrate also play an important role in determining the Mo film properties [90, 91, 92]. In practice, a bilayer Mo film comprising of a bottom layer deposited at relatively high Ar pressure with good adhesive properties and top layer deposited at relatively low Ar pressure with good conductivity is used in CIGS solar cells [36, 93, 94, 95].

Aside from Mo, other metal films such as W, Ta, Cr, Nb, V, Mn, Ti have been investigated to function as a back contact [96]. It was observed that Ti, V, Cr and Mn react with the Se during the CIGS deposition; however Ta, W produced similar results as Mo [96].

TABLE 2: Coefficient of thermal expansion and the density of the substrate materials used in CIGS solar cell[85].

Material	CTE[ $10^{-6}\text{K}^{-1}$ ]	Density[g/cm <sup>3</sup> ]
SLG	9	2.4-2.5
Stainless Steel	10-11	8
Mild Steel	13	7.9
Cu	16.6	8.9
Ni/Fe alloys	5-11	8.3
Ti	8.6	4.5
Mo	4.8-5.9	10.2
Al	23	2.7
ZrO <sub>2</sub>	5.7	5.7
Polyimide (kapton or Upilex)	12-24	1.4
CuInSe <sub>2</sub>	7-11	5.8
ZnO	3-5	5.6

### 2.4.3 CIGS ABSORBER LAYER

A unit cell of the Cu(In,Ga)Se<sub>2</sub> crystal lattice based on reference [59] is shown in Figure 10. CIGS crystalize in the chalcopyrite lattice structure (similar to a Zincblende structure) in which Cu and In (or Ga) occupy the cation positions such that Se (anion) is bonded to two Cu and two In(or Ga) atoms as shown in Figure 10. A pseudobinary Cu<sub>2</sub>Se – In<sub>2</sub>Se<sub>3</sub> equilibrium phase diagram of the Cu-In-Se system is shown in Figure 11. In Figure 11,  $\alpha$  is the chalcopyrite CuInSe<sub>2</sub>, which exist in a narrow range and is most wide around 600°C before vanishing completely above 800°C. On the In rich side of the pseudo-binary section between  $\alpha$  - CuInSe<sub>2</sub> and In<sub>2</sub>Se<sub>3</sub>, other phases such as  $\beta$  - CIS (Cu<sub>2</sub>In<sub>4</sub>Se<sub>7</sub>, CuIn<sub>3</sub>Se<sub>5</sub>),  $\gamma$  - CIS (CuIn<sub>5</sub>Se<sub>8</sub>) exist. A high-temperature  $\delta$ -phase with sphalerite structure is unstable at room temperature [97]. The addition of Ga or Na increases the chalcopyrite phase field

which is believed to be the result of the reduction in the formation of ordered defect phases ( $\beta$  - phase) [77].

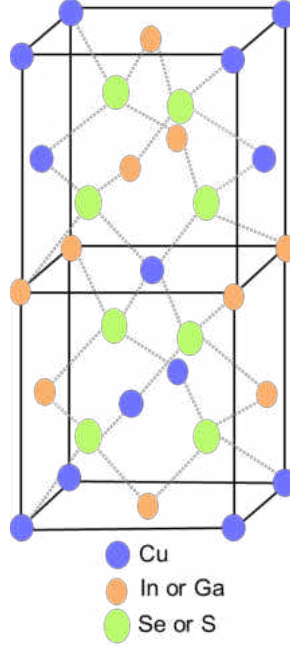


FIG. 10: A unit cell of the  $\text{Cu}(\text{In,Ga})\text{Se}_2$  crystal lattice based on reference [79].

The major optical parameter of a semiconductor is the complex refractive index  $N$ , where  $N = n + ik$ . The complex refractive index of a semiconductor which contains the same information as the dielectric function  $\epsilon = \epsilon_1 + i\epsilon_2$  with  $\epsilon_1 = n^2 + k^2$  and  $\epsilon_2 = 2nk$  is closely related with its electronic band structure. The features observed in the dielectric function are associated with the van Hove singularities or the critical points that correspond to the energy at which the joint density of states in the electronic band structure shows strong variations [99, 100, 101]. A critical point analysis has been carried out by Alonso et. al [99] and more recently by Minoura et. al [102] and Aryal et. al [101] for various composition from  $0 < \text{Ga}/(\text{Ga}+\text{In}) < 1$  in CIGS alloy system.  $E_o(\text{A,B})$  critical point energy, which originates from the energy transition at the Brillouin zone center, is observed at the bandgap energy [99, 103]. References [101, 102, 104] reported a shift in the critical point energy as a function of the  $\text{CuIn}_{1-x}\text{Ga}_x\text{Se}_2$  alloy composition. Minoura et. al [102] reported that only the  $E_o(\text{A,B})$  depend on both Cu and Ga content of the  $\text{CuIn}_{1-x}\text{Ga}_x\text{Se}_2$  alloy. However, the other critical point energy was independent of Cu composition and only varied

with the Ga content. In another study by Aryal et. al [101], a quadratic dependence on the Ga content in the critical point energy of  $\text{CuIn}_{1-x}\text{Ga}_x\text{Se}_2$  alloy was observed.

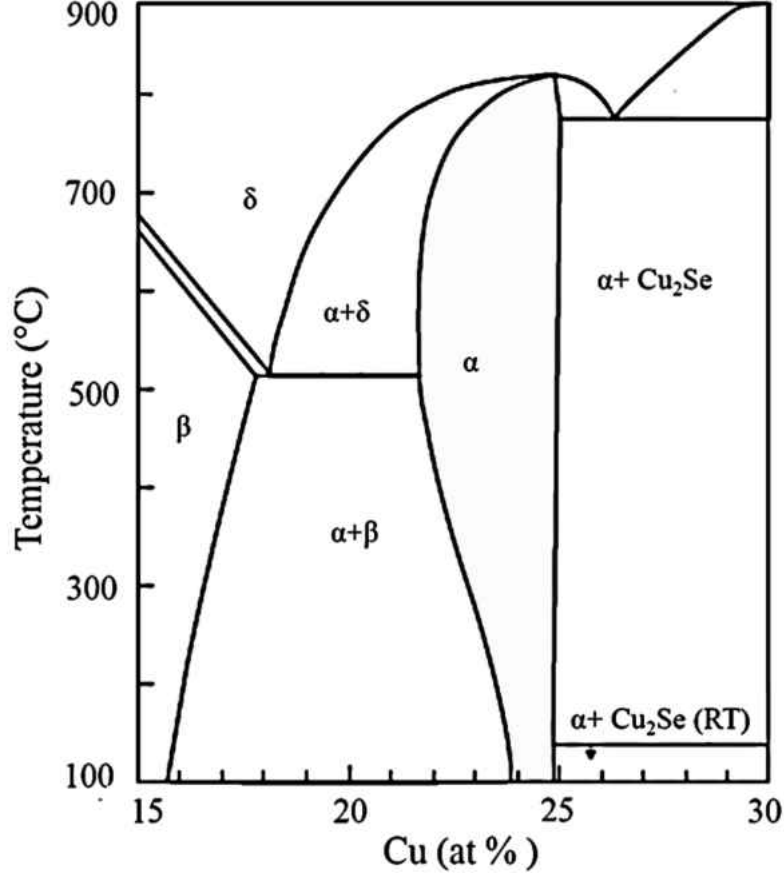


FIG. 11: A pseudo-binary  $\text{Cu}_2\text{Se}-\text{In}_2\text{Se}_3$  equilibrium phase diagram based on reference [98].

CIGS is a direct bandgap semiconductor [105] due to the alignment of the maximum of the valence band and the minimum of the conduction band at the same value of the crystal momentum. Since CIGS is direct bandgap semiconductor, the absorption coefficient ( $\alpha$ ) increases rapidly by several order of magnitude at the bandgap energy, which allows a thin film about 2-3  $\mu\text{m}$  to be used as an absorber layer in the solar cell.  $\alpha$  can be directly obtained from the extinction coefficient  $k$  value of the complex refractive index by using equation (10). Again, for a direct band gap

semiconductor, the absorption coefficient can also be expressed by equation (22),

$$\alpha = \frac{A\sqrt{(E - E_g)}}{E} \quad (22)$$

where A depends on the density of states. From equation (22) we can obtain the bandgap energy by plotting  $(\alpha E)^2$  versus the photon energy  $E$ .

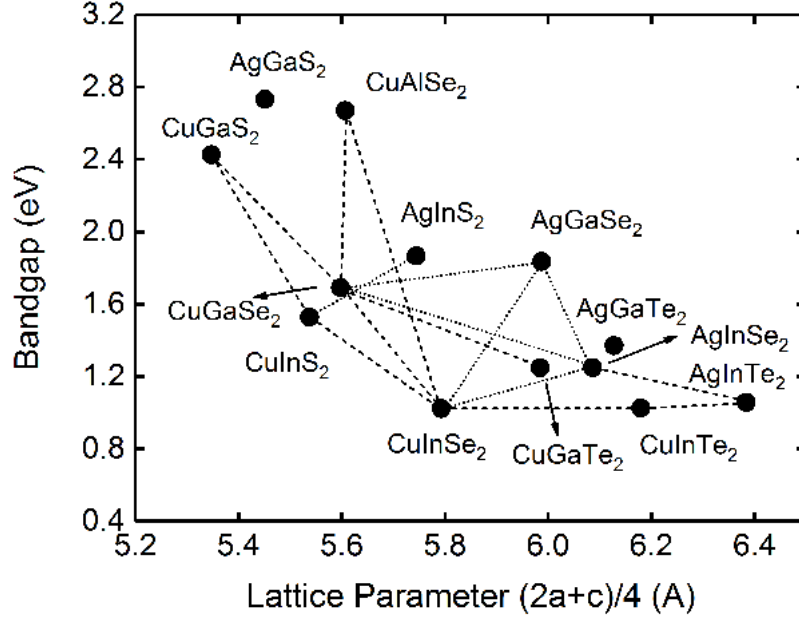


FIG. 12: Lattice constant versus bandgap for some I-III-VI<sub>2</sub> compounds [81].

The lattice constant versus the bandgap of some of the compounds in the I-III-VI<sub>2</sub> family is shown in Figure (12). The addition of Ga in CuInSe<sub>2</sub> increases the bandgap from 1.02 eV (CuInSe<sub>2</sub>) to 1.67 eV (CuGaSe<sub>2</sub>), primarily shifting the conduction band minimum [106]. In the case of thin films of CuIn<sub>1-x</sub>Ga<sub>x</sub>Se<sub>2</sub>, an empirical equation is used to express the composition dependence of the bandgap [79], which is expressed as (equation (23)),

$$E_g = 1.02 + 0.65x - b(1 - x) \quad (23)$$

where the bowing parameter  $b$  in the range of 0.11 – 0.26 has been experimental observed.

#### 2.4.4 BUFFER LAYER

CdS grown by chemical bath deposition (CBD) [45], which forms the electrical junction with the P-type CIGS absorber layer, is the most common buffer layer. A typical CdS bath contains an aqueous solution with Cd salt (Cadmium Acetate, Cadmium sulfate etc.), ammonia and thiourea at the deposition temperature of 60°C-90°C [107]. The CdS thin film prepared by the CBD process provides conformal coverage to the CIGS layer, despite its high surface roughness [108, 109]. Additionally, chemical bath processing of CdS etches the surface to some extent, which removes the surface contaminants resulting in a better CIGS/CdS interface [110]. It has been reported that the Cd diffusion in the CIGS near surface forms an inverted junction, which reduces the surface recombination rates via interface defects. Additional benefits of CBD-CdS comes from the ideal band alignment with the CIGS layer and high doping density, which results in an extended space-charge region in the CIGS layer augmenting the collection of photo-generated carriers. However, due to a relatively low bandgap of  $\approx 2.4$  eV there is higher parasitic absorption loss mainly in the blue region. The other disadvantage of CdS is the toxicity of Cd. Thus, ongoing research has been focused on various other alternative buffer layers such as Zn(S,O,OH),  $\text{Zn}_{1-x}\text{Mg}_x\text{O}$ ,  $\text{In}_2\text{S}_3$ ,  $\text{Zn}_{1-x}\text{Sn}_x\text{O}$  [111, 112, 113].

#### 2.4.5 FRONT CONTACT

Typically a bilayer of intrinsic ZnO (i-ZnO) and highly doped wide bandgap semiconductors such as ITO, ZnO containing n-type dopant such as Al, Ga, B is used as a transparent conducting oxide (TCO) [9, 111, 114, 115]. An efficient TCO requires high transparency for photons in the visible range, high conductivity for lateral current collection and moisture stability [9]. Sputtering and chemical vapor deposition are two common processes to deposit the transparent conducting oxides [9].

## CHAPTER 3

### SAMPLE PREPARATION AND CHARACTERIZATION

#### METHODS

This chapter introduces CIGS solar cell devices preparation steps used in this work. To characterize the resulting materials and the devices, a number of characterization techniques were employed including X-ray fluorescence (XRF), scanning electron microscopy (SEM), x-ray diffraction (XRD), secondary ion mass spectrometry (SIMS), deep level transient/optical spectroscopy (DLTS/DLOS), photoluminescence (PL), x-ray photoelectron spectroscopy (XPS), spectroscopic ellipsometry (SE), current-voltage measurement (I-V), and quantum efficiency measurement (QE). The growth process and the characterization methods used in this work are described in the following sections.

#### 3.1 SAMPLE PREPARATION

##### 3.1.1 SUBSTRATE

In this work, soda lime glass and alumina substrates were used. Substrates were cleaned with Micro 90 soap solution in a sonicator for an hour, rinsed with deionized (DI) water and finally dried off with nitrogen gas.

##### 3.1.2 BACK CONTACT

Molybdenum was used as the back contact for the CIGS solar cell. A bilayer Mo was deposited by DC magnetron sputtering. The bottom layer was deposited at Ar pressure of 1.33 Pa and the top layer at low Ar pressure of 0.4 Pa, at a constant power density of 7.4 W/cm<sup>2</sup>. The resulting combined thickness of the Mo film was  $\approx$  800 nm.



### 3.1.3 CIGS ABSORBER LAYER

The CIGS layer was deposited by a three-stage coevaporation method [116]. A precursor  $(\text{In,Ga})_x\text{Se}_y$  layer was deposited at the temperature of  $400^\circ\text{C}$ . When the desired thickness of roughly  $1\mu\text{m}$  of  $(\text{In,Ga})_x\text{Se}_y$  was obtained the In and Ga flux were terminated. The substrate temperature was ramped up to usually between  $550^\circ\text{C}$ - $600^\circ\text{C}$ . Then the Cu flux was introduced. When the overall film composition became Cu-rich, the Cu flux was terminated and the In and Ga flux was introduced again until the overall composition of the film became Cu-poor. The process control technique and further details on the deposition process are given in the experimental section of chapter 4.

### 3.1.4 BUFFER LAYER

Cadmium sulfide deposited by chemical bath process was used as a buffer layer. 15 ml of 6.7 g/l aqueous solution of Cadmium Acetate, 15 ml of 28.5 g/l aqueous solution of Thiourea and 35 ml of  $\text{NH}_4\text{OH}$  (28%) were first mixed into a beaker containing 185 ml of DI water. The beaker was then placed into the water bath preheated at  $70^\circ\text{C}$ . Then the samples were then dipped into the solution and the deposition was completed in 20 minutes which resulted in  $\approx 50\text{nm}$  thick CdS film on the CIGS. If a variation in the thickness of CdS film was desired, the deposition time was adjusted accordingly. After the desired thickness was obtained, the samples were rinsed with DI water and dried with nitrogen gas.

### 3.1.5 FRONT CONTACT

A combination of i-ZnO and indium tin oxide,  $\text{In}_2\text{O}_3:\text{Sn}$ (ITO) was used as a front contact. Both films were deposited by RF magnetron sputtering process at 13.56 MHz. 80-100 nm of i-ZnO and 200-250 nm of ITO was deposited at Ar pressure of 0.67 Pa with a power density of  $4.9\text{ W/cm}^2$ . The substrate temperature was kept at room temperature. Substrate rotation of 20 rpm was used to achieve the thickness uniformity of the film.

### 3.1.6 METAL CONTACT

Metal grids were deposited on top of the ITO layer to provide a contact pad for J-V characterization of the cells. The tapered finger grids in a 50/3000/50 nm thick

Ni/Al/Ni sandwich were deposited by e-beam evaporation through a shadow mask and covered approximately 4% of the total cell area.

## **3.2 CHARACTERIZATION METHODS**

### **3.2.1 X-RAY FLUORESCENCE**

X-ray fluorescence (XRF) is a non-invasive and non-destructive analytical technique used to analyze the elements and their concentration in the material. The basis of this technique involves the exposure of a sample to X-rays, which are characterized by an energy in the range of 0.125 KeV to 125 KeV in the electromagnetic spectrum. Typically, energy dispersive XRF can detect the elements from Na to U while the wavelength dispersive XRF can even identify elements down to Be. Elemental concentration from 100% to sub-ppm level can be detected, nevertheless detection limits depends on the specific element, the sample matrix and the design of the XRF instrument itself. If the incident x-rays have enough energy, tightly bound electrons in the inner orbital are dislodged. The loss of electrons from an inner shell renders the atom in the electronically unstable configuration. In order to restore the equilibrium, the higher orbit electrons occupy the empty inner shells. In this process, the excess energy, which is the difference between the participating orbitals, is usually emitted in the form of fluorescent X-ray. The measurement of the energy of this characteristic X-ray fluorescence is used to identify and quantify any element present in the sample.

In this work, the composition and/or thickness of CIGS samples were determined by using Solar Metrology System SMX, XRF system. A reference CIGS sample analyzed by Calmetrics Inc. was used in the calibration process. The fundamental parameters technique was employed for XRF analysis, to convert the elemental peak intensities to elemental concentration and/or film thickness. For the XRF measurements, primary X-rays at 65 keV with 2 mm beam size and an exposure time of 30 seconds were used.

### **3.2.2 SECONDARY ION MASS SPECTROMETRY**

Secondary ion mass spectrometry (SIMS) is a highly sensitive surface analysis technique for trace element analysis and elemental depth profile in the solid films.

In this technique, a beam of primary ions ( $\text{Ar}^+$ ,  $\text{Ga}^+$ ,  $\text{Cs}^+$  etc.) is incident on the sample surface. This interaction produces a large variety of secondary species such as electrons, neutral species, atoms or molecules or atomic and cluster ions but only the secondary ions are detected and analyzed by the mass spectrometer. Time of flight (ToF) Mass Spectrometers are one of the various types of mass analyzer used for mass separation in SIMS. The continuous sputtering and monitoring of the secondary ion count of selected elements as a function of time give the depth profile. The measurement of crater depth using profilometer can be used to convert the time axis into depth.

For ToF SIMS, the elemental depth profile of CIGS film/devices acquired in this study, 3 keV  $\text{Cs}^+$  with 20 nA current were used to create a 120  $\mu\text{m}$  by 120  $\mu\text{m}$  and middle 50  $\mu\text{m}$  by 50  $\mu\text{m}$  areas were analyzed using 0.3 pA  $\text{Bi}^{3+}$  primary ion beam. SIMS measurements used in this thesis were done at Analytical Instrumentation Facility(AIF) at North Carolina State University.

### 3.2.3 SCANNING ELECTRON MICROSCOPE

Scanning electron microscope (SEM) uses electrons to image the specimen directly. When the electrons for the beam (primary electrons) strike the specimen, they either get reflected (backscattered electron), dislodge an electron from the sample (secondary electron) or become absorbed while emitting an x-ray photon in the process. The SEM detectors use backscattered and secondary electrons to image the sample while the emitted x-rays are used to determine the elemental information about the specimen using the dedicated detectors.

For this work, a JOEL model 6060LV was used for the SEM imaging to analyze the surface and the cross-section morphology.

### 3.2.4 X-RAY DIFFRACTION

X-ray diffraction (XRD) is a non-destructive method used for identification and characterization of material using their diffraction pattern when the x-rays are directed at the sample. Comparing the measured peaks with the XRD database, the crystalline phases, lattice parameters, film texture and strain in the film can be obtained. In this thesis, film texture was analyzed by XRD measurements using a Rigaku Miniflex benchtop X-ray diffractometer in the  $\theta$ - $2\theta$  configuration.

### 3.2.5 X-RAY PHOTOELECTRON SPECTROSCOPY

X-ray photoelectron spectroscopy (XPS) gives the quantitative information about the elemental surface composition and the molecular environment of the sample surface. In XPS, photoelectrons are excited from core levels of the element present at the sample surface by irradiating with x-rays [117]. The energy of the emitted photoelectrons carries the information about elements within the sampling volume, and the number of emitted photoelectrons is the characteristic of the concentration of the emitting atoms in the sample.

XPS measurement was performed using SPECS FlexMod XPS with a monochromatic  $MgK\alpha$  (1.25 keV) x-ray radiation with a takeoff angle of  $30^\circ$  relative to the surface normal. Energy calibration was established by referencing to adventitious Carbon(C 1s line at the binding energy of 285.0 eV).

XPS measurements used in this thesis were done at Analytical Instrumentation Facility(AIF) at North Carolina State University.

### 3.2.6 DEEP LEVEL TRANSIENT/OPTICAL SPECTROSCOPY

Deep level transient/optical spectroscopy (DLTS/DLOS) is used to characterize the electrically active defect levels in the semiconductor. In a conventional capacitance based DLTS/DLOS technique, the capacitance transient in a semiconductor device or junction during the measurement phase is recorded. The response of the transient time constant as a function of temperature or the sub-bandgap light energy gives the trap energy level, while the amplitude of the capacitance change is proportional to the trap concentration. More detailed description to the DLTS/DLOS techniques is given in reference [118, 119]. The measurement parameters used for the DLTS/DLOS analysis in this thesis are given where the measurement results are discussed.

We would like to thank Pran Paul and Dr. Aaron Arehart from The Ohio State University for carrying out DLTS/DLOS measurements used in this thesis.

### 3.2.7 PHOTOLUMINESCENCE

Photoluminescence (PL) involves the excitation of electrons in a material to the higher electronic state and detection of a subsequent release of photon energy as they relax into the lower energy states. The charge carrier dynamics can be studied

with the PL emission measured with the temporal resolution known as time-resolved photoluminescence (TRPL). TRPL was used to calculate the minority carrier lifetime in the CIGS layer of the solar cell devices via a time correlated single photon counting method. A 680 nm wavelength laser was used for the excitation source, and the detection wavelength was set to the photoluminescence maximum.

We would like to thank Dr. Evgeny Danilov and Dr. Felix Castellano from North Carolina State University for carrying out PL/TRPL measurements used in this thesis.

### **3.2.8 CURRENT VOLTAGE MEASUREMENT**

The current density-voltage (J-V) characteristics of the solar cell were measured under simulated AM 1.5G illumination ( $1000 \text{ W/m}^2$ ) (Model: IV5, PV measurement, Inc.). For the temperature dependent J-V measurements, a liquid nitrogen cooled cryostat was used.

### **3.2.9 EXTERNAL QUANTUM EFFICIENCY**

External quantum efficiency (QE) measurement gives the spectral response of the solar cell. It is the measure of the ratio between the number of electron-hole pairs collected to the number of incident photon at each wavelength. QE was measured at room temperature using chopped monochromatic light in the range from 300 to 1300 nm, usually in the step of 10 nm (model: QEX7, PV measurement, Inc.).

### **3.2.10 SPECTROSCOPIC ELLIPSOMETRY**

Spectroscopic ellipsometry (SE) is a very sensitive non-destructive, non-invasive optical measurement technique that uses polarized light to characterize thin films, surfaces and material microstructure [119]. This optical technique is commonly applied to measure thin film thickness and optical constants. SE measures the change in polarization of the light as it reflects from the sample surface, which is reported as two measured values ( $\Psi$ ,  $\Delta$ ) as a function of photon energy. We shall consider an orthogonal p-s coordinate system in order to understand the measurement geometry and define  $\Psi$  and  $\Delta$  [120]. The p-direction is taken to be parallel to the direction of the propagation of light and contained in the plane of incidence which is the plane containing the incident, normal and reflected light. The s-direction is perpendicular

to the direction of the propagation and is parallel to the sample surface. In this configuration, the light of known polarization is incident on the sample surface, and the polarization state of the outgoing light are measured. The encoded information is expressed as  $\Psi$  and  $\Delta$ . The parameters  $\Psi$  and  $\Delta$  are defined as (equation (24) as equation (25)),

$$\Delta = \delta_p - \delta_s \quad (24)$$

$$\tan(\Psi) = \frac{|r_p|}{|r_s|} \quad (25)$$

where,  $\delta_p$  and  $\delta_s$  represent the phase difference between the p-wave and the s-wave of the polarized light before striking the sample and after reflecting from the sample surface. The amplitude of both the p-component and the s-component may change after reflection. The  $|r_p|$  and  $|r_s|$  are the ratios of outgoing wave amplitude to the incoming wave amplitude for the p and s components respectively.  $\Psi$  ranges from  $0^\circ \leq 90^\circ$  since it is defined from the absolute reflection coefficient however  $\Delta$  ranges from  $0^\circ \leq 360^\circ$  being the phase difference.

An ellipsometer measures  $\Psi$  and  $\Delta$  for various wavelengths which cannot be directly converted into the optical constants. Thus, a model-based analysis must be used. This approach of ellipsometry data analysis involves three major parts (i) the construction of the optical model representing the nominal structure of the sample with starting parameters, (ii) determination of the best-fit parameters for the assumed model and (iii) evaluation of the fitting error and checking the reasonability of the result. Two commonly used data analysis methods are the least square regression and the mathematical inversion [120].

### 3.2.11 SOFTWARE: SCAPS

SCAPS is a one-dimensional solar cell simulation software developed at the University of Gent, Belgium [121]. We have used the SCAPS software to simulate the devices wherever necessary and discuss the salient properties. The parameters used in such simulation are tabulated in the respective sections.

We would like to thank Dr. Marc Burgelman from University of Gent for providing us SCAPS software.

## CHAPTER 4

# KF POST DEPOSITION TREATMENT ON CIGS SOLAR CELLS

Several laboratories have now fabricated polycrystalline  $\text{Cu}(\text{In,Ga})\text{Se}_2$  (CIGS) solar cells with efficiencies higher than 20% [4]. Alkali doping is indispensable to achieve such high efficiency. Hedstrom et al.[22] were among the first to realize the importance of Na diffusion from soda lime glass into CIGS solar cells. The alkaline metal Na, supplied either by the soda lime glass substrate or during the CIGS deposition process, leads to higher performance CIGS solar cells, improving both open circuit voltage ( $V_{oc}$ ) and fill factor (FF) [30, 122]. The observed higher net hole concentration is thought to be the cause of the increase in  $V_{oc}$  and FF [123]. Similarly to Na, Laemmle et al. [124] demonstrated increases in  $V_{oc}$ , FF and net carrier concentration after the post deposition treatment of CIGS by KF on alkali-free substrates. The improvement in the device was further linked to the passivation of grain boundaries and the donor like defects. They also observed potassium to diffuse homogeneously throughout the film depth. In another study by the same group, potassium was found to result in small grained CIGS when applied as a precursor rather than during post annealing, as compared to a potassium free sample [125]. They concluded that the presence of potassium deters the interdiffusion of the constituent elements. As a result, a more pronounced gallium gradient is produced and causes Cu depletion at the CIGS surface, while the post annealing of CIGS in the presence of potassium does not affect the CIGS composition. More recently, Chirila et al.[44] demonstrated a high efficiency (20.4%) CIGS solar cell on a polyimide substrate which does not contain alkali, by applying sequential NaF and KF PDT. They reported that the use of KF after the deposition causes surface modification, allowing higher  $\text{Cd}_{Cu}$  formation during CdS chemical bath deposition, and a thinner CdS layer to be used without compromising device performance. In reference [46], the presence of ordered defect compounds (ODC) at the surface prior to KF PDT was reported to determine whether such treatment could benefit or degrade the device. The formation of a K containing  $\text{In}_2\text{Se}_3$  surface layer was observed when ordered defect compound

was present prior to KF PDT, but no trace amount of K was noticed when ODC was not present before KF PDT along with segregation of detrimental  $\text{Cu}_x\text{Se}$  and high amount of elemental Se at the surface. Jackson et al. have demonstrated the short circuit current gain by minimizing CdS thickness and lowering the position of the minima of the double gallium gradient in the KF treated sample [19]. They argued structural defects should increase with such a strong gallium gradient in the space charge region causing an increase in recombination. So, defect passivation was assumed to occur due to KF PDT. Both ideality factor and the reverse saturation current were found to increase in the KF treated device showing the improvement in the diode. The widening of the surface bandgap potentially due to a Cu and Ga depleted surface in NaF/KF PDT CIGS solar cells have also been proposed to be the cause of the observed improvement in the efficiency of those devices [52]. However, many questions still remain to this date on the exact effect of these alkali PDT on the properties of CIGS.

In this Chapter, we present the effect of potassium fluoride (KF) post deposition treatment of CIGS on the properties of the thin films and the solar cells. We demonstrate the use of in-situ real-time spectroscopic ellipsometry (RTSE) to monitor the CIGS deposition process and track the time evolution of the material properties in real time. In-situ RTSE makes it possible to deduce the modification in the as deposited film without external influences. The compositional modification due to KF post-deposition treatment in the near surface of the CIGS thin film has been analyzed through the spectroscopic ellipsometry measurements. Furthermore, SIMS measurements have been used to probe the elemental distribution in the bulk of the CIGS film. To have a complete picture of the role of KF incorporation in the CIGS film on the formation of defects, a combination of DLTS and DLOS have been applied. Moreover, the location of potential traps was identified with the scanning DLTS method.

One possible reason for device enhancement due to KF PDT frequently invoked in the literature but lacking sufficient experimental verification was identified to be the modification of localized deep-level traps, which are associated with defects and impurities in the materials [126]. In order to shed light on this issue, we were motivated to study the trap spectrum within the bandgap of the CIGS and experimentally verify whether KF treatment leads to defect passivation and discuss how it contributes to the observed improvement in the photovoltaic parameters after KF treatment.



We perform a systematic comparison between the reference sample and KF treated samples ensuring that the reference sample has relatively high efficiency and compositional variation is minimized. We performed this study with two different substrates, one containing Na and another devoid of Na, in order to isolate any competing effect due to the presence of Na.

#### 4.1 EXPERIMENTAL DETAILS

In this study, CIGS films were grown on molybdenum coated SLG and alumina substrates by the three-stage process [116] in a high vacuum co-evaporation chamber. Alumina was chosen as an alkali-free substrate, which has a comparable coefficient of thermal expansion to CIGS to inhibit the delamination of CIGS film due to thermal stress during deposition. In order to investigate the effect of K on the CIGS absorber, two sets of experiments on each substrate (SLG and Alumina) were performed. In the first set of experiments, reference samples without KF PDT were prepared. Note that a trace amount of K is expected in the CIGS films prepared on SLG substrate due to the diffusion from the SLG glass substrate. In the second set of experiments, after CIGS deposition the substrate temperature was first reduced to 350°C, and the CIGS films then underwent a KF PDT for 15 minutes while a Se flux was applied. The thickness of the KF layer was calibrated at 20 nm. The film was finally cooled to room temperature and the selenium supply was discontinued when the substrate temperature fell below 300°C. Devices were completed by depositing about 50 nm of CdS by chemical bath deposition, followed by i-ZnO ( $\approx 50$  nm), ITO ( $\approx 250$  nm) and Ni/Al/Ni front contacts.

#### 4.2 RTSE ANALYSIS OF CIGS FILMS BEFORE AND AFTER KF PDT

The CIGS deposition was monitored by using an IR temperature sensor that records the substrate temperature and real-time spectroscopic ellipsometry (RTSE) simultaneously. A rotating compensator multichannel spectroscopic ellipsometer set at an angle of incidence of 65° was used for in-situ RTSE measurements. The ellipsometry data  $(\Psi, \Delta)$ , defined by  $\tan(\Psi)\exp(i\Delta) = r_p/r_s$ , where  $r_p$  and  $r_s$  are the amplitude reflection coefficients for p and s linearly polarized light respectively [120], were measured for the spectral range of 0.75 eV to 6.5 eV. Monitoring substrate

temperature keeping the substrate heater power constant or vice-versa is well-known technique to monitor the three-stage deposition process of CIGS film [127]. Substrate temperature monitoring was used to cross-validate the process monitoring by in-situ RTSE technique. Figure 13 depicts the in-situ RTSE measurements of the ellipsometry amplitude angle ( $\Psi$ ) for a photon energy of 2.615 eV in conjunction with the substrate temperature profile.

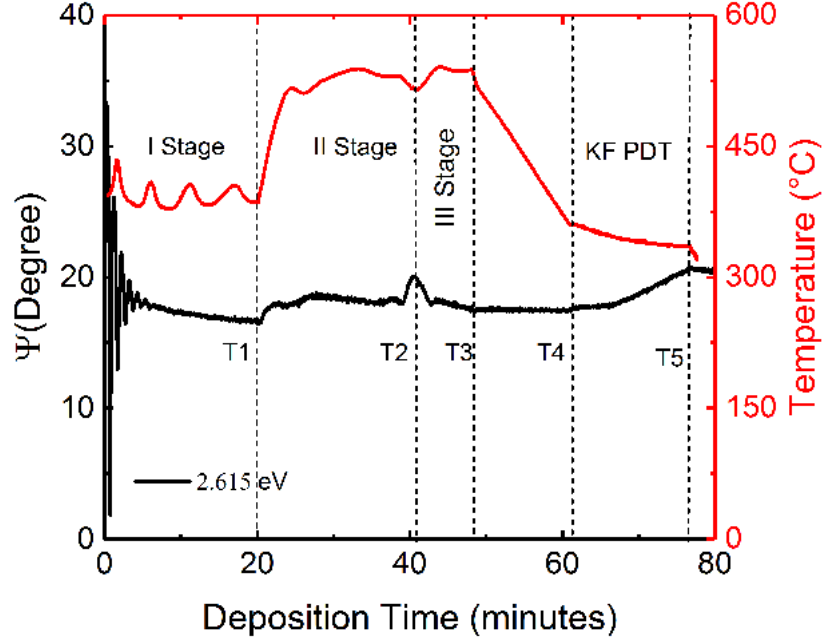


FIG. 13: The evolution of  $\Psi$  parameter measured by ellipsometer as a function of deposition time (black) and the substrate temperature change during the CIGS deposition (red) [36].

In the first stage of the three stage process  $(\text{In,Ga})_2\text{Se}_3$  is deposited which is represented in Figure 13 from time  $t = 0$  minute to 20 minute. The In and Ga flux were closed after the first stage, and the substrate temperature was raised to  $550^\circ\text{C}$  and the Cu flux was introduced. As the Cu flux is introduced the precursor  $(\text{In,Ga})_2\text{Se}_3$  is converted to  $\text{Cu}(\text{In,Ga})\text{Se}_2$ . After  $(\text{In}_{1-x}\text{Ga}_x)_2\text{Se}_3$  (IGS) has been transformed into CIGS near the end of the second stage of deposition, an abrupt decrease in the pyrometer temperature, due to the rise in the film surface emissivity, indicates the formation of the semi-metallic phase  $\text{Cu}_{2-x}\text{Se}$ . The same transition is recorded by RTSE, via an increase in  $\Psi$ , identified by T1 to T2 (Figure 13). When the third stage

starts at T2, the Cu flux is turned off while the In and Ga fluxes are turned on. The  $\text{Cu}_{2-x}\text{Se}$  phase is then progressively transformed into CIGS, which is indicated by the rise in substrate temperature (T2 to T3). The In and Ga fluxes are maintained until the appropriate stoichiometry is reached (T4). Interestingly,  $\Psi$  returns to its original value after the transition from Cu-rich to Cu-poor (compare T2 and T3), and decreases only slightly thereafter until the end of deposition (T4). The substrate temperature is then reduced to  $350^\circ\text{C}$  while the selenium flux is held constant. During this time,  $\Psi$  remains mostly unchanged for all measured wavelengths. At T4, the KF flux is turned on, resulting in a continuously increasing  $\Psi$  for all wavelengths, until the KF flux is turned off at T5. T4 represents the end of deposition in case KF PDT was not performed.

For the RTSE data analysis, an optical model based on a multilayer cell structure was used as shown in Figure 14. First, the complex dielectric functions  $\epsilon(E) = \epsilon_1(E) + i\epsilon_2(E)$  were obtained for the IGS and CIGS film by analyzing the  $(\Psi, \Delta)$  spectra acquired at the end of the first stage and after the third stage respectively, by least-square regression analysis [120] using the Levenberg-Marquardt method. For the IGS, the dielectric function was determined using one critical point parabolic band (CPPB) oscillator to represent the IGS bandgap and one background Tauc-Lorentz oscillator. For the CIGS film, four CPPB oscillators and one background Tauc-Lorentz oscillator along with a constant contribution  $\epsilon_{1,\infty}$  to the real part of  $\epsilon$  were used. In the analyses to determine the dielectric functions, the dielectric function parameters and thicknesses were varied until a good fit was obtained between the calculated and measured data, as quantified by the root mean squared error (MSE). The dielectric function of  $\text{Cu}_{2-x}\text{Se}$  was determined in previous experiments [128].

Based on these dielectric functions of the components, the RTSE data were then analyzed using the model shown in Figure 14 to determine the time evolution of bulk layer thickness ( $d_b$ ), surface roughness layer thickness ( $d_s$ ), and void volume fraction ( $f_v$ ) [129, 130]. Figure 15 shows the time evolution of the bulk and surface roughness thicknesses during the deposition process. During KF PDT,  $d_s$  increases while  $d_b$  remains relatively constant. From the analysis, a  $d_s$  value of 20.5 nm with  $f_v$  of 25% was obtained for CIGS prior to KF PDT and a  $d_s$  value of 30.6 nm with  $f_v$  of 64.3% was obtained after KF PDT. The same parameters ( $\Psi, \Delta$ ) that were used to extract the bulk layer and the surface roughness layer thicknesses ( $d_b, d_s$ ) were also used to

extract the complex dielectric functions ( $\epsilon_1, \epsilon_2$ ).

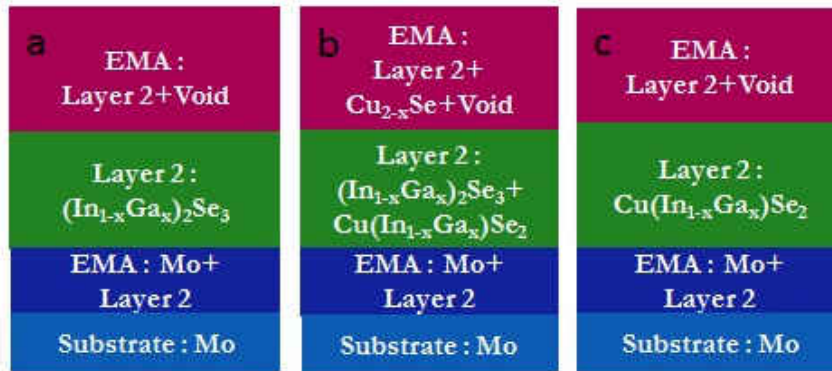


FIG. 14: Schematic of the optical models for a) the IGS film in stage 1; b) IGS to CIGS conversion, Cu<sub>2-x</sub>Se formation and Cu<sub>2-x</sub>Se to CIGS conversion in stage 2 and 3; c) the CIGS before and after KF PDT at 350°C [36].

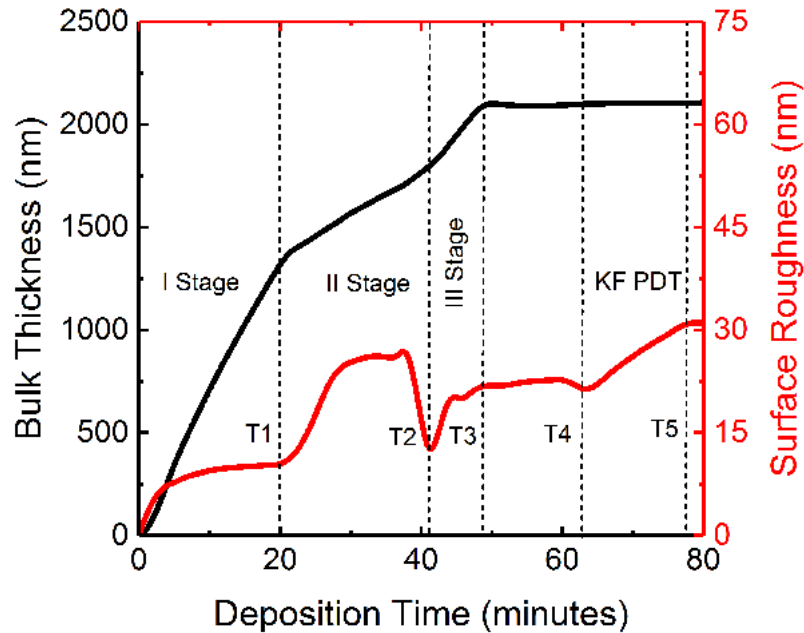


FIG. 15: Bulk thickness (black) and surface roughness thickness (red) of CIGS deduced from RTSE as a function of time [36].

Figure 16 shows the CIGS dielectric functions before and after KF PDT at 350°C,

clearly demonstrating the modification of the dielectric functions above 1.5 eV where the penetration depth is small ( $< 300$  nm) relative to the thickness. The results suggest a Ga deficiency within at least 40 nm of the surface as the  $E_1(A)$  critical point(CP) energy at 2.94 eV is red-shifted upon KF PDT. This can be seen most clearly by the 0.2 eV red-shift in the  $E_1(A)$  CP peak in  $\epsilon_1$ , which would suggest a Ga reduction by  $\Delta x = 0.15 - 0.20$  based on previous work [101]. The  $E_1(A)$  CP is identified as a direct dipolar transition associated with the N point  $(\pi/a)(110)$  in the band structure of CIGS [99]. The suggestion of a Ga deficiency is consistent with the previous observation [44].The CP energy may also be affected by film structure and voids since the deduced void content in the roughness layer is high, and voids may also extend into the bulk layer. The higher CP energies were not evaluated for the Ga deficiency because these would be even more strongly affected by a near-surface density deficiency and associated EMA limitations [101]. The corresponding bandgap of the CIGS film as extracted from the extinction coefficient is shown in Figure 17.

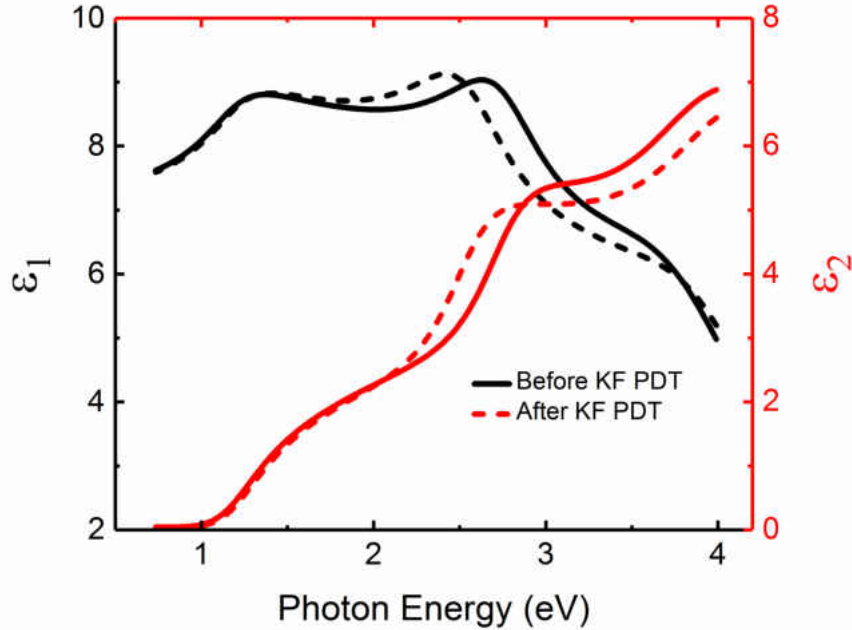


FIG. 16: Dielectric function of the CIGS film before and after KF PDT [36].

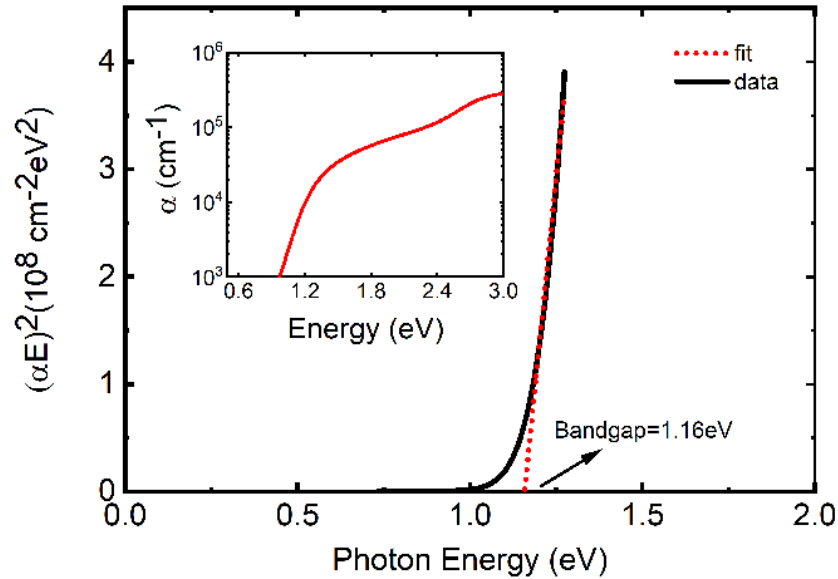


FIG. 17: The bandgap of the CIGS thin film extracted from the ellipsometry analysis. Absorption coefficient as a function of photon energy is shown in the insert.

### 4.3 COMPOSITION AND ELEMENTAL DISTRIBUTION

#### 4.3.1 CIGS GROWN ON ALUMINA SUBSTRATE

The composition of the CIGS film measured by XRF is shown in Table 3, which confirms that the samples used for comparison have a similar bandgap. The elemental depth profile in the CIGS film was obtained by SIMS measurement and is shown in Figure 18 for the film without KF and in Figure 19 for the CIGS film treated with KF PDT. Comparing the SIMS profile of the samples with and without KF PDT, the elemental distribution of the constituent elements (Cu, In, Ga, Se) did not show appreciable difference except for the  $K^+$  depth profile (see Figure 3). SIMS revealed that the  $K^+$  is distributed throughout the CIGS film in KF treated samples. The intensity of the  $K^+$  signal peaks at the surface at about 10% of the film depth from the surface; however, it remained fairly homogeneous in the rest of the film thickness, following closely the gallium depth profile.

TABLE 3: The elemental composition of the CIGS thin films deposited on Mo coated alumina substrate with and without KF PDT from XRF measurement.

Sample	Cu(at%)	In(at%)	Ga(at%)	Se(at%)
No KF	22.9	17.6	9.6	49.9
KF PDT	22.6	17.4	9.6	50.3

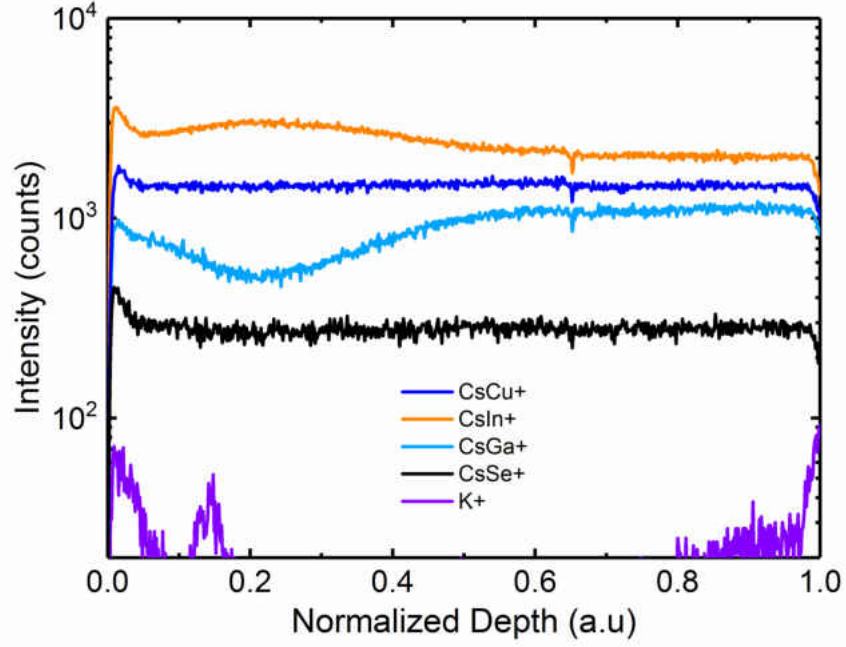


FIG. 18: Elemental depth profile of the CIGS film prepared on alumina/Mo substrate with no post deposition alkali halide treatment measured by SIMS [73].

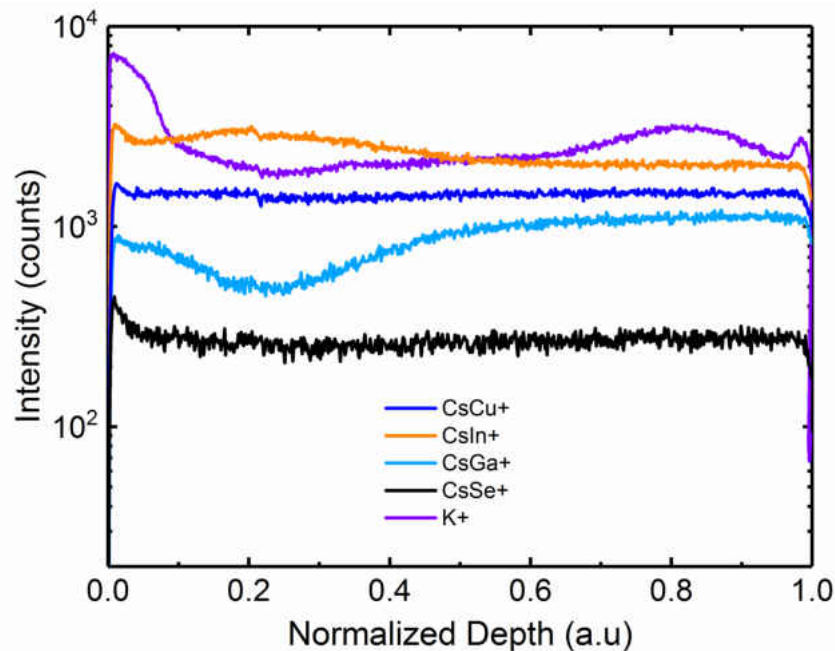


FIG. 19: Elemental depth profile of the CIGS film prepared on alumina/Mo substrate with KF post deposition treatment measured by SIMS [73].

#### 4.3.2 CIGS GROWN ON SLG SUBSTRATE

The composition of the CIGS film is shown in Table 4, validating the similar nominal bandgap of the CIGS thin films under study. SIMS measurements were carried out for both the samples (Figure 20 and Figure 21). One can see that the intensity of the  $K^+$  signal increased throughout the device for the sample with KF PDT compared with the one without. On the other hand, the  $Na^+$  intensity decreased throughout the device with KF PDT (even considering the possibly higher Na out-diffusion from SLG during KF PDT at the substrate temperature of 350 °C). This indicates that  $K^+$  diffuses quickly throughout the entire film thickness which was also observed in the sample prepared on alumina substrates discussed earlier. An ion-exchange mechanism has been reported to be the possible cause for the substitution of  $Na^+$  by  $K^+$  [44]. Since there is no increase of  $Na^+$  concentration either toward the back or the front of the CIGS, it is likely that Na is removed during CdS chemical bath deposition [44]. It is important to note that for the Ga/(Ga+In) profile, even though the overall composition is the same for both samples (as seen by XRF), there



is a slightly lower Ga/(Ga+In) content in the sample with no KF in the region probed by the DLTS, which might explain the lower energy for the traps observed by DLTS compared with the sample with KF PDT (0.56 eV versus 0.61 eV), as expected theoretically [131]. No statistically significant change in the Cu profile was observed between the two samples.

TABLE 4: The elemental composition of the CIGS thin films deposited on Mo coated SLG substrate with and without KF PDT from the XRF measurement.

Sample	Cu(at%)	In(at%)	Ga(at%)	Se(at%)
No KF	23.4	15.9	10.1	50.6
KF PDT	23.7	15.6	10.0	50.7

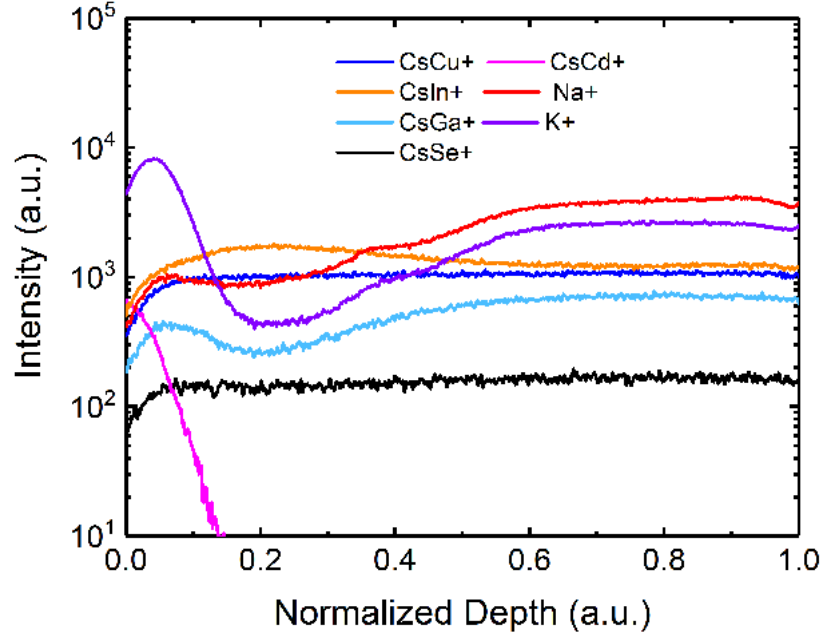


FIG. 20: Elemental depth profile of the CIGS film prepared on SLG/Mo substrate without KF post deposition treatment measured by SIMS [36].

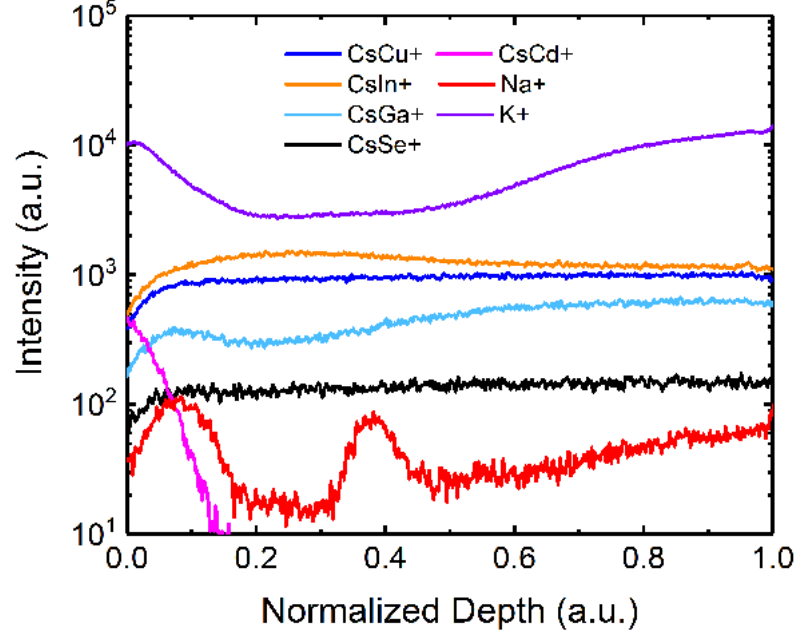


FIG. 21: Elemental depth profile of the CIGS film prepared on SLG/Mo substrate with KF post deposition treatment measured by SIMS [36].

#### 4.4 FORMATION OF DEFECT LEVELS

##### 4.4.1 CIGS GROWN ON ALUMINA SUBSTRATE

Figure 22 shows the defect level distribution for the CIGS film from DLTS measurement in the temperature range from 150 K to 375 K. A positive peak in the DLTS spectra at  $\approx 365$  K represents a majority carrier trap with a maximum density of  $4.46 \times 10^{14} \text{cm}^{-3}$  and  $3.94 \times 10^{14} \text{cm}^{-3}$  in KF untreated and KF treated samples respectively, with lambda correction to accurately obtain the DLTS measurement. The activation energy of this trap was determined to be  $E_v + 0.59 \pm 0.03$  eV from the Arrhenius plot. Figure 23 shows the DLOS spectra of the CIGS sample. In this case, a deep level was observed at  $E_v + 0.98 (\pm 0.03)$  eV with a density of  $3.0 \times 10^{15} \text{cm}^{-3}$  and  $2.61 \times 10^{15} \text{cm}^{-3}$  in KF untreated and KF treated samples, respectively, which is  $\approx 13\%$  lower concentration in the KF treated sample.

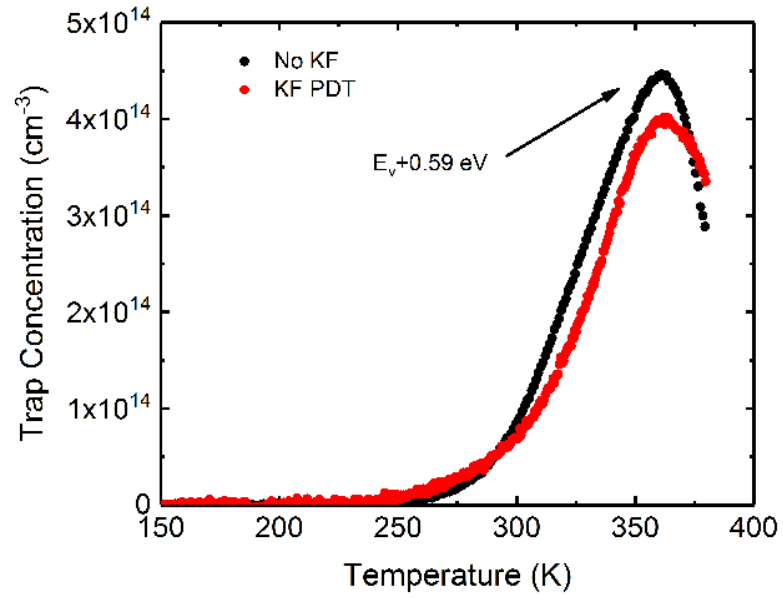


FIG. 22: Comparison of DLTS spectra of CIGS sample with and without KF PDT deposited on alumina/Mo substrate [73].

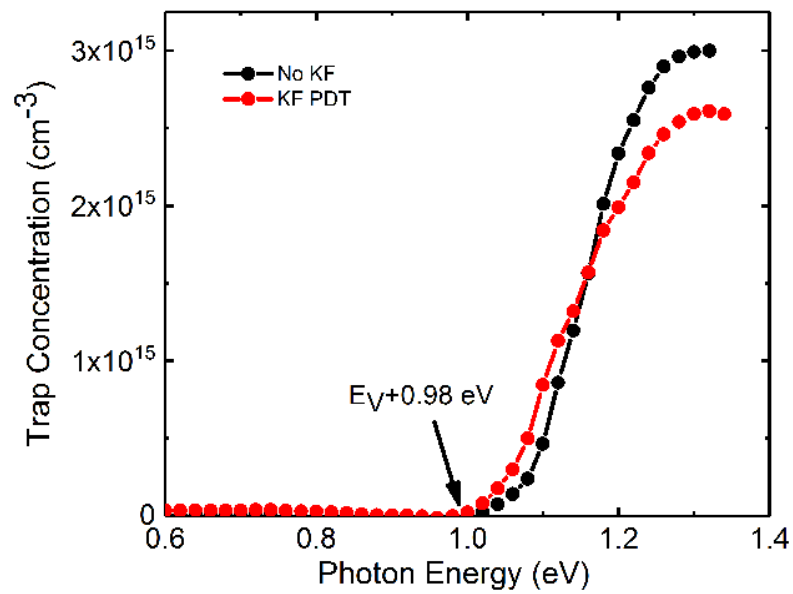


FIG. 23: Comparison of DLOS spectra of CIGS sample with and without KF PDT deposited on alumina/Mo substrate [73].

#### 4.4.2 CIGS GROWN ON SLG SUBSTRATE

Figure 24 shows the comparative DLTS spectra of the CIGS samples prepared on SLG substrates with and without KF PDT. The DLTS spectra resolved one majority carrier trap in both samples. The activation energy of the trap, as extracted from the Arrhenius plot (insert) was  $E_v+0.56(\pm 0.03)$  eV with cross section  $8 \times 10^{-18}$  cm<sup>2</sup> for the sample without KF and  $E_v+0.61(\pm 0.03)$  eV with cross-section of  $1 \times 10^{-17}$  cm<sup>2</sup> for the sample with KF PDT, while the concentration was  $1.2 \times 10^{14}$  cm<sup>-3</sup> without KF and  $1.1 \times 10^{14}$  cm<sup>-3</sup> with KF PDT. This defect may act as an effective recombination center because of its location close to the mid-bandgap. This  $E_v+0.56/0.61$  eV trap has been previously identified by different groups and attributed to different origins. A theoretical study by Wei et al. [106] shows that acceptor levels at  $E_v+0.61$  eV and  $E_v+0.58$  eV exist for CuGaSe<sub>2</sub> and CuInSe<sub>2</sub>, respectively, and are associated with Cu<sub>Ga,In</sub> defects. Similar conclusions were drawn by Zhang et al. [131] suggesting that the observed defects might originate from Cu<sub>Ga,In</sub> anti-site defects. It is important to note that, with a post-deposition KF treatment, the  $E_v+0.56/0.61$  eV trap concentration does not change significantly indicating that the  $E_v+0.56/0.61$  eV level is not sensitive to the KF PDT.

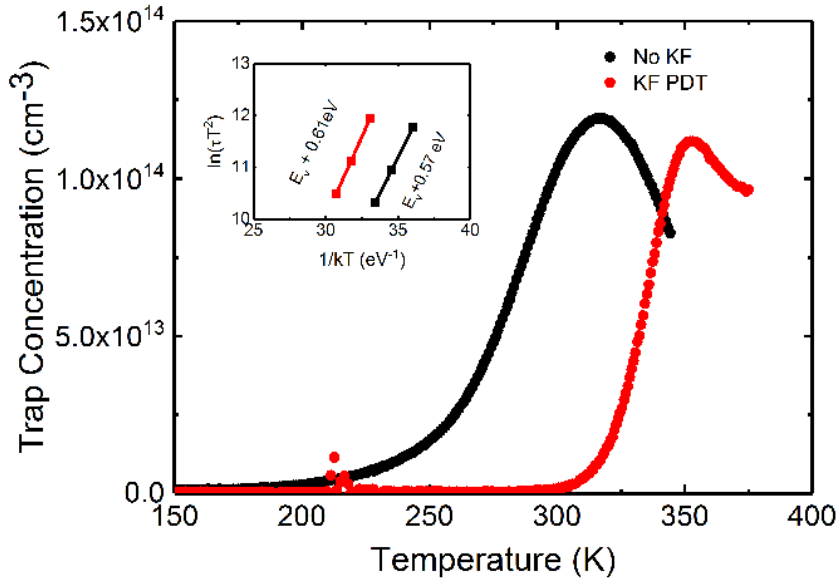


FIG. 24: Comparison of DLTS spectra of CIGS sample with and without KF PDT deposited on SLG/Mo substrate [36].

Scanning DLTS measurements were also performed to understand the spatial distribution of the  $E_v+0.56/0.61$  eV trap (Figure 25). During the scanning-DLTS measurement, the surface potential transients due to trap emission were recorded at each spatial location. A 0V fill pulse was applied to fill traps and the trap emission was measured at  $-2V$ . Similar to DLTS, the double boxcar approach was used to provide selectivity to a specific defect ( $E_v+0.56$  eV) where the change in surface potential  $\Delta SP = SP(t_2) - SP(t_1)$ , where the times are selected to match the time constant of the trap ( $\tau_p$ ) of interest at the scanning-DLTS measurement temperature using equation (26),

$$\tau_p = \frac{t_2 - t_1}{\ln\left(\frac{t_2}{t_1}\right)} \quad (26)$$

The two green lines in the topography images represent the approximate region where the depletion region modulated and where the scanning-DLTS is sensitive to traps. Comparing the topography and scanning DLTS map, one can see that the  $E_v+0.56/0.61$  eV trap is not uniformly distributed, but exhibits a strong trap emission in the inter-grain regions.

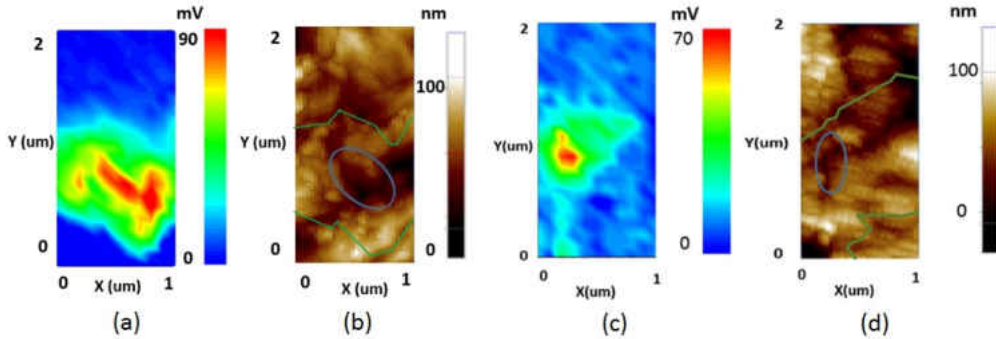


FIG. 25: (a) Scanning-DLTS map and (b) topography image of the CIGS sample without KF PDT. (c) Scanning-DLTS map and (d) topography image of the CIGS sample with KF PDT. The two green lines represent the approximate area where the depletion region is modulated [36].

To probe the trap states located in the upper half of the CIGS bandgap, DLOS measurement was performed. From the DLOS data, trap concentration ( $N_T$ ) were calculated using the step height of the DLOS signal given by equation 27,

$$N_T = 2N_A \times \frac{\Delta C}{C} \quad (27)$$

where  $N_A$  is the carrier concentration,  $\Delta C$  is the change in capacitance due to trap emission and  $C$  is the steady state capacitance [132]. Figure 26 shows the DLOS signal with one dominant trap level for both samples. To determine precisely the energy level of the DLOS deep trap, the optical cross-section was plotted as a function of energy and fitted by using the Lucovsky model [133]. From the optical cross-section fitting, an activation energy of  $E_v+0.99(\pm 0.03)$  eV was obtained for both samples. In contrast to the trap at  $E_v+0.56/0.61$  eV, however, the concentration of this trap is different from one sample to another, with approximately 35% lower concentration for the sample with KF PDT compared to untreated sample ( $2.9 \times 10^{14} \text{cm}^{-3}$  without KF and  $1.9 \times 10^{14} \text{cm}^{-3}$  with KF PDT). This second trap could contribute significantly to recombination in the material, especially for higher Ga contents where it would be located toward mid-bandgap [106]. A previous study by Repins et al. [134] has shown the presence of a similar deep trap with an activation energy of  $E_v+0.94$  eV in CIGS solar cells. It is important to note that for the Ga/(Ga+In) profile, even though the overall composition is the same for both samples (as seen by XRF), there is a slightly lower Ga/(Ga+In) content in the sample with no KF in the region probed by the DLTS, which might explain the lower energy for the traps observed by DLTS compared to the sample with KF PDT (0.56 eV Vs. 0.61 eV), as expected theoretically [131]. No statistically significant change in the Cu profile was observed between the two samples.

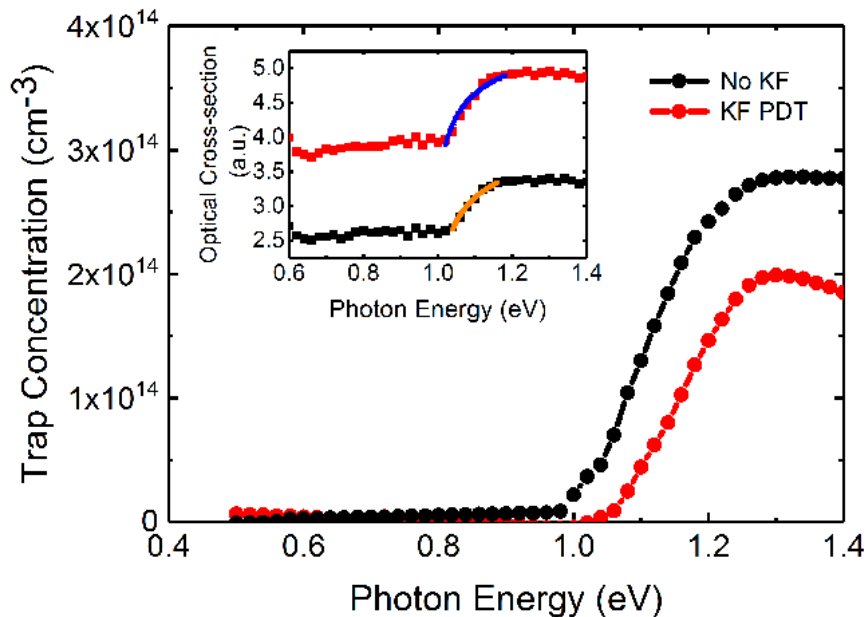


FIG. 26: Comparison of DLOS spectra of CIGS samples with and without KF PDT deposited on SLG/Mo substrate [36].

## 4.5 DEVICE RESULTS

### CIGS GROWN ON ALUMINA SUBSTRATE

Figure 27 shows the J-V parameters of the cells grown on an alumina substrate with and without KF PDT. It is evident that the KF treated samples have better power conversion efficiency, primarily due to the increase in open circuit voltage and fill factor (see Figure 29). The short circuit current is almost identical for both samples, which is also seen in the external quantum efficiency (EQE) plot (Figure 28). Figure 29 shows a representative J-V curve of the CIGS device with and without KF PDT. The K free sample showed a roll-over effect, which was eliminated in the KF treated sample. The roll-over effect is often observed in alkali-free (Na or K) samples [87, 135] and has been linked to a secondary diode at the Mo/CIGS back contact [135].

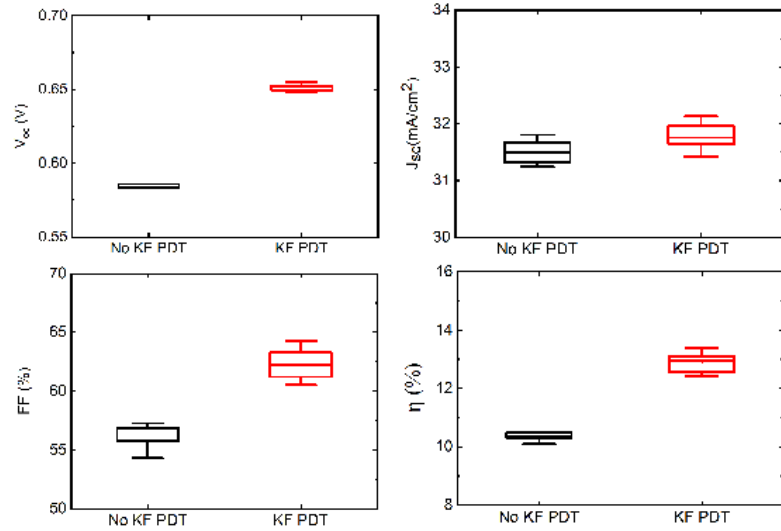


FIG. 27: Comparison of CIGS devices parameters with and without KF PDT prepared on alumina substrates without an anti-reflective coating. The overall gain in efficiency was observed in the KF treated samples mostly due to improvement in open circuit voltage and fill factor and a small increase in short circuit current.

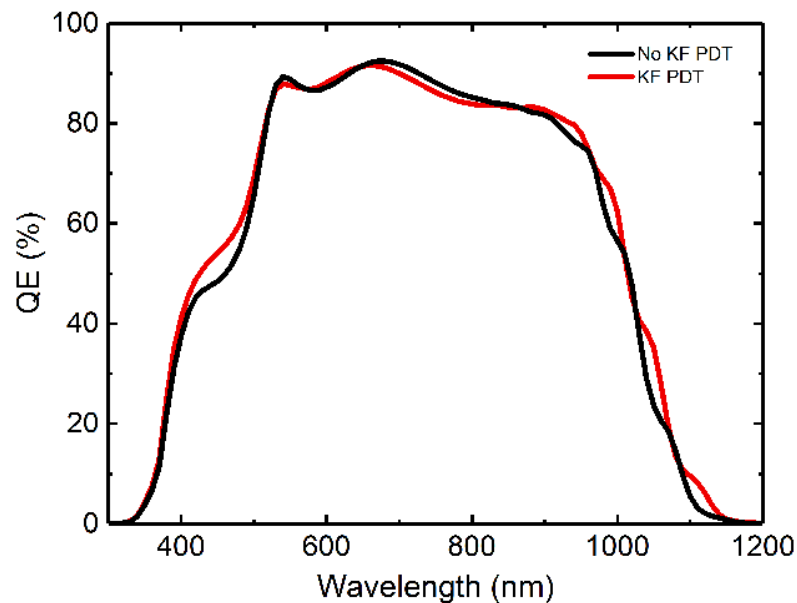


FIG. 28: Comparison of external quantum efficiency in the CIGS devices with and without KF PDT prepared on alumina substrates. A small variation in EQE response in the 400 nm-500 nm range is due to the small variation in the CdS thickness.



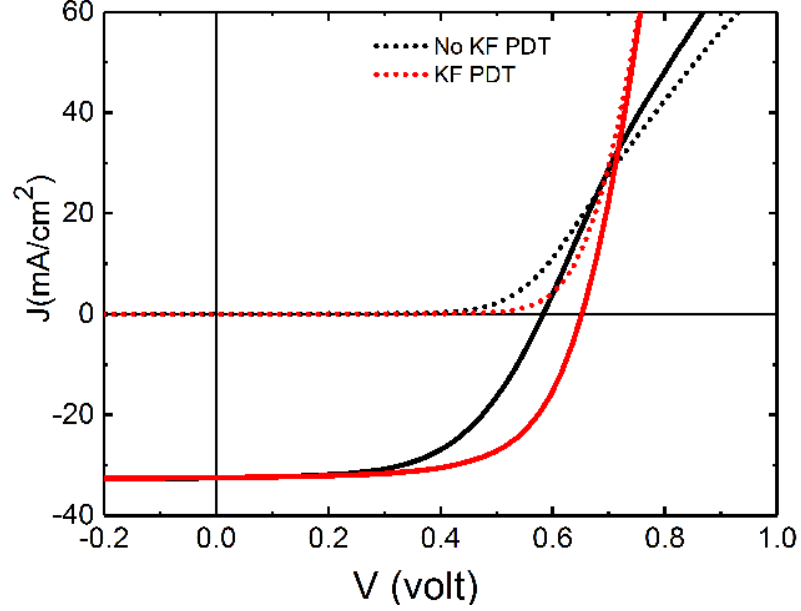


FIG. 29: Comparison of a current density-voltage plot of the CIGS devices with and without KF PDT prepared on alumina substrates. The roll-over effect seen in the device without KF treatment is corrected after KF post-deposition treatment [73].

### CIGS GROWN ON SLG SUBSTRATE

Solar cell devices were fabricated on SLG substrates for CIGS samples with and without KF PDT. Box plot (see Figure 30) shows the improvement in the device efficiency after KF PDT. The J-V measurements (Figure 31) show an improvement in the efficiency from 17.0% to 17.9% after KF PDT (measurements were made with a  $\text{MgF}_2$  anti-reflective coating). There is an improvement in the open circuit voltage ( $V_{oc}$ ) and fill factor (FF) after KF PDT (from 0.68 V to 0.70 V and 71.7% to 73.1%, respectively), although the samples have similar Ga contents as shown by the absorption cut off in the EQE (Figure 32) and the bandgap extracted from the extinction coefficient obtained from ellipsometry (Figure 17). Moreover, no appreciable change in short-circuit current density was observed between these samples as shown by EQE (Figure 32). The light J-V curves were fitted to a single diode model to extract the ideality factor ( $A$ ), saturation current density ( $J_o$ ), series resistance ( $R_s$ ) and shunt resistance ( $R_{sh}$ ) (Table 5). Minor improvements in all these parameters were observed after KF PDT, which contribute to the improvement of both  $V_{oc}$  and FF.

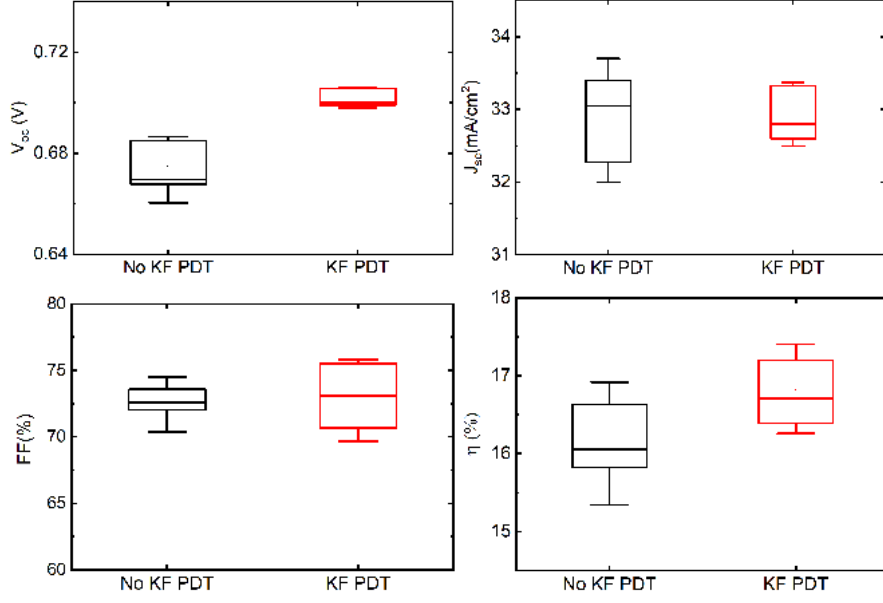


FIG. 30: Comparison of device parameters in the CIGS devices with and without KF PDT prepared on SLG substrates after  $\text{MgF}_2$  anti-reflective coating.

TABLE 5: Best cell parameters of the CIGS solar cells with and without KF PDT prepared on SLG with anti-reflective coating.

Parameter	Unit	No KF PDT	KF PDT
$\eta$	%	17.0	17.9
$V_{oc}$	mV	680	700
$J_{sc}$	$\text{mA cm}^{-2}$	34.8	35.0
FF	(%)	71.7	73.1
$R_s$	$\Omega - \text{cm}^2$	1.3	1.1
$R_{sh}$	$k\Omega - \text{cm}^2$	1.45	1.50
$J_o$	$\text{A cm}^{-2}$	$2 \times 10^{-8}$	$1 \times 10^{-8}$
A		1.92	1.87

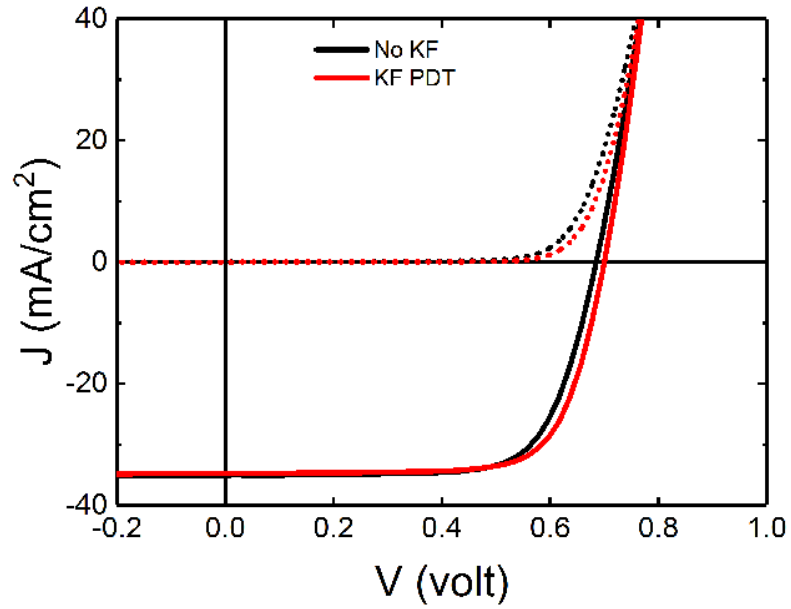


FIG. 31: Comparison of current density-voltage plot of the CIGS devices with and without KF PDT prepared on SLG substrates. The J-V curve shows the improvement in open-circuit voltage for the KF PDT sample [36].

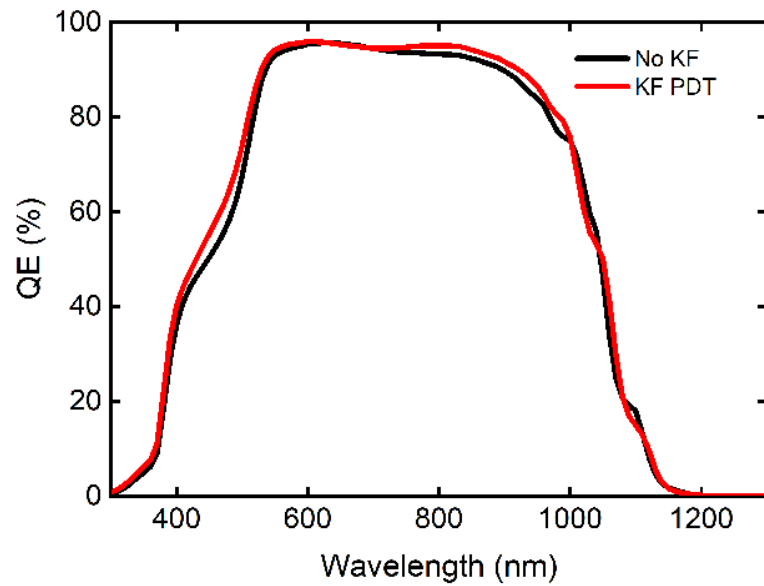


FIG. 32: Comparison of external quantum efficiency in the CIGS devices with and without KF PDT prepared on SLG substrates after MgF<sub>2</sub> anti-reflective coating.

## 4.6 SUMMARY

We investigated the evolution of CIGS films and devices properties with KF post-deposition treatment. RTSE analysis was used to monitor the deposition process and extract structural parameters such as bulk layer thickness, surface roughness and optical properties such as dielectric function and bandgap. The critical point analysis performed on the extracted dielectric functions before and after the KF post deposition treatment indicated a shift in the critical point energy of  $E_1(A)$ . This suggests a Ga deficiency at the surface based on comparison with previous calculations linking the shift in the critical point energy with the gallium content in the CIGS film. The compositional depth variations as studied by SIMS did not show major differences in the main constituent elements namely Cu, In, Ga, and Se. However, we did observe Na substitution by K in the case of the film containing Na prior to the KF PDT. Potassium was found to diffuse evenly throughout the CIGS film depth prepared on both alkali free (alumina) and alkali containing (SLG) substrates. A combination of DLTS and DLOS measurements revealed two traps around  $E_v+0.55$  eV and  $E_v+0.99$  eV, regardless of the presence or absence of alkali in the deposited films. The mid-bandgap defect close to  $E_v+0.55$  eV, whose origin has not been identified yet, was observed to show a higher response in some inter-grain regions by scanning DLTS method but did not show a significant change in concentration due to alkali treatment. This gives an indication that regardless of its origin, passivation of this defect may not be achieved through the alkali incorporation. However, another trap state present in all studied CIGS films did show a reduction in the concentration after KF treatment. This observation indicates passivation of the  $E_v+0.99$  eV trap is indeed one of the reasons for the improvement in the electronic quality of the KF treated samples, contributing to the overall improvement in the device performance.

## CHAPTER 5

# RbF POST DEPOSITION TREATMENT IN CIGS SOLAR CELLS

After discovering that KF PDT can produce better CIGS solar cell devices, a new motivation existed to deliberately introduce heavier alkali elements, such as RbF and CsF, after CIGS growth. This in fact, resulted in a series of record efficiency CIGS solar cells within a short period of time [4]. Record efficiency device with RbF PDT [45] was attributed at the time to the improvement of the diode quality. RbF and KF PDT also allowed a reduction of the CdS buffer layer and showed similar improvement in the device parameters [47]. The CIGS/CdS interface characteristic was studied [136], and it was concluded that although RbF PDT allows for reduced CdS thickness to be used without compromise in device performance, further reduction in the thickness may be costly because of formation of chemically and electronically inhomogeneous interface structure. K and Rb were observed to accumulate in a nanopatterned copper poor secondary phases at CIGS surface which was believed to be  $\text{KInSe}_2$  or  $\text{RbInSe}_2$  in the respective case, according to theoretical calculations [137]. The CIGS composition-dependent effect of RbF PDT was also studied [138]. Significant surface modification was reported to occur in the In-containing film with relatively higher surface roughness due to pores formation; however, In-free film did not show such surface morphology. An increased amount of indium and gallium oxides was observed at the RbF treated CIGS surface and they partly or wholly got removed during the CdS deposition [139]. Furthermore, RbF PDT was found to act differently than KF PDT to the CIGS surface with much weaker copper depletion at the surface and no changes in the gallium profile in the same region [139], while others reported both Cu and Ga depletion [51]. It was suggested that the presence of rubidium and/or fluorine might provide a chemical driving force for the mobility of Na [51]. The formation of  $\text{RbInSe}_2$  was observed at the CIGS surface [50]. Since no RbF related compound was detected in the  $\text{CuGaSe}_2/\text{CdS}$  interface, only In was found to participate in the formation of Rb-related compound. The presence of Rb traces in the CIGS/CdS interface along with In enrichment and Cu depletion in the

RbF treated samples were reported [140]. Additionally, RbF PDT sample showed a higher concentration of Rb and lowered amount of Na and K in the grain boundaries compared to the untreated sample, which further suggested the replacement of lighter alkali element by Rb. At the same time pronounced Cu depletion was observed in the grain boundaries which is believed to act beneficially by acting as hole barriers, improving the grain boundary characteristics leading to device improvement.

In this context, we studied the electronic defect spectrum in the RbF treated sample to relate the improvement in the electronic quality of the material to the device improvement. In the previous chapter, we have shown that KF treatment leads to the defect passivation in both the Na containing and Na-less CIGS thin films. In this chapter, we extend a similar comparative study on traps characterization between the CIGS with and without another heavier alkali element, incorporated by RbF post-deposition treatment (PDT). The observed modifications in the defect level and density due to RbF treatment in the CIGS film are then correlated with device performance. Another motivation to perform this study was to answer whether RbF shows a similar effect as KF PDT on the CIGS defect spectrum or behaves differently. We have analyzed the results more closely with additional characterizations including time-resolved photoluminescence, allowing us to compare the minority carrier lifetime, and temperature dependent current-voltage measurement used to locate where the dominant recombination occurs and whether RbF incorporation makes any difference. The experimentally obtained data are utilized to model the devices using SCAPS simulation, and the contribution of component parameters varied in the simulation are quantitatively discussed in the context of improvement of the device parameters.

## 5.1 EXPERIMENTAL DETAILS

CIGS absorber layers about 2.2  $\mu\text{m}$  thick were grown on Mo-coated soda lime glass (SLG) substrates by a three-stage process [141]. The substrate temperature in the first stage was maintained at 400°C and ramped up to 600°C for the second and the third stage of the deposition. Se vapor was supplied during both growth and the cool down process until the substrate temperature fell below 300°C. During cool down, 10-20 nm of RbF was evaporated at 350°C for RbF post deposition treatment(PDT) in the presence of Se vapor. Samples were rinsed in 2N ammonium hydroxide solution for 1 minute before CdS deposition to remove excess RbF from the

surface. The cells were completed by depositing a CdS ( $\approx 50$  nm) buffer layer using chemical bath deposition. A combination of i-ZnO (60-100 nm) and ITO (200-250 nm), both deposited by RF magnetron sputtering, was used as transparent conducting layer. The Ni/Al/Ni front contacts were deposited by electron beam evaporation. Finally, solar cells with active areas of  $0.5 \text{ cm}^2$  were isolated by mechanical scribing. The trap states in the lower half of the bandgap were probed by DLTS, which utilizes the analysis of capacitance transients due to the emission of the trapped carriers [118]. Additionally, DLOS was used to probe the deep trap states in the upper half of the bandgap, where the slower thermal emission limits the sensitivity of the DLTS measurements [132]. The information about the activation energy of the trap states, their concentration and capture cross-section can be obtained from the DLTS measurement; DLOS measures the trap level, concentration, and optical cross section. Experimental details for the DLTS and DLOS measurements have been described previously [132]. The device performance was evaluated by in-house current-density/voltage (J-V) measurements under AM 1.5G illumination with a light intensity of  $100 \text{ mW/cm}^2$  at  $25^\circ\text{C}$ . Temperature-dependent J-V measurements were performed from room temperature down to 200 K to extract activation energies for dominant recombination processes. Capacitance-voltage (C-V) measurements were performed to obtain the effective hole carrier concentrations in the CIGS films. SIMS measurements were used to obtain the elemental depth profile in the CIGS film and XRF was used to extract bulk composition.

## 5.2 COMPOSITION AND ELEMENTAL DISTRIBUTION

Table 6 shows the elemental composition from XRF of the reference sample and the RbF treated sample, which confirms a similar composition for both of them. SIMS measurements (Figure 33 and Figure 34) were performed on both samples and showed that the Rb is distributed throughout the CIGS film. When the Na and Rb profiles are compared with respect to the corresponding  $\text{CsCu}^+$  ion intensity in the matrix, one can see that the Na intensity in the RbF treated film is lower. This suggests a partial substitution of Na by Rb, similar to what is happening with K, despite the ionic radii difference. This is believed to occur due to an ion exchange mechanism [142]. Rb was observed to accumulate at the Mo/CIGS as well as the CIGS/CdS interfaces. SIMS measurements also indicate that there is a modification of the CIGS surface ( $\approx$  first 40 nm) after RbF PDT, with an increase in Cu and In

near the surface (Figure 34).

TABLE 6: The elemental composition of the CIGS film with and without RbF PDT from XRF measurement.

Sample	Cu(at%) (at%)	In(at%) (at%)	Ga(at%) (at%)	Se(at%) (at%)
w/o RbF	23.5	17.5	9.8	49.2
RbF PDT	23.3	16.9	9.9	49.9

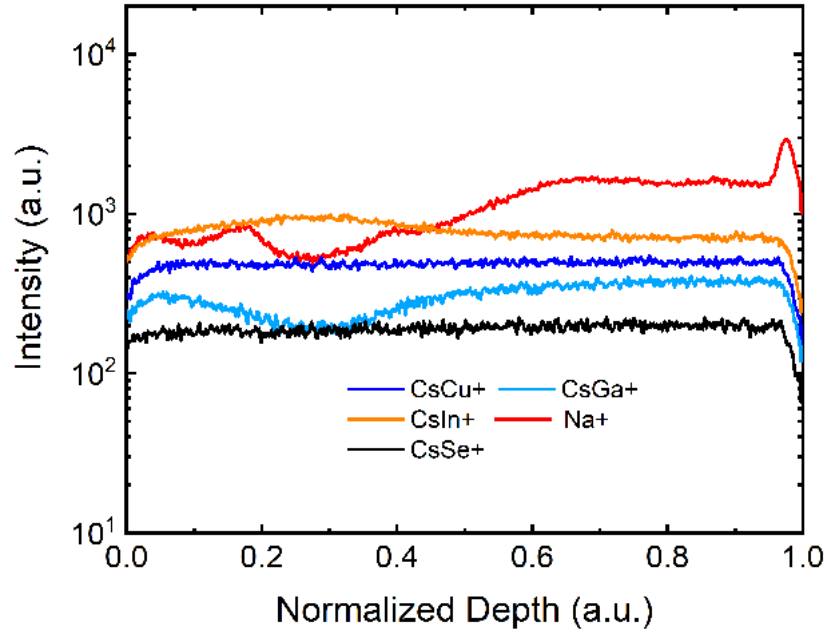


FIG. 33: Elemental depth profile of the CIGS film prepared on SLG/Mo substrate with no post deposition alkali halide treatment measured by SIMS (reference sample) [74].



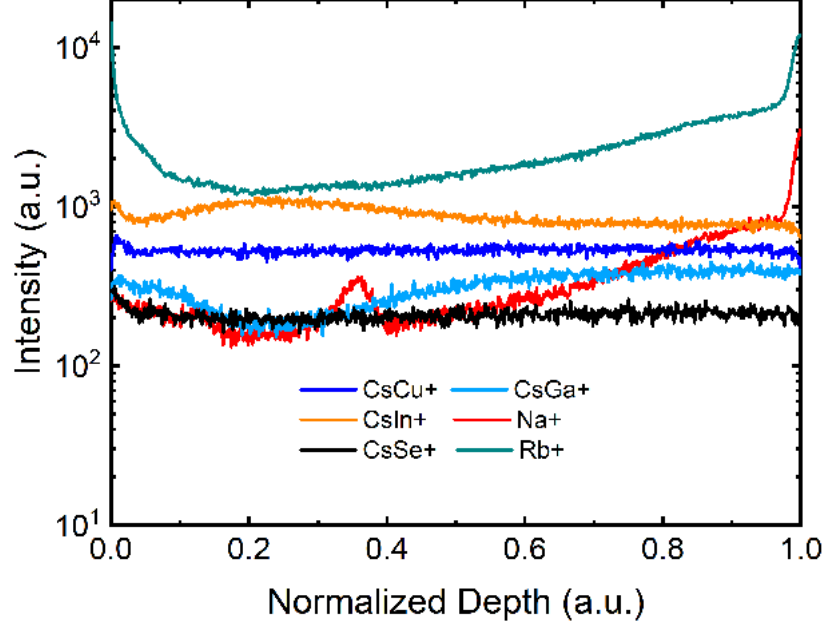


FIG. 34: Elemental depth profile of the CIGS film prepared on SLG/Mo substrate with RbF post deposition treatment measured by SIMS [74].

### 5.3 DEVICE RESULTS

Solar cells were fabricated with the process described in the previous section. Overall, an improvement in  $V_{oc}$  was observed for all cells following RbF treatment (Figure 35) with a small decrease in fill factor (FF). The J-V characteristics of the best cells without antireflection coatings are shown in Table 7 and corresponding J-V curves are shown in Figure 36. The improvement in the device performance after RbF PDT was due to gain in the  $V_{oc}$ . EQE measurements (Figure 37) confirm that there was no change in the overall current of the devices after PDT and indicate a nominal bandgap of 1.16 eV. Both this measurement and the XRF measurement indicate that the increase in  $V_{oc}$  is not due to an increase in the bandgap.

A one diode model fit to the J-V measurement shows a decrease in both reverse saturation current and diode quality factor in the RbF treated samples (Table 7), while there is a small increase in both series resistance (from 0.5 to 0.7  $\Omega\text{cm}^2$ ) and shunt conductance from (0.66 to 0.71  $\text{mS}\cdot\text{cm}^{-2}$ ). This indicates that the  $V_{oc}$  increase is mostly due to the enhancement of the diode quality and lower recombination,

while the slight decrease in FF is possibly due to changes in both series and shunt resistances.

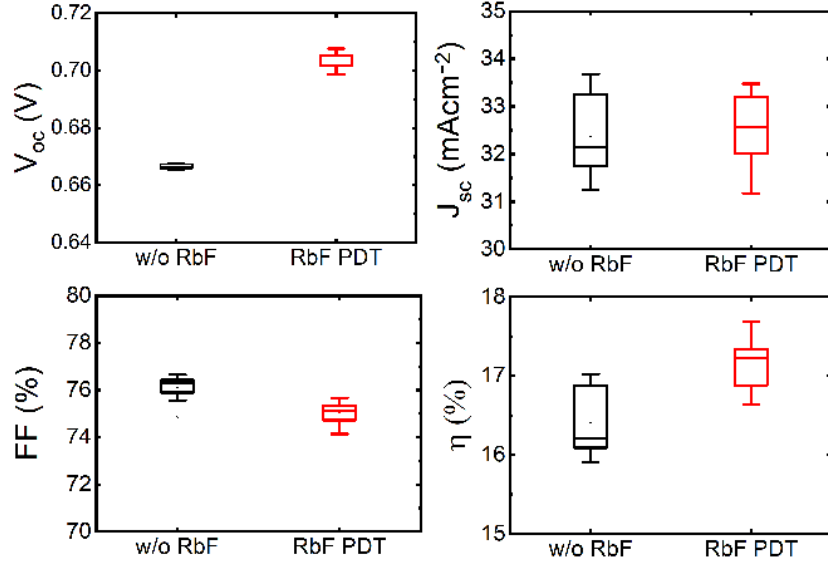


FIG. 35: Summary of the photovoltaic parameters of the device without (black) and with (red) RbF PDT[74].

TABLE 7: Photovoltaic characteristics of the best cell studied in this experiment.

Sample	$\eta$ (%)	$V_{oc}$ (mV)	$J_{sc}$ ( $\text{mA}/\text{cm}^2$ )	FF (%)	A	$J_0$ ( $\text{mA}/\text{cm}^2$ )
w/o RbF	17.0	667	33.7	75.9	1.70	$9 \times 10^{-6}$
RbF PDT	17.7	704	33.5	75.0	1.67	$3 \times 10^{-6}$

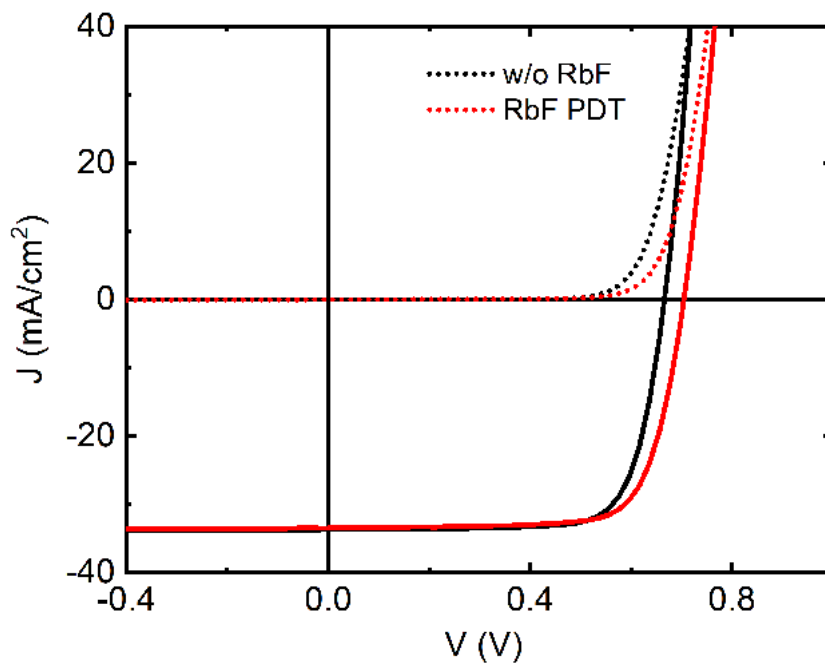


FIG. 36: Representative current density-voltage curves for the reference and the RbF treated CIGS device[75].

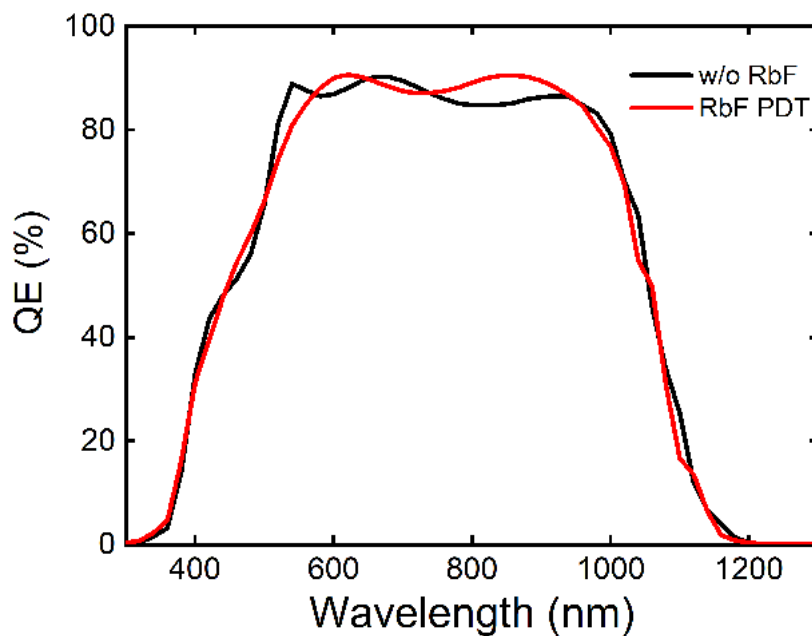


FIG. 37: Representative external quantum efficiency curves of the reference and the RbF treated CIGS device [74].

Figure 38 shows the temperature dependent J-V measurement of the investigated samples as well as the  $V_{oc}$  as a function of temperature with lines extrapolated to 0K. When  $R_{sh}$  is large, which is our case, one can obtain the activation energy of the dominant recombination mechanism ( $E_a$ ), according to equation (28),

$$V_{oc} = \frac{E_a}{q} - \frac{Ak_B T}{q} \ln \left( \frac{J_{oo}}{J_{sc}} \right) \quad (28)$$

where  $q$ ,  $A$ ,  $k_B$ ,  $T$ ,  $J_{oo}$ , and  $J_{sc}$  are the electron charge, diode quality factor, Boltzmann constant, temperature, recombination current density prefactor and the short-circuit current density, respectively. When  $E_a$  is less than the bandgap energy ( $E_g$ ), the devices are dominated by interface recombination whereas if  $E_a$  is equal to  $E_g$ , as observed here, the devices are dominated by bulk recombination [143]. As seen in Figure 38, the activation energies of the reference device and the RbF treated device are similar and equal to the band gap, which suggests that Shockley-Read-Hall (SRH) recombination in the CIGS is prevalent in both samples (since  $A > 1$ ). The insert shows that no roll-over is observed even at low temperature for both samples, so a back-contact diode is not a detrimental factor in either sample.

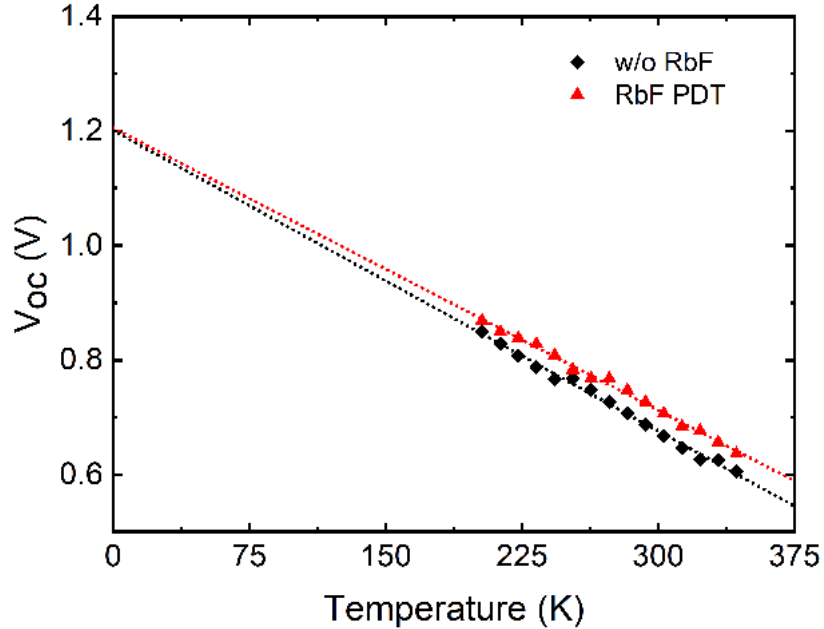


FIG. 38: Light temperature dependent J-V plot for reference device and the RbF treated device [74].

#### 5.4 CHARACTERIZATION OF DEEP LEVEL TRAPS

To better understand the origin of the diode enhancement, several film and device characterizations were performed to try to assess the evolution of the majority carrier concentration ( $N_A$ ), minority carrier lifetime ( $\tau_n$ ) and deep-level trap characteristics ( $N_T$ ,  $\sigma_T$ ), as they all impact  $J_0$  and  $A$ . Fast C-V measurements at  $2000 \text{ Vsec}^{-1}$  sweep rate provided the majority carrier (hole) concentration (Figure 39) [144]. Taking the minimum of the doping concentration of the reference device and the RbF treated device, an increase in the hole concentration by  $1.8\times$  in RbF PDT sample was obtained. The increase in  $V_{oc}$  can be correlated with the higher carrier concentration, which corresponds to a greater built-in voltage. The contribution due to increase in hole concentration in the  $V_{oc}$  can be estimated by using the following equation 29 [142] (assuming all other parameters constant and low injection),

$$\Delta V_{oc} \approx \frac{k_B T}{q} \ln \left( \frac{N_2}{N_1} \right) \quad (29)$$

where,  $N_1$  and  $N_2$  are the hole concentration in the reference sample, and RbF treated samples, respectively. The expected increase in  $V_{oc}$  value of approximately 15 mV due to increase in hole concentration is much lower than the experimentally measured  $V_{oc}$  increase of nearly 30 mV. Therefore, the increase in hole concentration does not solely explain the  $V_{oc}$  enhancement in the RbF treated devices.

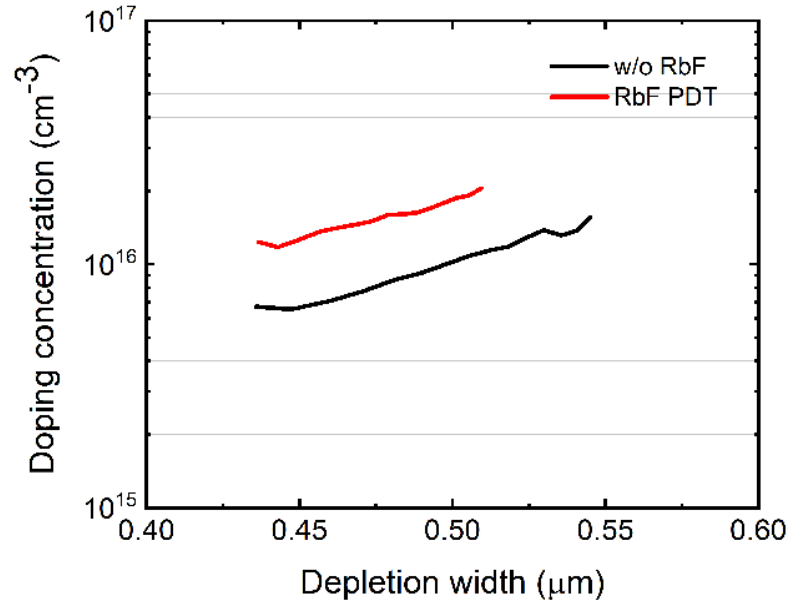


FIG. 39: Doping concentration measured by C-V measurement on reference and RbF PDT devices[74].

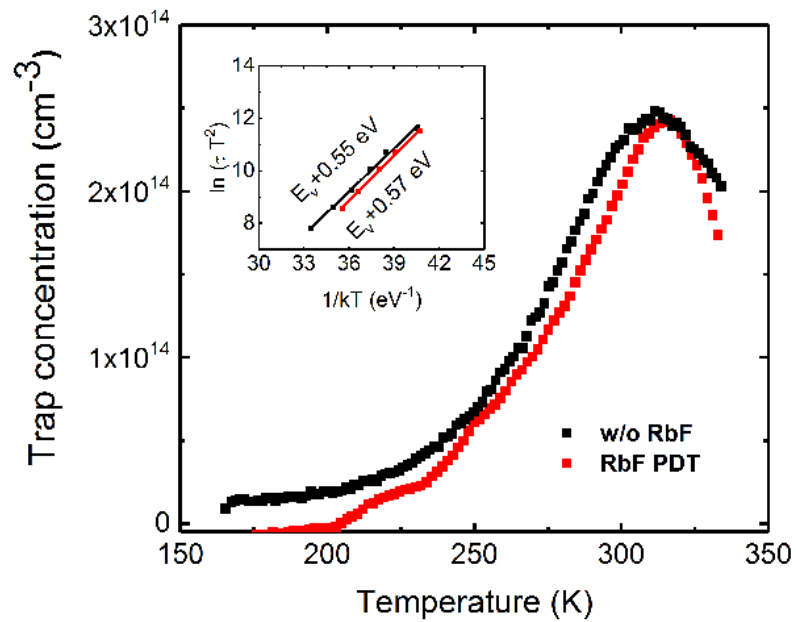


FIG. 40: Comparison of DLTS signal of the reference cell with RbF PDT CIGS solar cell. An  $E_v+0.55$  eV trap was observed in the reference cell, while a  $E_v+0.57$  eV trap was observed in the RbF treated cell [74].

In devices limited by SRH recombination, a higher concentration of deep-level traps controls  $V_{oc}$ , most effectively if the trap is located at mid-bandgap. The transient signals were analyzed by the double boxcar method using rate windows between 0.8 to 2000  $\text{sec}^{-1}$ . Results are shown in Figure 40. The trap energy and the capture cross-section were obtained from the Arrhenius plots. A single positive peak (majority carrier trap) was measured at  $\approx 320$  K, with a position of  $E_v+0.55(\pm 0.03)$  eV for the reference sample and  $E_v+0.57(\pm 0.03)$  eV for the RbF treated sample with a trap concentration of  $2.4 \times 10^{14} \text{ cm}^{-3}$  and capture cross-section of  $6 \times 10^{-17} \text{ cm}^2$  for both samples. To obtain the accurate DLTS detected trap concentration, lambda effect [119] was considered here. The trap around  $E_V+0.57/0.55$  eV has been identified frequently in CIGS samples [17, 145, 146]. Our previous study via scanning-DLTS (see chapter 4) has shown, by superimposing the trap distribution maps with the topography, that the traps are localized at or very near a portion of the grain boundaries [36, 147]. The origin of this defect level has not been identified yet, although various sources of origin including In vacancies,  $\text{Cu}_{(\text{Ga},\text{In})}$  antisite defects [131] and foreign impurity contributions have been discussed [148]. However, this trap around  $E_V+0.57/0.55$  eV does not affect the difference in device efficiency, between the reference sample and the RbF treated sample, based on the similarity of concentrations and cross-sections.

DLOS involves the analysis of photocapacitance transient as a function of incident photon energy arising from deep level photoemission in the depletion region of the diode. The concentration of the deep trap detected by DLOS is calculated from the magnitude of the total steady state photocapacitance using equation 27. DLOS measurements are compared for the reference and RbF treated samples in Figure 41. The DLOS spectra reveal a trap level at  $E_V+0.99(\pm 0.03)$  eV with a concentration of  $\approx 5.3 \times 10^{15} \text{ cm}^{-3}$  and  $\approx 4.0 \times 10^{15} \text{ cm}^{-3}$  in the reference and Rb treated samples, respectively. This corresponds to a  $1.3 \times$  higher concentration in the reference sample.  $E_V+0.99$  eV traps have been observed previously in CIGS films, regardless of the growth process or Ga content and attributed to  $(V_{\text{Se}}-V_{\text{Cu}})$  divacancy complex [17, 60, 147]. However, the defect density has been found to decrease with alkali treatment [36], in agreement with what was observed in this study. Since it has been observed that Rb primarily segregates to grain boundaries [149], it is reasonable to assume that Rb passivates the  $E_v+0.99$  eV trap on these locations and thus enhances  $V_{oc}$ .

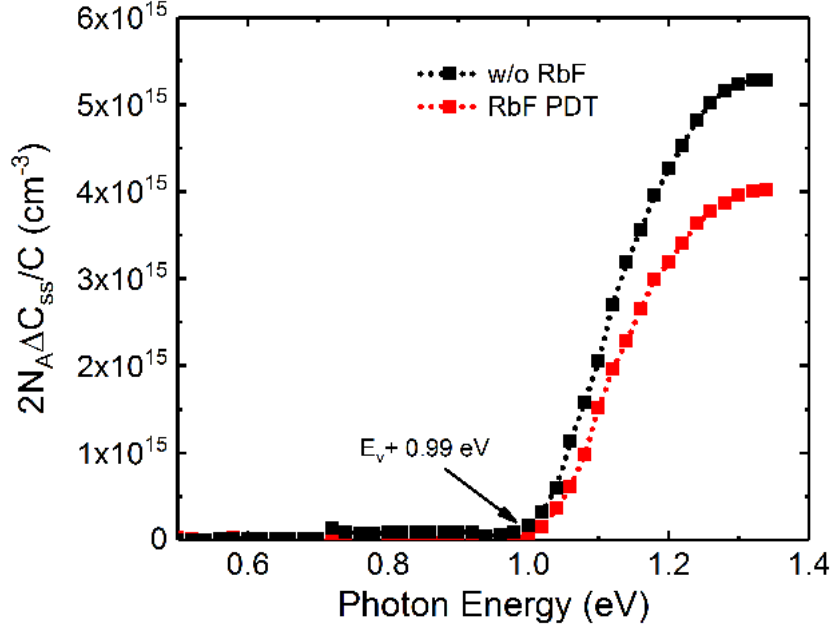


FIG. 41: Comparison of DLOS signal of the reference cell with RbF PDT CIGS solar cell. The  $E_v + 0.99$  eV trap was observed in both samples [74].

## 5.5 PHOTOLUMINESCENCE MEASUREMENT

To correlate the effects of both the change in majority carriers and deep-level trap concentrations, lifetime measurements were performed by TRPL. Figure 42 shows the TRPL results on the reference and RbF treated samples using an excitation laser of 680 nm. TRPL was measured on CdS-coated CIGS samples to prevent air-induced degradation [66]. A single exponential decay function was used to fit the decay curve for both samples, using the following equation (30),

$$I(t) = N e^{-\frac{t}{\tau}} \quad (30)$$

with  $N$  and  $\tau$  as the fitting parameters. The minority carrier lifetime for the reference sample was  $48 \pm 1$  ns and for the RbF treated samples was  $57 \pm 1$  ns. The longer PL decay time correlates well with the  $V_{oc}$  improvement in the Rb treated samples. Assuming that Auger recombination is not a dominant mechanism in CIGS films [150], the PL lifetime can be expressed as in equation (31),

$$\frac{1}{\tau} = B N_A + \sigma_T N_T V_{th} \quad (31)$$



where  $\tau$  is the lifetime,  $B$  is a fitting parameter,  $N_A$  is the majority carrier concentration,  $\sigma_T$  is the capture cross section for the traps,  $N_T$  is the trap concentration and  $V_{th}$  is the thermal velocity. Assuming  $B$  and  $V_{th}$  do not change between the two samples, and with the measured values for our samples, the extracted values of  $B$  and  $V_{th}$  are  $2.7 \times 10^{-10} \text{ cm}^3 \text{ sec}^{-1}$  and  $3.6 \times 10^6 \text{ cm sec}^{-1}$ , respectively. Both are smaller than the value reported in [150, 151]. Assessing the respective contribution of the majority carrier and the deep-level traps, one can see that the reduction in deep-level trap density is the major contributor to the increase of lifetime.

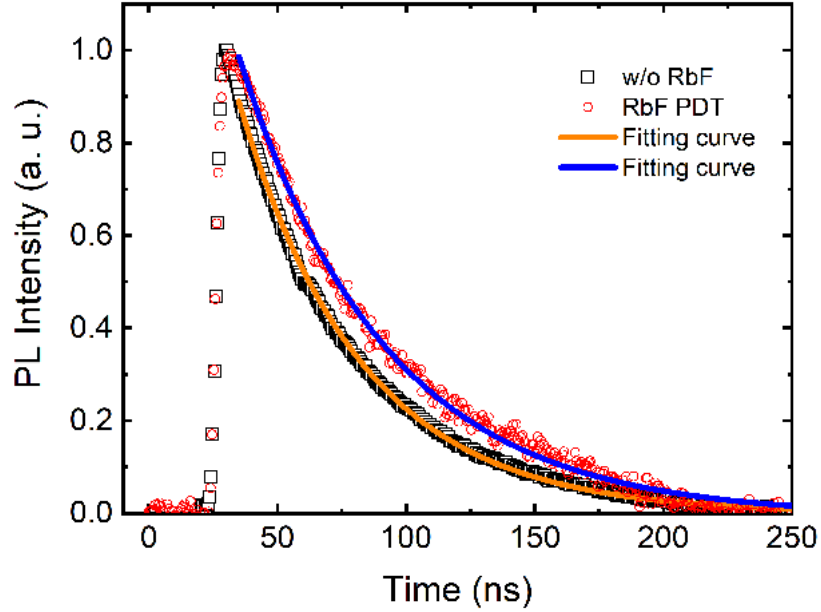


FIG. 42: TRPL decays for the reference sample (black square box) and the RbF treated sample (red circle). Dotted lines show the measured data while the solid lines show the corresponding single exponential fit to the decay curve [74].

## 5.6 SCAPS SIMULATION RESULTS

In order to assess the validity of our interpretation, the SCAPS simulation software was used for device simulation. The starting parameters for the simulation were adopted from [152] with the following modifications: CIGS thickness was set to  $2.2 \mu\text{m}$  with a double Ga grading, as observed in SIMS profiles (Figure 33). The donor density in the CdS was set to  $4 \times 10^{16} \text{ cm}^{-3}$  instead of  $1 \times 10^{16} \text{ cm}^{-3}$ . Other

modified parameters based on the experimental data are given in Table 8.

TABLE 8: Parameters used in the SCAPS simulation

Parameter	Unit	Reference cell	RbF PDT
$N_A$	$\text{cm}^{-3}$	$6.5 \times 10^{15}$	$1.16 \times 10^{16}$
$N_{E_v+0.57/0.55eV}$	$\text{cm}^{-3}$	$2.4 \times 10^{14}$	$2.4 \times 10^{14}$
$\sigma_{E_v+0.57/0.55eV}$	$\text{cm}^2$	$1.0 \times 10^{-15}$ (electron), $6.0 \times 10^{-17}$ (hole)	
$N_{E_v+0.99eV}$	$\text{cm}^{-3}$	$5.3 \times 10^{15}$	$4.0 \times 10^{15}$

With these modifications, a good fit was obtained for the reference device (as shown in Figure 43), which is represented by the w/o RbF simulated curve. To model the RbF treated sample, all other parameters were held identical except the acceptor density, the trap energy level and concentration, and the series resistance, which were obtained experimentally. With these modifications, the RbF simulation curve was obtained. This simulation shows an enhancement of  $V_{oc}$  by  $\approx 17$  mV. Another mechanism (such as lower interface recombination velocity) due to surface modification, as observed here by SIMS and by x-ray photoelectron spectroscopy in other study [47, 153], has to be taken into account to fully fit the experimental data.

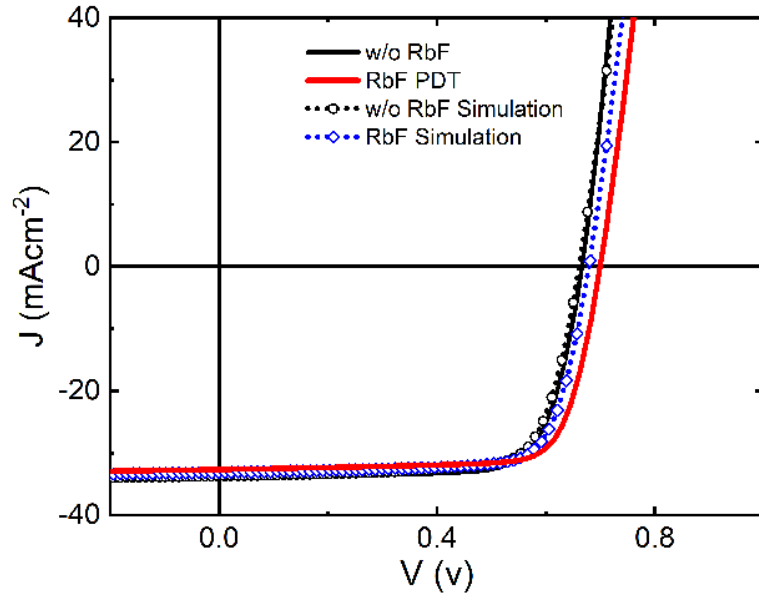


FIG. 43: The measured and simulated J-V curves of the reference and RbF treated CIGS solar cells [74].

## 5.7 SUMMARY

Alkali halide post-deposition treatments have become a driving force in the continuing enhancement of CIGS solar cell efficiencies. To fully understand its effect and how to enhance not only lab-scale devices but also manufacturing-scale modules requires a better understanding of the effect of these treatments on the device. We have shown that RbF PDT modifies the film composition by substituting Rb in part for Na. It also enhances  $V_{oc}$  by modifying the diode quality factor and reverse saturation current, while keeping the SRH recombination constant. No simple mechanism can, however, explain this change, as the majority carrier concentration increases while the deep-level trap density at  $E_V+0.99(\pm 0.03)$  eV decreases. The deep-level trap density at  $E_V+0.55(\pm 0.03)$  eV is not modified. The evolution of the lifetime, increasing by 10 ns after RbF PDT, also explains in part the increase in  $V_{oc}$ . However, the simulation and calculation show that only by considering surface modification (seen here by SIMS), can one fully assess the modifications due to post-deposition treatment.

## CHAPTER 6

# IMPACT OF DAMP HEAT STRESS ON MOLYBDENUM BACK CONTACT

Molybdenum thin films have been used for many years as the back contact for the fabrication of CIGS solar cells, and, to date, continue to be used in high-efficiency CIGS devices [88]. This material presents many advantages, including low contact resistance with CIGS layer, mechanical stability during high-temperature CIGS growth process, good adhesion with soda lime glass (SLG) substrate, viable pathways for Na diffusion from SLG, chemical inertness and formation of a beneficial  $\text{MoSe}_2$  interfacial layer [88, 89]. While the susceptibility of Mo to degrade in a humid environment is a potential concern for the long-term stability of these solar cell devices [53], modification of the physico-chemical properties of Mo back contact also plays a crucial role in the sodium out-diffusion during high-temperature growth of the CIGS absorber layer [154, 155, 156]. Researchers have shown that the surface oxidation of Mo thin films results in the loss of both conductivity and reflectivity [157, 158], while it can also prevent the formation of a beneficial interfacial  $\text{MoSe}_2$  [159]. Several studies have therefore been conducted to investigate the effect of oxidation, aging, pre-heating, damp heat and moisture on the properties of Mo thin films and consequently to the CIGS solar cell fabricated on them in some cases [53, 160, 161]. Pern et al. [160] observed substantial structural and morphological changes in Mo under damp heat condition resulting in blue-yellowish rust formations, pinholes, microcracks, and increased sheet resistance. The discolored surface was found to be soluble with deionized water, which leads authors to believe the blue-yellow appearance was due to the formation of  $\text{MoO}_3$  and/or  $\text{Mo}(\text{OH})_3$  species. Theelen et al. reported visible degradation effects in the form of discoloration in the Mo surface and random colored spots after several hours of Mo exposure to  $85^\circ\text{C}/85\%$  relative humidity [162]. Degraded Mo contained a thick non-conductive molybdenum oxide and suboxide layer on top of metallic Mo. Degraded Mo was found to expand in volume and showed cracks along with needle-like structures. Additionally, Mo deposited at high Ar pressure

by magnetron sputtering was found to degrade at a faster rate compared to Mo deposited at low Ar pressure. The selenization of Mo reduced the degradation rate. In another study by the same group, oxidized Mo was investigated for chemical composition which showed the formation of  $\text{Na}_x\text{MoO}_3$  due to intercalation of  $\text{Na}^+$  [53]. It was suspected that the formation of insulating  $\text{MoO}_3$  or intercalation of  $\text{Na}^+$  in  $\text{MoO}_3$  could influence the band alignment with CIGS, while severe loss of solar cell efficiency remains a possibility due to increase in series resistance for example.

Reference [159] showed that the molybdenum oxide layer could be used to limit the thickness of  $\text{MoSe}_2$  to impede the excessive formation of  $\text{MoSe}_2$ , while reference [154] showed that the CIGS solar cell grown on oxidized Mo had difficulty with Na diffusion. Meanwhile, the effect of Mo oxidation on device performance is not entirely consistent, as some researchers observed benefits to it while others find degradation [154, 161, 163]. In this chapter, Mo thin films exposed to moisture are studied, with an emphasis on how the modifications of their properties impact device performance. Another emphasis is on the alkali diffusion characteristics within the layer and subsequently deposited CIGS thin film. Modification in micro-structural properties, change in film morphology, optical and electrical modifications were observed via X-ray diffraction, atomic force microscopy, transmission electron microscopy, spectroscopic ellipsometry, and four-point probe measurements. Several types of samples were prepared to allow for more accurate identification of the issues and solutions are proposed to test and confirm our hypothesis.

## 6.1 SAMPLE PREPARATION

CIGS devices with a Mo/CIGS/CdS/i-ZnO/ITO structure were fabricated on SLG and alumina substrates. A bilayer Mo was deposited by DC magnetron sputtering at a constant power density of  $7.4 \text{ W/cm}^2$ . The bottom layer was deposited at Ar pressure of 1.33 Pa and a top layer at low Ar pressure of 0.4 Pa. The resulting combined thickness of the Mo film was  $\approx 800 \text{ nm}$ . For the CIGS deposition, Mo samples from the same batch were used. Half of the Mo samples were immersed into the deionized water ( $18.2 \text{ M}\Omega$ ) at  $50^\circ\text{C}$  for twenty-four hours in a glass beaker prior to CIGS deposition (referred to as water-soaked (WS) samples), while the other half was kept in a desiccator. The CIGS layers were thereafter deposited by using a three-stage co-evaporation process [165] as reported in reference [36]. The cells were completed by depositing CdS (50-60 nm) using chemical bath deposition, i-ZnO (70-80

nm) and ITO(250-300 nm), both using RF sputtering with a constant power density of  $4.93 \text{ W/cm}^2$  at the Ar pressure of 5 mT. Finally, the Ni/Al front contacts were deposited by e-beam evaporation. Table 9 summarizes the type of CIGS samples studied in this work. Sample A prepared on SLG substrate and Sample D prepared on alumina substrate are the reference samples in the experiment, allowing comparison with the water exposed samples.

TABLE 9: Summary of the CIGS samples used in this study.

Sample	Substrate	Mo WS	NaF PDT
A	SLG	No	No
B	SLG	Yes	No
C	SLG	Yes	Yes
D	Alumina	No	Yes
E	Alumina	Yes	Yes

The structural analysis of the films was done by X-ray diffraction (XRD) (Mini-flex benchtop X-ray diffractometer, Rigaku) and the optical properties were extracted using spectroscopic ellipsometry (M2000, J.A. Woolam Co.). Surface topography was analyzed by atomic force microscopy (AFM), and the cross-section morphology was studied by scanning transmission electron microscopy (STEM). Samples for STEM work were prepared in a FEI Helios Ga-source focused ion beam (FIB) at 30 kV using low currents (48 pA - 96 pA) and finished with a 5 kV cleanup to minimize amorphous damage. STEM imaging was performed on an image-corrected FEI Titan3 G2 STEM at 300 kV. Secondary ion mass spectrometry (ToF SIMS) was used to measure the compositional variation as a function of depth in the device. ToF-SIMS analyses were conducted using a TOF SIMS V (ION TOF, Inc. Chestnut Ridge, NY) instrument. 3 KeV Cs<sup>+</sup> with 20nA current was used to create a 120 $\mu\text{m}$  by 120 $\mu\text{m}$ , and middle 50 $\mu\text{m}$  by 50 $\mu\text{m}$  areas was analyzed using 0.3pA Bi<sup>3+</sup> primary ion beam. The photovoltaic characteristics were evaluated by in-house current density-voltage (J-V) measurements under AM1.5G with a light intensity of 100 mW/cm<sup>2</sup> at 25°C (IV5, PV measurement, Inc.) and by external quantum efficiency (QE) measurements (QEX7, PV measurement, Inc.).

## 6.2 CHARACTERIZATION OF Mo THIN FILM ON SLG SUBSTRATE

The XRD diffractograms of the reference Mo and water-soaked Mo is shown in Figure 44. The anticipated peaks relating to Mo-O phases were not evident in the symmetric geometry ( $\theta/2\theta$ ) XRD patterns at least in the water-soaked Mo. Furthermore, no noticeable change in the peak position, intensity or broadening was observed in the symmetric geometry XRD ( $\theta/2\theta$ ) patterns. However, glancing incidence XRD (GIXRD) patterns of Mo before and after water soaking, taken at an asymmetric geometry with  $0.5^\circ$  angle of incidence (allowing to probe the surface region), shows a different trend. The (110), (200) and (211) peaks are observed in both films (note that the (200) peak is not readily observable in the XRD scans). The peak intensity of the (200) drastically diminished after water soaking, while the (110) and (211) intensities are only slightly reduced. It shows that the [110] is the main crystal orientation of the Mo films. The AFM images show a granular nanocrystalline surface morphology (Figure 45). The water-soaked Mo shows a modified grain structure and a slight increase in the rms surface roughness (from 3.98 nm to 4.23 nm).

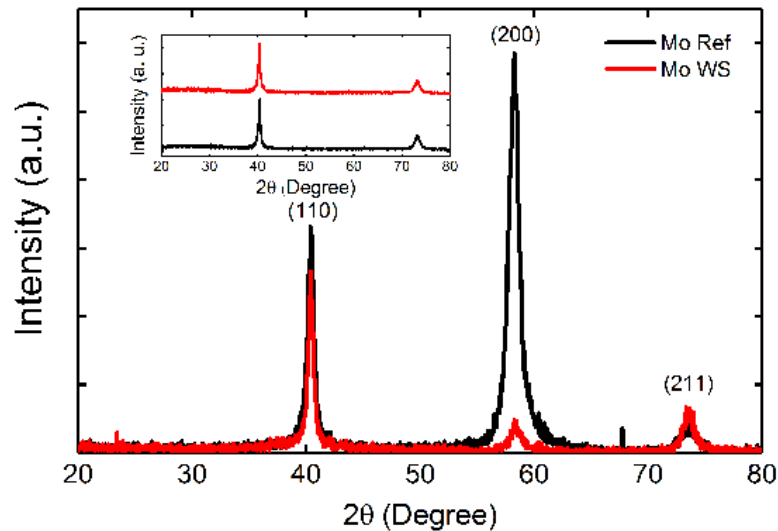


FIG. 44: The GIXRD pattern of the reference Mo film and the water-soaked Mo film (insert: XRD measurements).

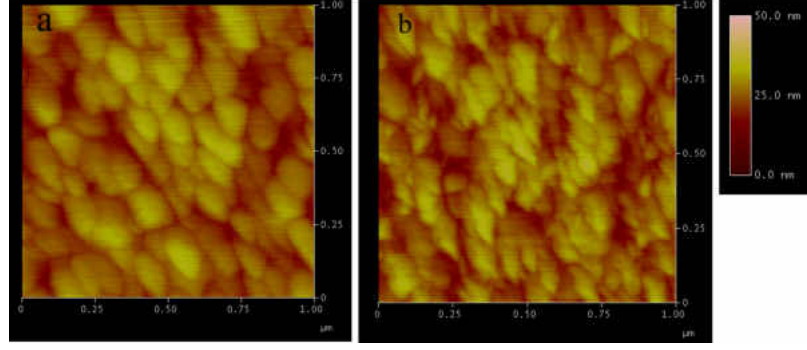


FIG. 45: AFM images for the reference Mo (a) and water-soaked Mo (b).

The film structure and the electrical properties of the Mo film were optically analyzed by spectroscopic ellipsometry (SE) measurement before and after water soaking the Mo layer. Figure 46 shows the nominal structural model used in the analysis of the SE data. The dielectric functions of the surface roughness layer were determined using the Bruggeman effective medium approximation(EMA) [126] by assuming a mixture of bulk layer material and the void with 50-50% (Mo-voids). The complex dielectric functions( $\epsilon$ ) of the Mo layers were obtained by mathematical inversion [120]. The parametric form of the extracted dielectric functions using a Drude oscillator( $\epsilon_{Drude(RT)}$ )[120] and three critical point parabolic band oscillators(CPPB)[120] expressed in equation (32), was obtained by least square regression analysis.

$$\epsilon(E) = \epsilon_{1,\infty} + \epsilon_{Drude(RT)} + \sum_{n=1}^3 \epsilon_{CPPB,n}(E) \quad (32)$$

where,  $\epsilon_{1,\infty}$  is an energy-independent contribution to the real part of the dielectric function.



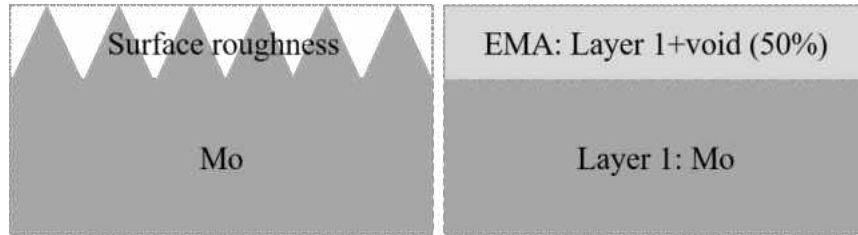


FIG. 46: Model used to study the dielectric properties of the Mo film in the spectroscopic ellipsometry analysis. The surface roughness layer was modeled using the Bruggeman EMA with 50-50% Mo-voids.

Figure 47 shows the dielectric functions of the reference Mo and the water-soaked Mo. A rapid decrease in the  $\epsilon_1$  spectra below the photon energy of 1.5eV, represents the dielectric response due to the free-carrier absorption relating to the Drude term. The resistivity and the scattering time deduced from the Drude term suggest that the resistivity increased by  $\approx 2\times$  and scattering time decreased by  $\approx 2\times$  after water soaking. The increase in resistivity as observed with ellipsometry correlated well with the measured resistivity from four-point probe measurements. The relatively shorter scattering time in the water exposed Mo may result from the increased grain boundary scattering in the water exposed Mo[165]. It was also observed that the amplitude of  $\epsilon_2$  for the reference Mo was higher compared to the water-soaked Mo which occurs due to the stronger optical absorption associated with the interband transitions [165]. This, in turn, suggests a higher void volume fraction or the decrease in the crystallite packing density of the water-soaked Mo compared to the reference Mo [165, 166]. It is worth noting here that the surface roughness layer from this analysis was found to increase from  $6 \pm 2$  nm to  $14 \pm 3$  nm after water soaking. The apparent increase in porosity or decrease in density of the Mo film after water exposure from this optical analysis was further validated by high-angle annular dark field (HAADF) STEM analysis discussed in the next section. Additionally, the reflectance of the Mo sample before and after water exposure as measured by spectroscopic ellipsometry (SE) is shown in Figure (48). The reflectance of the Mo samples dropped by  $\approx 50\%$  in average after water soaking in the measured wavelength range from 300 nm to 1000 nm.

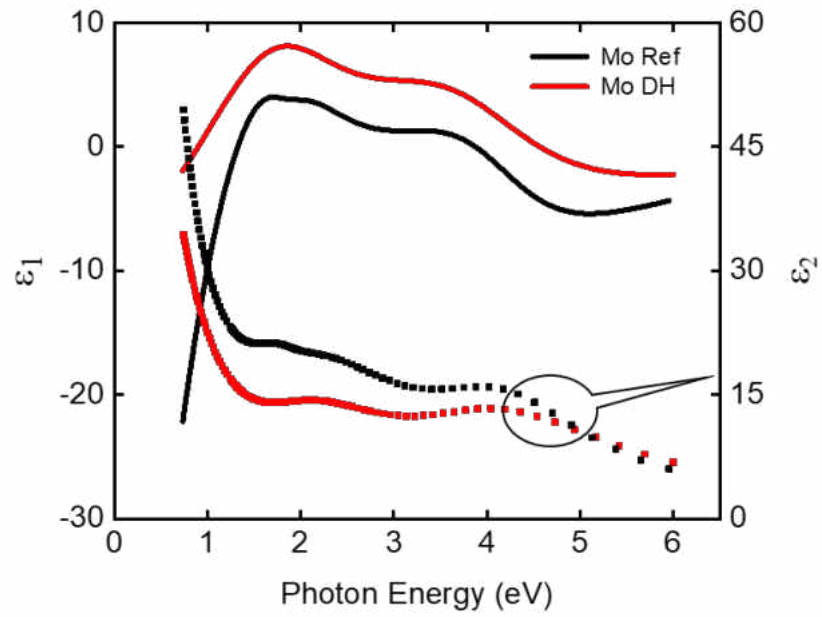


FIG. 47: Dielectric function  $\epsilon = \epsilon_1 + i\epsilon_2$  of the reference and the water-soaked Mo film.

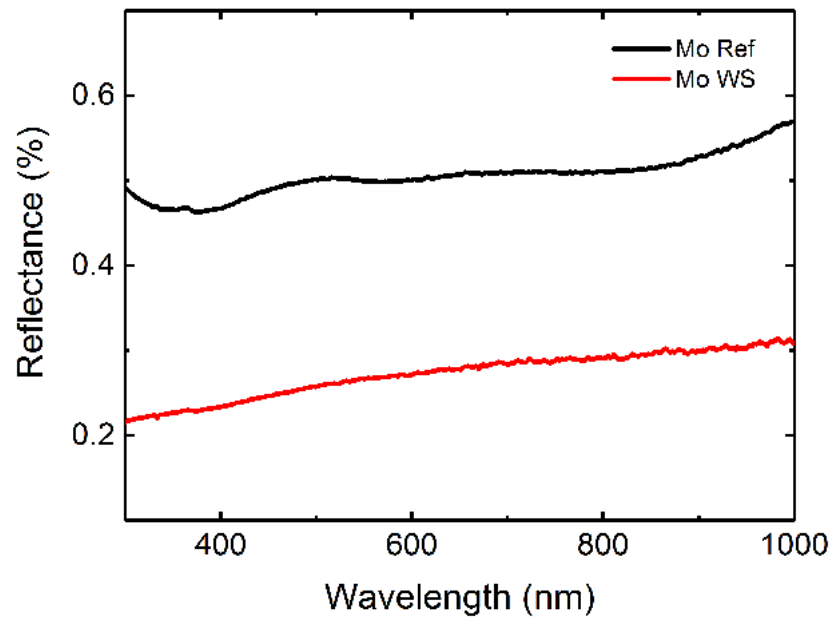


FIG. 48: Reflectance of the reference and the water-soaked Mo film.

### 6.3 EFFECTS OF Mo DEGRADATION IN CIGS FILM

Figure 49 shows the XRD diffractogram of the various CIGS samples studied in this chapter. While the samples prepared on SLG substrates show intense (220)/(204) CIGS peaks, samples prepared on alumina have a relatively intense (112) CIGS peak orientation (peak assigned according to ICDD card 00-040-1488). For both substrates, the intensity of the (112) peak is higher on Mo WS. No change was observed in the XRD pattern between samples B and C. The degree of preferred orientation along the (hkl) direction, was calculated using equation (33)[91],

$$p(hkl) = \left[ \frac{I(hkl)}{I_o(hkl)} \right] \cdot \left[ \sum \frac{I(hkl)}{I_o(hkl)} \right]^{-1} \quad (33)$$

where,  $I(hkl)$  is the relative peak intensity of a given orientation, and  $I_o(hkl)$  is the relative intensity of the same peak from the ICDD reference card (00-040-1488 for CIGS). The degree of preferred orientation and the FWHM are listed in Table 10. Overall, an increase in the (112) orientation and a decrease in the FWHM was observed for CIGS film on Mo WS.

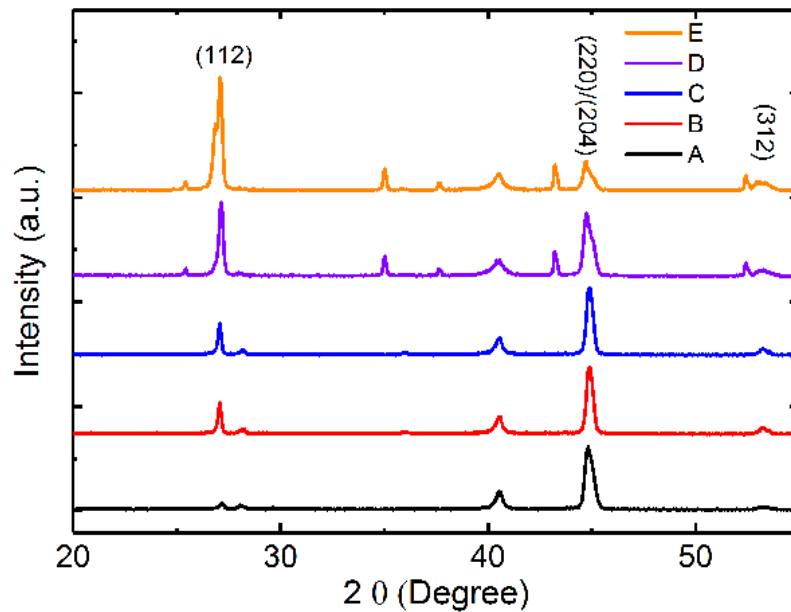


FIG. 49: The XRD pattern of the CIGS samples as listed in Table 9

TABLE 10: Calculated CIGS film texture from XRD measurement

Samples	p(112)	p(220)/(204)	FWHM[°](112)	FWHM[°](220)/(204)
A	0.064	0.86	0.201	0.439
B	0.229	0.76	0.162	0.439
C	0.229	0.76	0.162	0.325
D	0.353	0.431	0.207	0.390
E	100	0.329	0.199	0.250

Figure 50 shows the HAADF STEM images of CIGS devices prepared on SLG/Mo substrates. The cross-sectional images reveal a significant change in the morphology of the water-soaked Mo film. The reference Mo shows a bilayer columnar grains as expected since the bottom layer was deposited at high Ar pressure and the top layer was deposited at low Ar pressure with a constant sputtering power density to obtain an adhesive high conductive film. While the bottom layer of the water-soaked Mo resembled the reference Mo, the top layer was structurally degraded. This suggests a progressive degradation occurring from the top to the bottom part. Comparing the intensity in the HAADF STEM images reveals an interesting result. We note here, given the same material, the contrast in the HAADF image depends on the local density of the material. In the case of as-deposited Mo, the bottom layer appeared darker than the top layer as expected since Mo deposited at low Ar pressure is denser Mo than at high Ar pressure (other conditions remain the same). However, in the water exposed Mo, the top layer appeared darker compared to the top layer of the reference Mo and was almost similar in contrast to the bottom Mo layer, indicating the lower density of the material. This is in close agreement with the spectroscopic ellipsometry results. The apparent lower density of degraded Mo may result from the additional contribution coming from Mo oxidation since the density of  $\text{MoO}_x$  is much lower than the density of Mo. To corroborate this argument EDS analysis was performed. Indeed, EDS analysis showed a higher concentration of oxygen at the top layer, indicating oxidation of Mo (Figure 51).

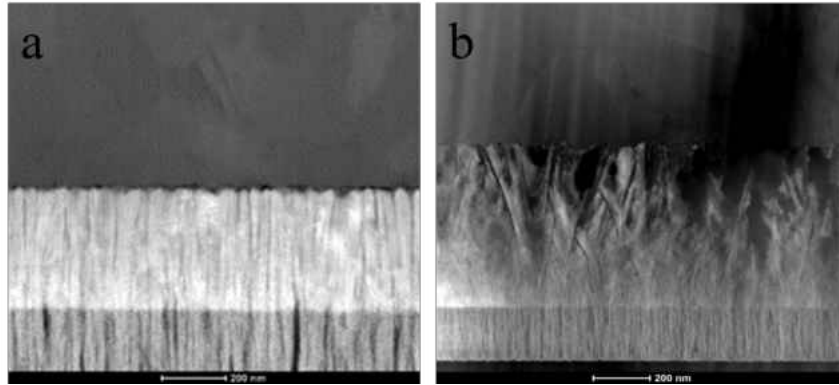


FIG. 50: STEM-HAADF image of the devices prepared on reference Mo (a) and water soaked Mo (b) on SLG substrate.

Furthermore, the areas with higher oxygen content are associated with higher Na content as well, possibly due to the formation of Na containing Mo oxides such as  $\text{Na}_x\text{MoO}_3$ [155, 167, 168] or formation of thermodynamically favorable  $\text{Na}_2\text{O}$  disrupting the Mo-O bonds[92]. Since the measurement was done on the sample after the CIGS deposition, Se was observed in the near-surface region of degraded Mo. Since there is an inverse correlation between Mo and Se content, it is likely that Se diffused rather than merely forming a  $\text{MoSe}_2$  layer, which is also supported by the observation that the  $\text{MoO}_2$  suppresses the formation of a  $\text{MoSe}_2$  layer [159]. It is possible that the selenium diffusion occurred through the micro-cracks in the oxidized Mo whose surface roughness layer, composed of underlying Mo together with the voids, was also found to be twice as rough by SE analysis.

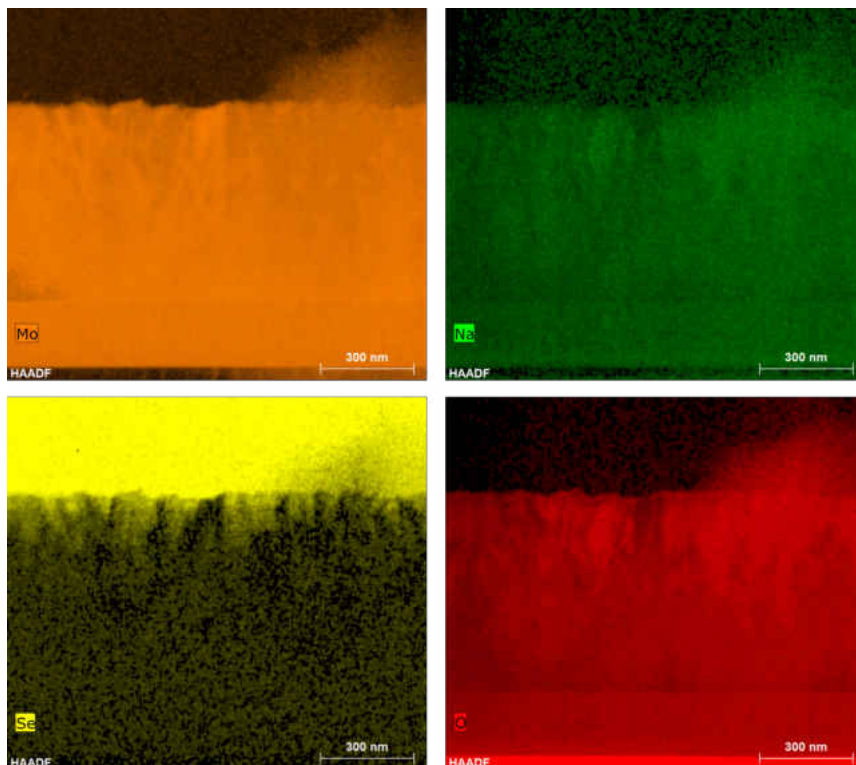


FIG. 51: The elemental distribution of Mo, O, Se and Na in oxidized Mo measured by EDS in STEM.

CIGS devices prepared on SLG substrates were analyzed by SIMS measurements (Figure 52, 53, 54, 55). Although purely quantitative analysis of the SIMS spectra could not be made due to a lack of standard, a comparative study of the elemental profiles can still be made. The  $\text{Ga}/(\text{In}+\text{Ga})$  ratio for the CIGS on reference and water-soaked Mo showed no noticeable difference. Moreover, an overall composition of the CIGS film did not show a statistically significant difference. We can, therefore, assume that the constituent elemental profile of the CIGS film and the overall composition remains identical for the control and water-soaked Mo samples, as expected.

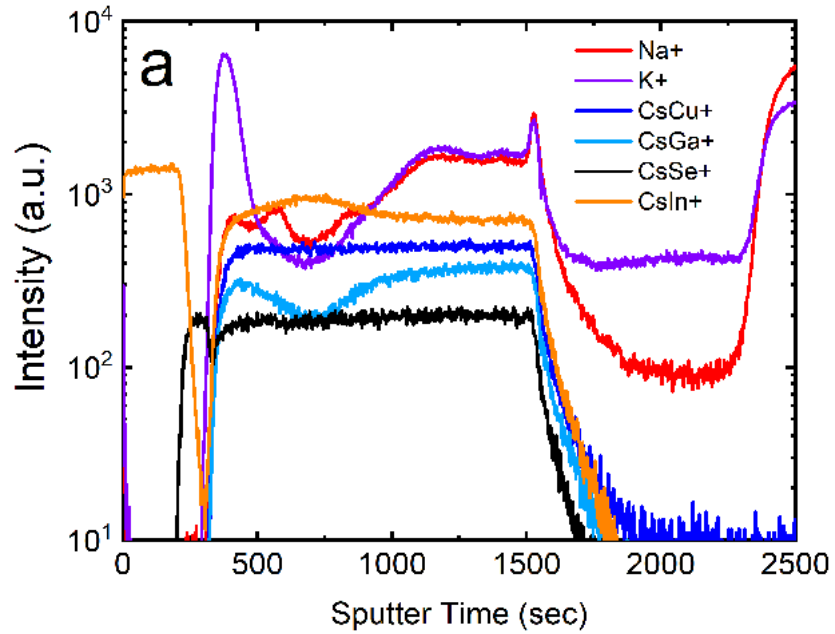


FIG. 52: Elemental distribution in the CIGS devices deposited on reference Mo ((a)-positive SIMS).

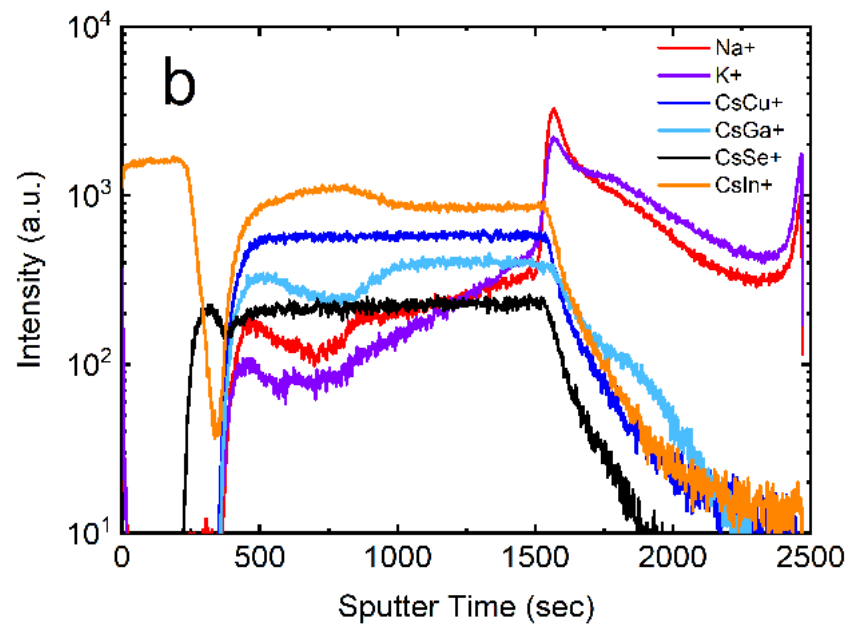


FIG. 53: Elemental distribution in the CIGS devices deposited on water-soaked Mo ((b)-positive SIMS).

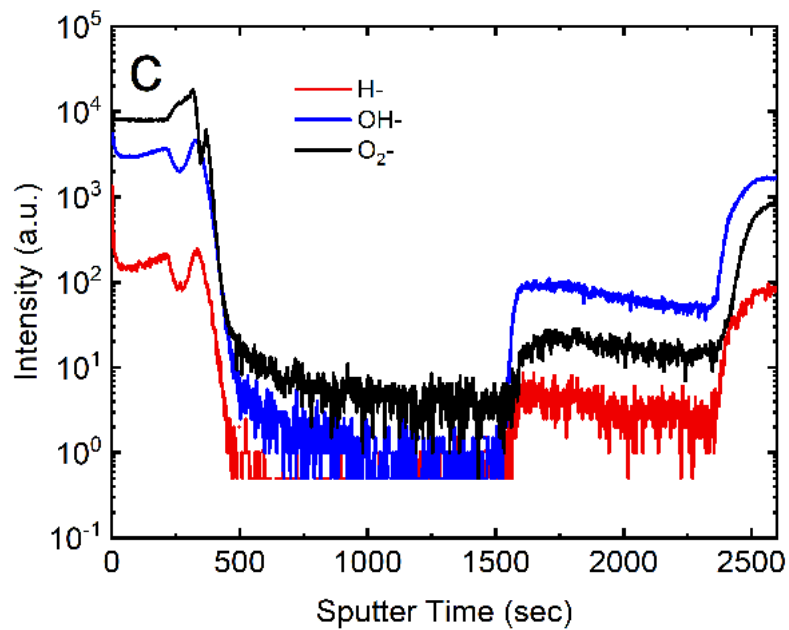


FIG. 54: Elemental distribution in the CIGS devices deposited on reference Mo ((c)-negative SIMS).

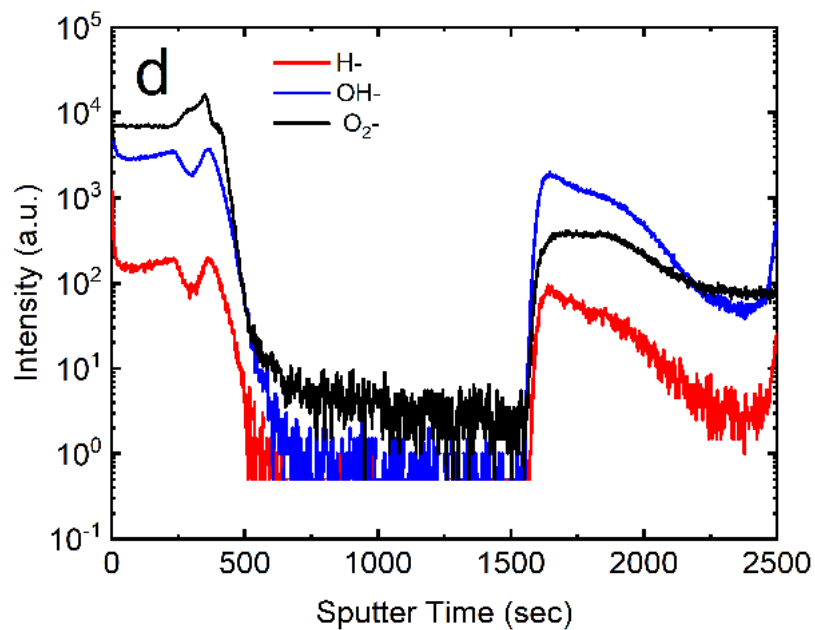


FIG. 55: Elemental distribution in the CIGS devices deposited on water-soaked Mo ((d)- negative SIMS).



Of particular interest here is the distribution of alkali elements (Na, K) in the CIGS and Mo layer (Figure 52 and Figure 53). It is well known that alkali atoms diffuse during the CIGS growth from the SLG substrate into the CIGS through the intermediate Mo layer. The properties of the Mo layer are therefore of critical importance to the diffusion of the alkali into the CIGS. Here, the alkali element profile had an upward trend within the Mo when it is water-soaked, but is flat for the reference sample inside the Mo. On the other hand, the alkali element profile has a downward slope in the CIGS when deposited on Mo WS, while it follows the Ga profile on the reference Mo. Furthermore, the bump in alkali ion at the CIGS/CdS interface observed in the reference sample is drastically reduced in the Mo WS sample. Significant differences can also be seen in the negative SIMS profile (Figure 54 and Figure 55). The  $\text{H}^-$ ,  $\text{OH}^-$  and  $\text{O}_2^-$  profiles in the reference samples are relatively flat in the Mo while being nearly absent in the CIGS. In the water-soaked Mo samples, all profiles slope upward from the glass toward the CIGS. This is in good agreement with the oxidation observed by STEM/EDS. Another trend, also observed for the alkali profiles, is the progressive disappearance of the bilayer profile in the Mo after water soaking.

Several previous studies have shown a higher diffusion of sodium in the Mo layer deposited at relatively higher Ar pressure which is also evident here in the reference Mo when we compare the Na intensity level at the bottom part deposited at high pressure to the top part deposited at low Ar pressure [155, 169]. These variations in the sodium diffusion are linked to the oxygen content, which is believed to provide a chemical driving force for Na diffusion in Mo [155, 170]. However, simultaneous Na accumulation in the oxidized Mo but frustrated diffusion into the subsequently prepared CIGS was seen in this experiment and elsewhere [167]. This suggests that the degree of oxidation in the Mo back contact plays a vital role in alkali incorporation in the CIGS films when entirely dependent on the Na supply from the SLG substrate. Based on our experimental results a possible explanation for the observed phenomena is that: (i) the oxidized Mo facilitates a higher diffusion of alkali within the Mo; (ii) the interaction of adsorbed chemical species during CIGS deposition with the heavily modified surface of Mo (as seen by GIXRD, AFM, SIMS and SE) forms a barrier to the further diffusion, where there is a significantly thicker blocking layer at the Mo/CIGS interface.

## 6.4 SOLAR CELL DEVICE RESULTS

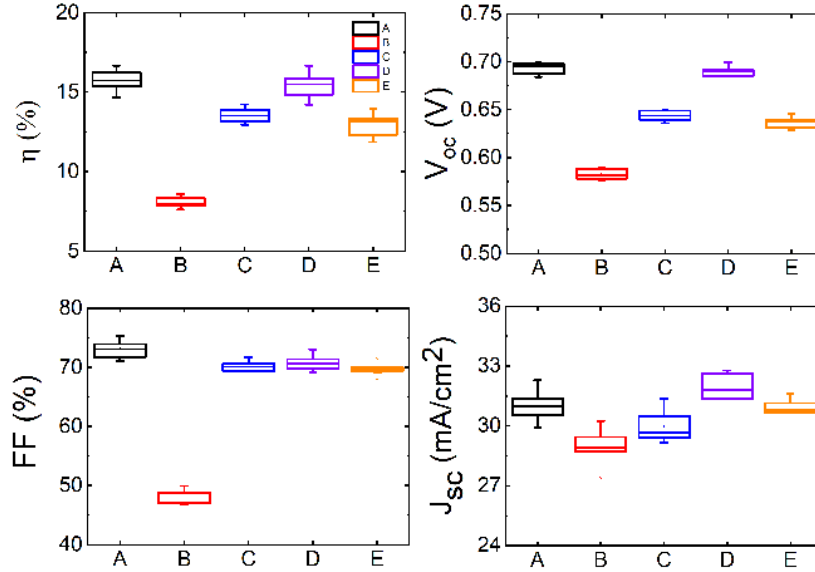


FIG. 56: Box plot of the CIGS devices in each category of the devices listed in Table 9.

The changes in alkali content in the CIGS observed in SIMS can result in significant loss in device performance [27, 122]. Solar cells were therefore fabricated according to Table 9, in an attempt to study the influence of Mo back contact on the device performance. Figure 56 shows a summary of the key photovoltaic parameters for the different types of devices and Figure 57 shows representative dark J-V curves with the double diode model fit for the same devices (labeled A to E) [171]. Compared to the reference device on SLG (Device A), the water-soaked Mo device (Device B) shows significant performance losses, due to a decrease in  $J_{sc}$ ,  $V_{oc}$ , and FF. Also, device B tends to show a slight rollover characteristic in the forward bias. A rollover effect is commonly observed in CIGS devices with low carrier concentration, mostly due to a lack of Na, [87, 172] and has been associated with a Schottky barrier at the back contact. This behavior is consistent with the SIMS analysis discussed in the previous section and confirms that Na diffusion in the CIGS layer is reduced after water soaking. In order to identify if the Mo water-soaking degrades the solar cell performance just by suppressing the Na diffusion (or if other phenomena are involved), we performed a NaF (PDT) after the growth of CIGS on a device with an

SLG/water-soaked Mo substrate (Device C). As shown by the device characteristics and the J-V curve, a partial recovery in the  $V_{oc}$ , FF, and  $J_{sc}$  was observed after the NaF(PDT). Furthermore, no rollover was observed after NaF PDT. This indicates that other factors such as degraded Mo/CIGS interface, besides Na are in play for the performance drop. To further validate that the detrimental effect is due to more than a lack of Na diffusion, CIGS devices were grown on alkali-free alumina substrates. Devices D and E were prepared in the same CIGS batch with NaF PDT, but with a Mo water-soaked substrate for Device E and a reference Mo for Device D. Device performances for Device D were comparable to the reference Device A prepared on SLG glass (Figure 56), while Device E produced degraded devices comparable to Device C (SLG/WS Mo with NaF PDT). A double diode model was then used to extract the diode parameters of all the devices (Table 11). One can see that the value of the reverse saturation current density,  $J_{o1}$ , is order/s of magnitude higher in Devices B and E as compared to their respective reference Devices A and D. The device with the most degradation is Device B, with no NaF PDT, for which all diode parameters degrade rather significantly, including in  $R_s$  and  $R_{sh}$ .

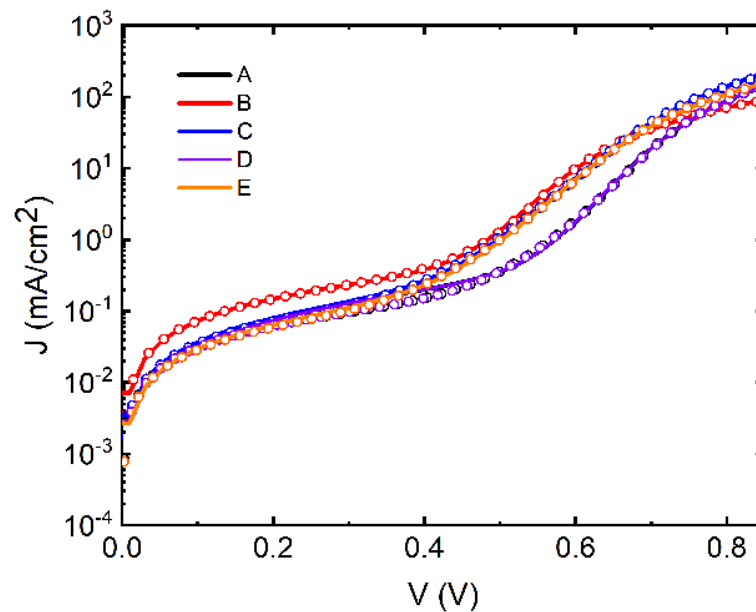


FIG. 57: Dark J-V characteristics of a representative device with double diode model fit (symbols) from each category listed in Table 9.

TABLE 11: J-V parameters of a representative solar cell device from each category listed in Table 9.

Parameter	Unit	A	B	C	D	E
$\eta$	(%)	16.5	8.6	13.6	16.0	13.9
$V_{oc}$	(mV)	697	576	657	699	646
$J_{sc}$	(mA/cm <sup>2</sup> )	31.4	29.5	29.2	31.4	30.2
FF	(%)	75.5	50.7	73.9	73.0	71.5
$J_{01}(\times 10^{-10})$	(mAcm <sup>-2</sup> )	0.25	111	0.87	0.24	1.21
$J_{02}(\times 10^{-05})$	(mAcm <sup>-2</sup> )	1.17	4.08	5.32	1.16	4.91
$R_s$	( $\Omega$ cm <sup>2</sup> )	0.73	2.34	0.66	0.93	0.96
$R_{sh}$	(k $\Omega$ cm <sup>2</sup> )	3.26	1.37	2.89	3.20	3.52

Figure 58 shows the  $QE(-1V)/QE(0V)$  ratio for devices A through E. Except for device B the ratio is close to 1, which indicates that there is no significant carrier collection loss in these samples. For device B, the ratio is wavelength dependent. The increased voltage-dependent carrier collection at longer wavelength suggest poor minority carrier collection on water-soaked Mo.

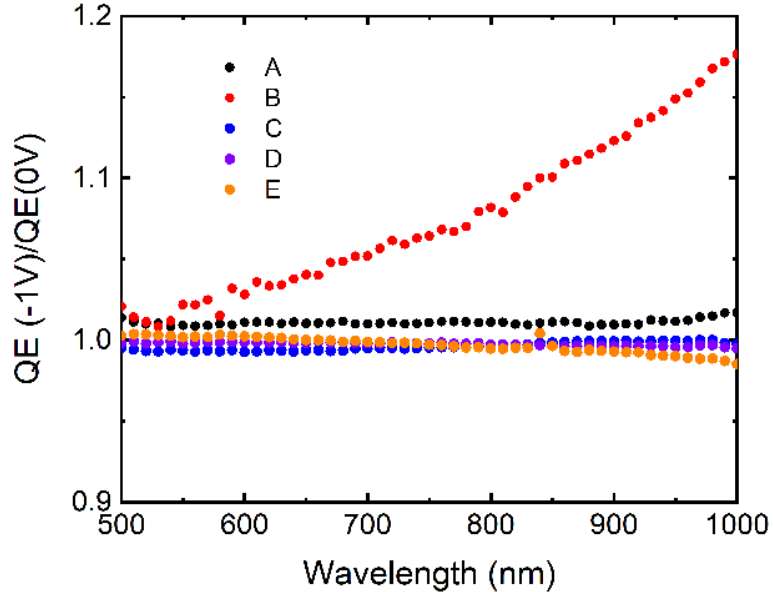


FIG. 58: The reverse bias  $QE(-1V)/QE(0V)$  characteristics of a representative device from each category listed in Table 9.

## 6.5 SUMMARY

Device efficiency and reliability can change drastically when exposed to a harsh environment. The origins of these modifications can sometimes be difficult to ascertain due to the multiple effects that can occur on the materials properties. In the case of Cu(In,Ga)Se<sub>2</sub> solar cells, the exposure of the back contact to damp heat has an immediate effect on the Mo layer right after exposure, and an even stronger effect after Cu(In,Ga)Se<sub>2</sub> deposition. In this experiment, we observed a decrease in intensity of the (200) peak in GIXRD suggesting the (200) plane is disrupted by water exposure of the Mo film. Both the AFM and SE showed surface modification through the increase in surface roughness. The oxidation caused the Mo film to be less dense suggested by SE and TEM measurement highlighting the degradation to occur due to moisture ingress. Oxidized Mo showed an increase in Na, having been annealed during the CIGS deposition which diffused through the soda lime glass substrate. However, the diffusion of Na through oxidized Mo was hindered into the CIGS as seen in the comparative SIMS profile with the reference sample. By varying the substrates and the origin of the alkali (applying NaF PDT), the distinction between the hindered alkali diffusion effect and the Mo/Cu(In,Ga)Se<sub>2</sub> interface effect were separated, demonstrated that both were present.

## CHAPTER 7

### IMPACT OF DAMP HEAT STRESS ON CIGS THIN FILM

The oxygenation of CIGS has been discussed in the context of having both beneficial and detrimental effect [173]. The passivation of the grain boundary with Se deficiencies increases the absorber effective doping level, eliminate recombination center and enhance inter-grain transport and was suggested as a beneficial effect. On the contrary, oxygenation reduced the band bending in the absorber film and enhanced the interface recombination, which is a detrimental effect. Although annealing of the complete solar cell based on  $\text{CuInSe}_2$  was an essential post-deposition step [174], no such step was required for the CIGS solar cell since the Na was employed [79]. It was argued that the oxygenation takes place in the Na containing CIGS film during air exposure of the film [173]. In reference [175], it was reported that the oxidation of bare CIGS film at elevated temperature is less detrimental than the oxidation in the humid air at room temperature in terms of electrical performance. It was mentioned that more oxidized species of Se or elemental Se, and less In and Ga oxides, were found in the CIGS containing Na (compared to without Na containing) when the samples were exposed to humid air. In the same study,  $\text{H}_2\text{O}$  catalyzed reaction was proposed for the incomplete oxidation of  $\text{Na}_2\text{Se}_x$  as well as the partial oxidation of elemental Se to support the experimental observation. In another study, the formation of a Na-O-CIGS complex was reported to be induced by  $\text{H}_2\text{O}$  [64]. The vacuum oxidation of CIGS surfaces was reported to mainly containing In or Ga oxides and  $\text{SeO}_2$  in a smaller amount, while, native oxidation also contained additional  $\text{Na}_x\text{O}$  and  $\text{Na}_2\text{CO}_3$ [65]. Pern et al. [176] reported that damp heat exposed CIGS films formed spots. These spots had relatively low gallium, copper and selenium and a higher concentration of sodium. Solar cells were completed on a bare CIGS exposed to an ambient condition and damp heat treatment. Solar cell completed on the ambient exposed bare CIGS showed severe degradation compared to the damp heat treated bare CIGS. The reduction of minority carrier lifetime was observed in the air exposed bare CIGS films, but the degradation was prevented when CdS was applied

[66, 67].

In Chapter 6, we showed that the damp heat-induced degradation of Mo back contact could have serious consequences on the layer itself and the subsequently completed CIGS solar cells. We paid close attention to the mobility of Na through degraded Mo and how it affected the solar cell devices. In this Chapter, we extended this study onto the bare CIGS thin films. As discussed above, several studies [72, 177, 180] have already reported that CIGS solar cells are sensitive to humidity ingress and that their performance degrades. However, the complete understanding of such degradation has not been uncovered. Here, we looked at the physicochemical, structural and optoelectronic properties of the bare CIGS samples before and after exposure to deionized water at 50°C for twenty-four hours, keeping the same experimental conditions that were used to study the degradation of Mo thin films in chapter 6. After such exposure, solar cells were also fabricated, and their performances were analyzed and modeled to extract valuable insight into the potential degradation mechanisms.

## 7.1 SAMPLE PREPARATION

CIGS films were deposited on Mo coated SLG glass using a three-stage co-evaporation process [116]. Parts of the CIGS samples were coated with CdS immediately after the deposition (treated here as reference samples) while some samples were immersed in deionized water for twenty four hours at 50°C before CdS deposition (water soaked (WS) samples). A combination of i-ZnO (60-100 nm)/ITO (200-250 nm) was used as a window layer for both types of samples. Finally, Ni/Al/Ni contacts were deposited by e-beam evaporation for the front contact and solar cells with an active area of 0.5 cm<sup>2</sup> were isolated by mechanical scribing.

X-ray diffraction (XRD) (Rigaku Miniflex II) was used to analyze the phases present and their preferred orientation if any. Transmission electron microscopy (TEM) was used to assess morphological changes in the layers after treatment, while energy dispersive x-ray spectroscopy (EDS) was used to measure average composition. Secondary ion mass spectrometry (SIMS) was used to measure the composition variation as a function of depth, and x-ray photoelectron spectroscopy (XPS) was used to investigate the surface composition and chemical bonding. Deep level transient/optical spectroscopy (DLTS/DLOS) was used for the quantitative characterization of deep level traps, and fast C-V was used to measure the majority carrier concentration.

Time-resolved photoluminescence measurements (TRPL) were used to obtain the minority carrier lifetime, while temperature dependent current-voltage measurements were used to identify the type of dominant recombination mechanism. The photovoltaic characteristics were evaluated by in-house current density-voltage (J-V) measurements under AM1.5G with a light intensity of  $100 \text{ mW/cm}^2$  at  $25^\circ\text{C}$  and by quantum efficiency (QE) measurements under white light bias.

## 7.2 MATERIAL CHARACTERIZATION

Figure 59 and Figure 60 show cross-sectional TEM micrographs of CIGS devices with and without water soaked CIGS absorber layer. Note that the cracks observed in both samples are presumed to have occurred sometime during the thinning process. No obvious microstructural change due to the water exposure was observed.

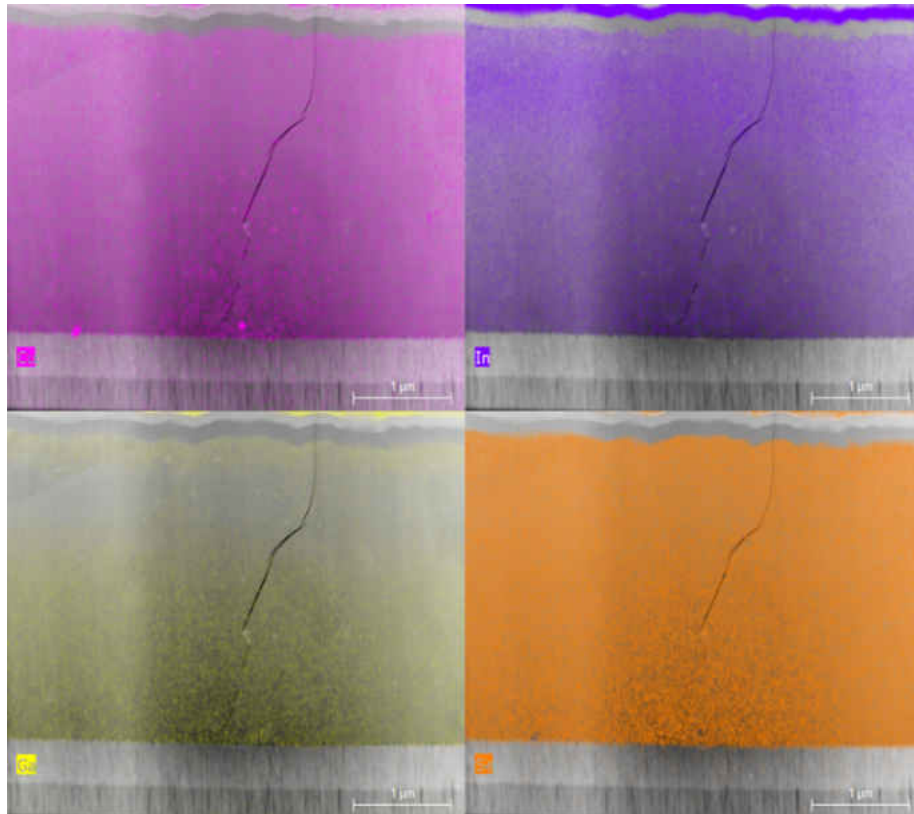


FIG. 59: STEM-HAADF cross-section image of reference CIGS device.



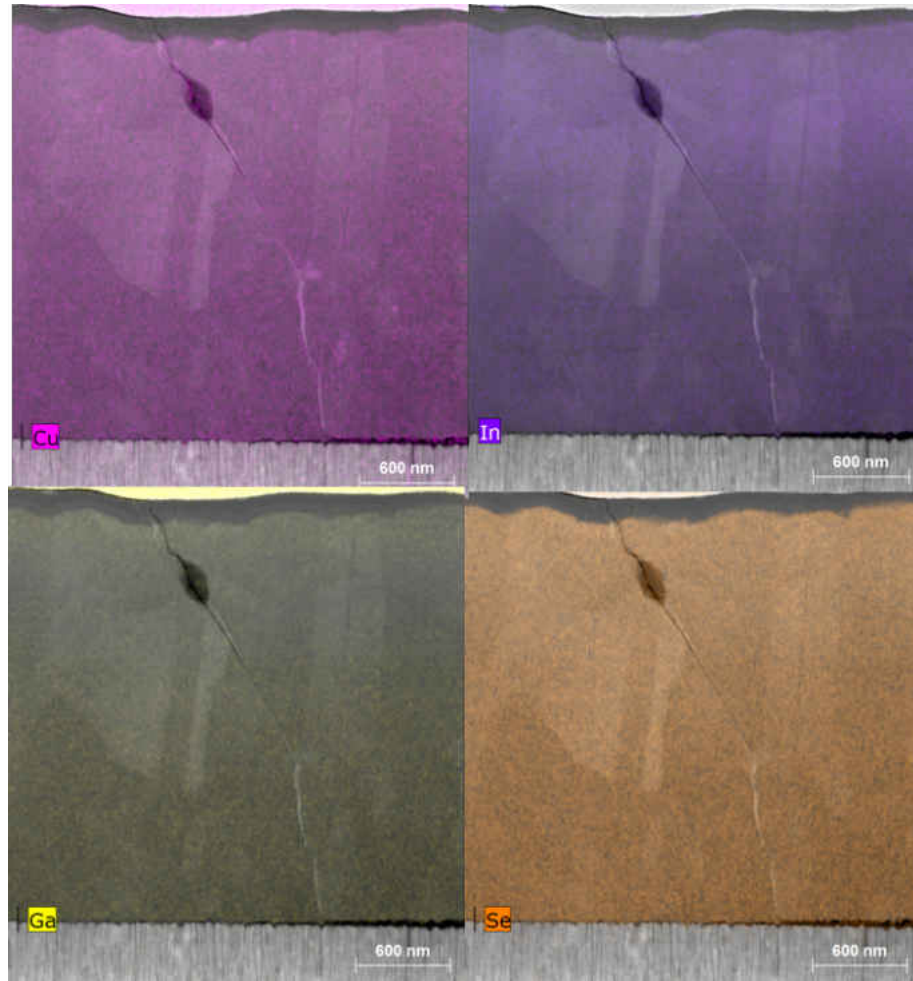


FIG. 60: STEM-HAADF cross-section image of CIGS device with water-soaked CIGS layer.

The surface composition and chemical states of the elements were measured by XPS (Figure 61,62,63,64,65,66). The Cu, In and Ga peaks showed a slightly higher intensity after WS, while the Se3d peak shows a higher intensity. The Se3d spectrum for the reference sample also shows a Na2s peak at 63.0 eV and a peak at 58.8 eV assigned to  $\text{SeO}_2$ [65]. The oxidation of Se could form the water-soluble selenium dioxide when exposed to air[181]. It is interesting to note that both the Na2s and  $\text{SeO}_2$  peaks disappeared in the WS sample. One can also notice a decrease in the peak intensity for the O1s and Na1s peaks. Along with the disappearance of the  $\text{SeO}_2$  peak, this indicates the removal of water-soluble compounds from the surface layer, which correlates well the increase in the intensity of the CIGS constituent peaks.

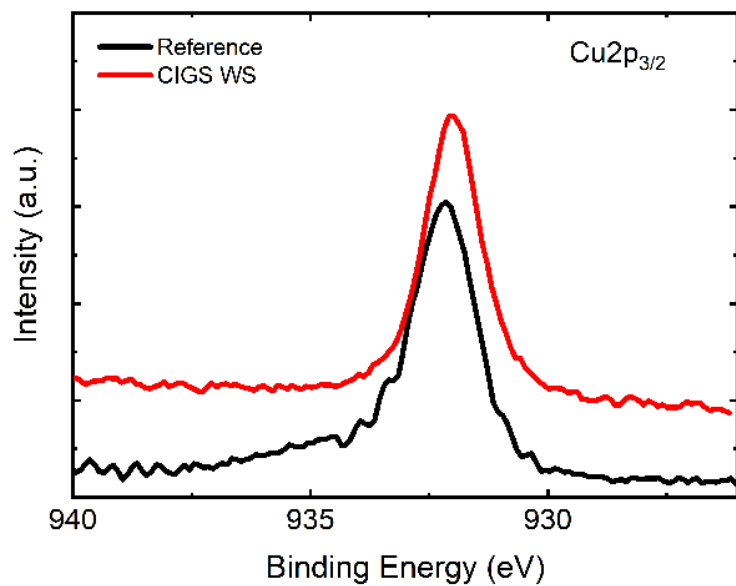


FIG. 61: Comparative XPS peak of Cu 2P<sub>3/2</sub> between reference (black) and water soaked (red) CIGS thin film.

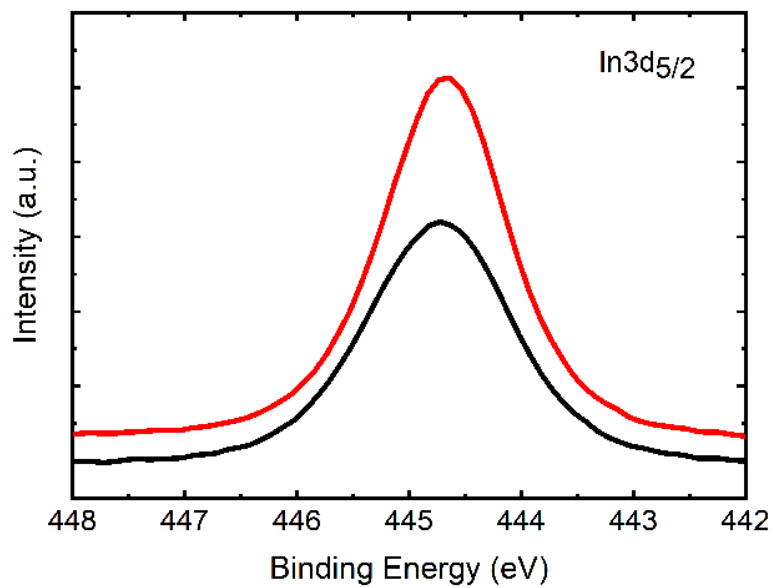


FIG. 62: Comparative XPS peak of In 3d<sub>5/2</sub> between reference (black) and water soaked (red) CIGS thin film.

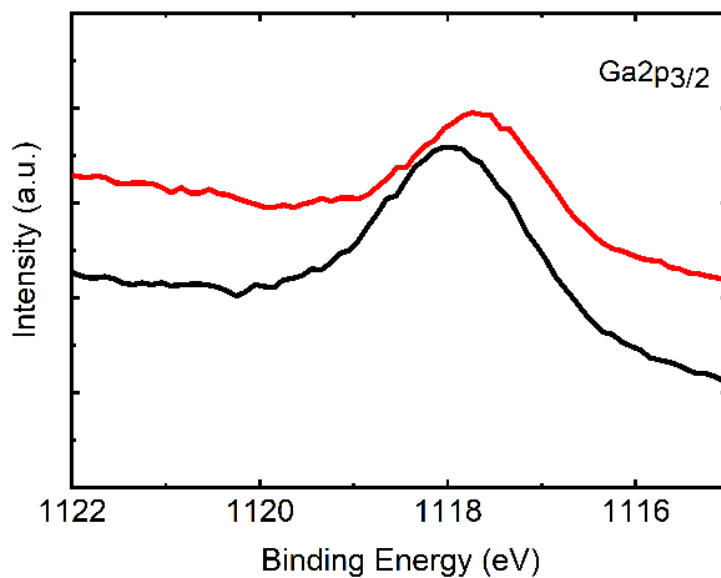


FIG. 63: Comparative XPS peak of Ga 2P<sub>3/2</sub> between reference (black) and water soaked (red) CIGS thin film.

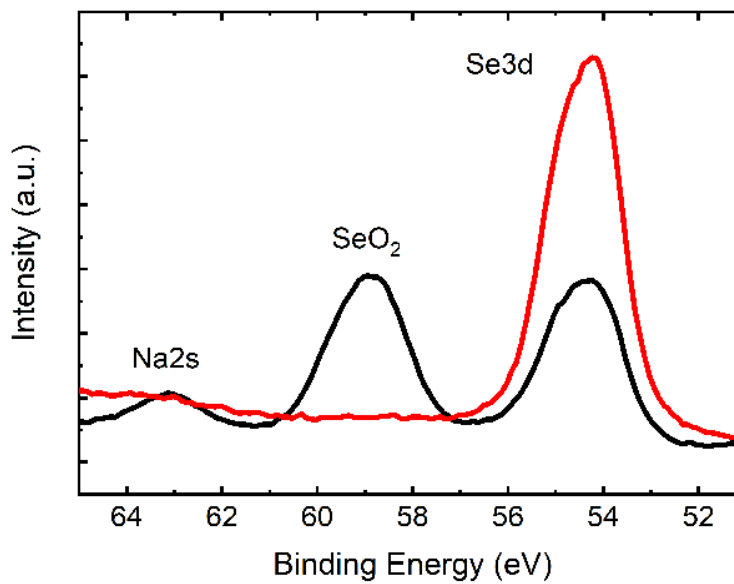


FIG. 64: Comparative XPS peak of Se 3d between reference (black) and water soaked (red) CIGS thin film.

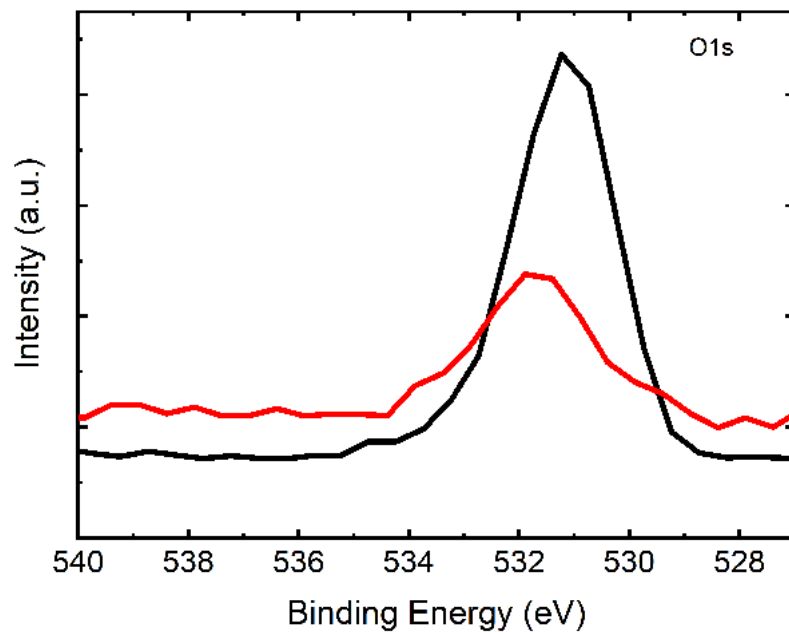


FIG. 65: Comparative XPS peak of O 1s between reference (black) and water soaked (red) CIGS thin film.

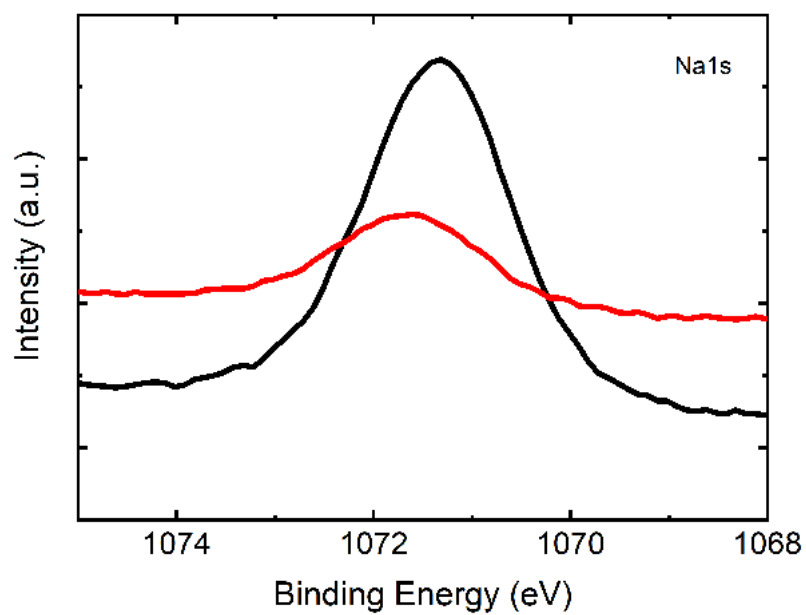


FIG. 66: Comparative XPS peak of Na 1s between reference (black) and water soaked (red) CIGS thin film.

The elemental depth profile of the studied samples from the SIMS measurement is shown in Figure 67 and Figure 68. The  $\text{CsCu}^+$  profile whose intensity in both the reference and water-soaked film remained approximately the same throughout the CIGS film thickness is used as a reference signal for comparing the relative change in the alkali metal distribution in each film. Both the  $\text{Na}^+$  and  $\text{K}^+$  signal was observed lower in the water-soaked sample compared to the reference sample throughout the CIGS film. No noticeable difference was observed in the gallium and indium profile in the SIMS data. The accumulation of both  $\text{Na}^+$  and  $\text{K}^+$  at back interface (Mo/CIGS) was observed in both sets of samples; however, their intensities decreased in the water-soaked sample. Similarly, a clear reduction in the  $\text{Na}^+$  and  $\text{K}^+$  signal was also observed at the front interface (CIGS/CdS) in the water-soaked sample compared to the reference sample. The relatively higher reduction of  $\text{Na}^+$  signal than the  $\text{K}^+$  signal indicates a faster migration of  $\text{Na}^+$  than  $\text{K}^+$  at elevated temperature in the CIGS bulk which may occur due to smaller ionic radii of  $\text{Na}^+$  compared to  $\text{K}^+$  [43]. The pronounced depletion of alkali at the water exposed surface suggests that both  $\text{Na}^+$  and  $\text{K}^+$  diffuse out from bulk to the front surface and potentially dissolve in the water.

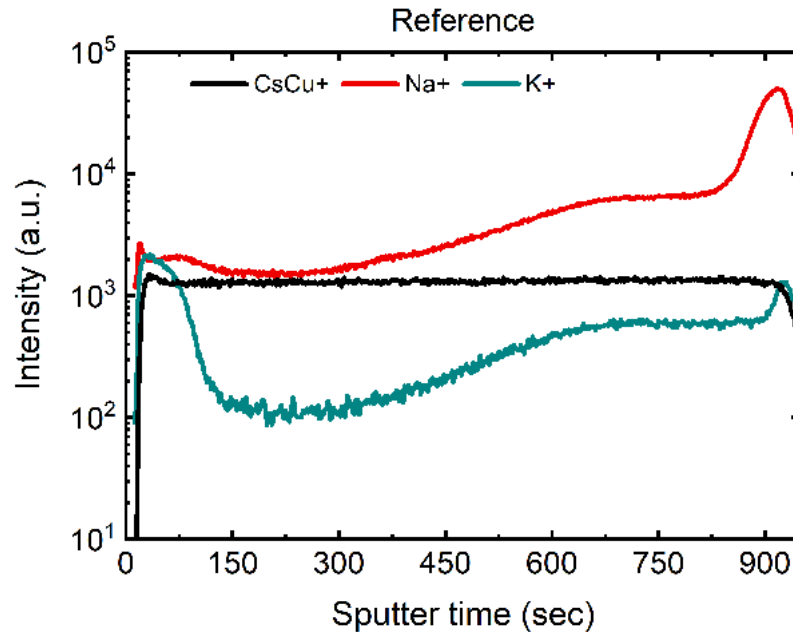


FIG. 67: SIMS depth profile of  $\text{Na}^+$ ,  $\text{K}^+$  and  $\text{CsCu}^+$  in reference CIGS layer.

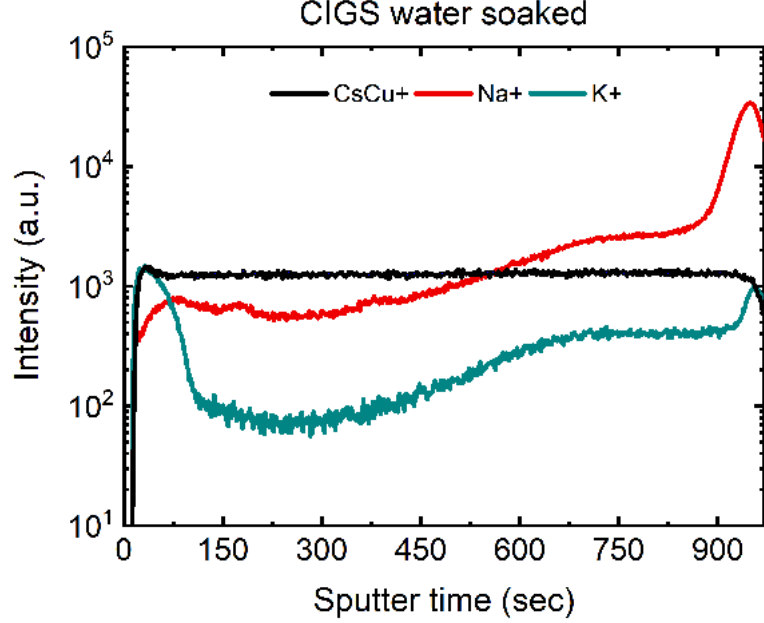


FIG. 68: SIMS depth profile of  $\text{Na}^+$ ,  $\text{K}^+$  and  $\text{CsCu}^+$  in the water soaked CIGS layer.

It is well known that the incorporation of an alkaline element results in enhanced p-type conductivity [36, 87, 122]. The loss of alkaline element in the water-soaked sample as shown by XPS and SIMS is expected to reduce net doping concentration in these samples compared to the reference which was confirmed by performing a fast C-V measurement [144]. To eliminate the artifact caused by trapping effect, fast CV measurements were performed from 0V to -1V DC applied bias with 2000V/s sweep rate. The doping profile from the fast C-V measurement shows the doping concentrations of the reference and water exposed devices are  $4.0 \times 10^{16} \text{ cm}^{-3}$  and  $2.5 \times 10^{16} \text{ cm}^{-3}$ , respectively. This indicates water soaking leads to large compensation, which could contribute to the degradation of solar cell performance and is likely due to deep level trap formation.

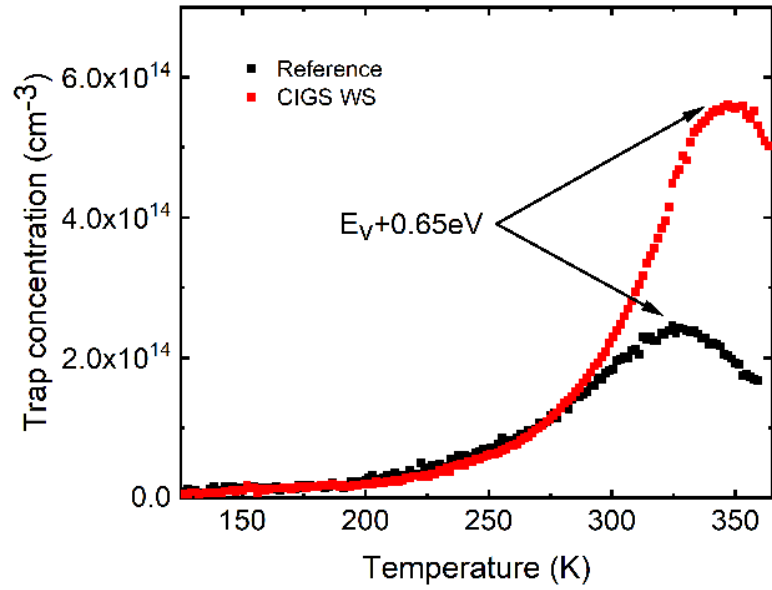


FIG. 69: DLTS spectra comparison of CIGS water soaked solar cell and reference solar cell from 100K to 365K. The concentration of  $E_v+0.65$  eV trap is  $\approx 2.5$  times higher in CIGS water soaked solar cell [184].

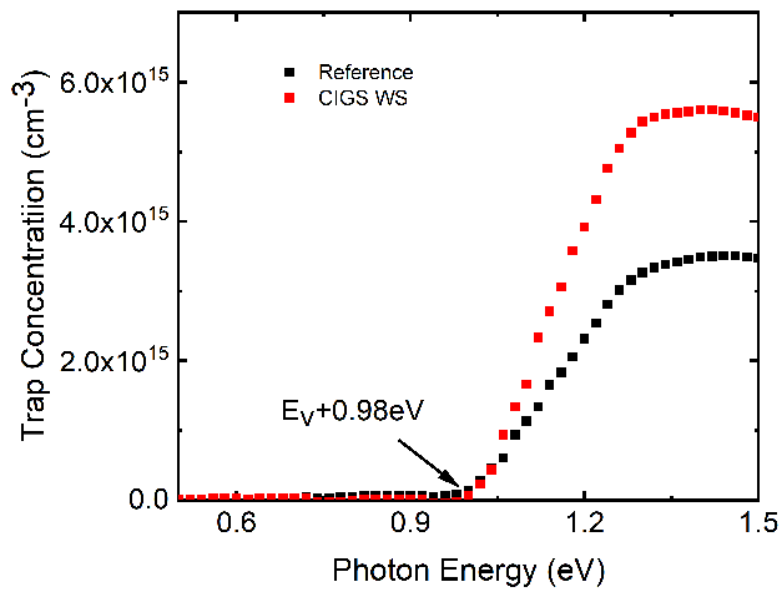


FIG. 70: Comparison of the DLOS spectra of the reference cell and WS CIGS solar cell [184].

To study the effect of water soaking of CIGS film in the deep level trap spectrum and their potential contribution to degradation of solar cell performance, trap spectroscopy measurements were performed. To probe the trap located in the lower half of the bandgap DLTS measurements were performed. Figure 69 shows the DLTS spectra for both the samples where both samples show one positive peak with the activation energy of  $E_v+0.65(\pm 0.02)$  eV and the capture cross section of  $6.0 \times 10^{-17}$  cm<sup>2</sup>. The concentrations of the  $E_v+0.65$  eV trap was  $\approx 2.5 \times$  higher in the water-soaked CIGS sample [77]. To probe the defects located in the upper half of the bandgap, DLOS measurements were performed. Figure 70 shows the DLOS spectra of both samples where an onset at 0.98 eV is visible in both samples, which is indicative of the  $E_v+0.98$  eV trap. The concentrations of  $E_v+0.98$  eV trap was about  $\approx 60\%$  higher in the water-soaked CIGS sample compared to reference sample [77]. The  $E_v+0.98$  eV trap has been previously identified in CIGS solar cell and the sensitivity of this trap to alkali metal content has been previously reported in chapters 4 and 5.

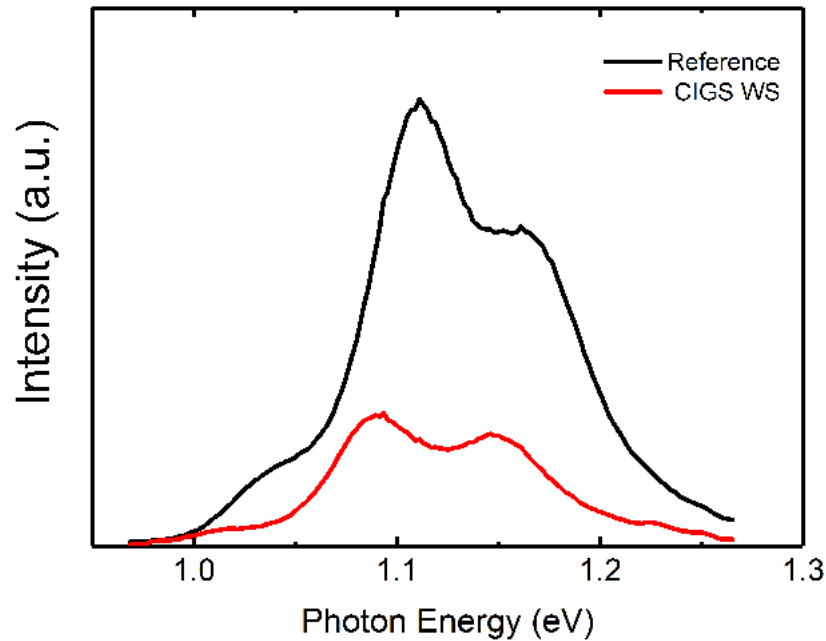


FIG. 71: PL spectrum of CIGS/CdS junction of the reference and the water soaked CIGS.



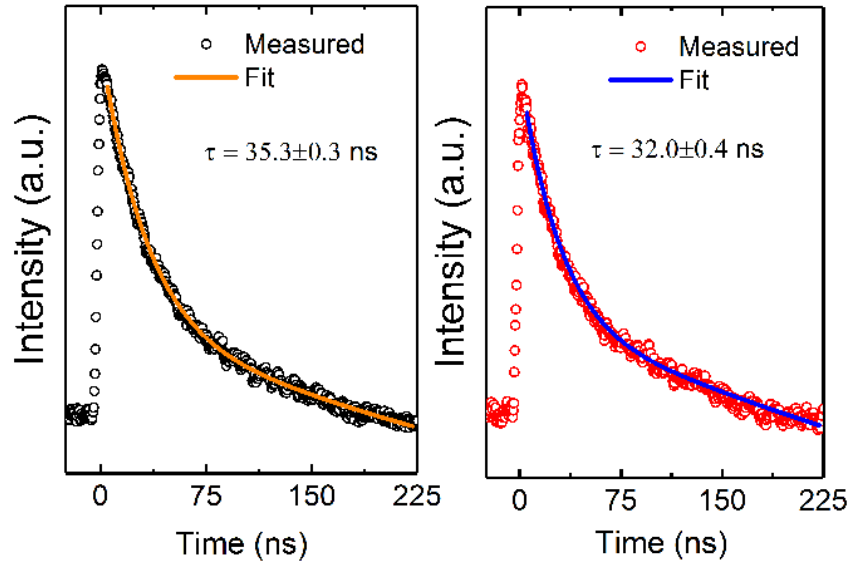


FIG. 72: TRPL dynamics of the reference (left) and the water soaked CIGS(right).

Figure 71 shows the PL spectrum of the reference and the water-soaked sample. The PL peak position shows a minor shift between two samples indicative of some compositional variation between two samples although they came from the same deposition run. The peak obtained at  $\approx 1.16$  eV for reference sample and  $\approx 1.15$  eV for water-soaked CIGS sample align closely with the nominal bandgap obtained from the quantum efficiency measurement suggesting near band edge emission due to band to band recombination. PL peak at  $\approx 1.11$  eV and  $\approx 1.09$  eV for reference and water exposed CIGS respectively are considered to be originating from a donor-acceptor pair transition [182]. The lower PL yield in the water exposed sample is indicative of higher surface recombination rate [183]. Furthermore, the PL decay curve is shown in Figure 72. The minority carrier lifetime showed slight decrease in water exposed sample, from 35 ns to 32 ns. The substantial changing in the PL quantum yield and initial PL amplitude while keeping the life time almost same most likely indicates a presence of static, not dynamic quenching where the party responsible for quenching forms in the ground state, takes some emitters off their emissive states while the unaffected emitters keep their emission life time [184].

### 7.3 SOLAR CELL DEVICE RESULTS

Solar cell devices were completed with reference CIGS films as well as WS CIGS films to evaluate the impact of moisture and heat on the device parameters (Figure 73). An overall loss in power conversion efficiency was observed due mostly to a decrease in open circuit voltage ( $V_{OC}$ ) and fill factor (FF), as well as a small decrease in short circuit current density ( $J_{SC}$ ). Analysis of the individual curves shows that there is a systematic increase in the series resistance (from 0.8 to 1.2  $\text{ohm.cm}^2$ ), shunt conductance (from 0.5 to 0.8  $\text{mS.cm}^{-2}$ ) and diode quality factor (from 1.6 to 1.8) after moisture and heat treatment. To better understand the origins of the device performance deterioration after WS treatment, temperature dependent J-V curves were measured (Figure 74). One can see that there is no roll over even at low temperature for the WS sample, indicating no significant deterioration of the back contact shown in the insert. Next, the open circuit voltage was extracted and plotted as a function of temperature to identify potential recombination mechanism. The results suggest that Shockley Read Hall recombination in the bulk is dominating over the interface recombination as the open circuit voltage at 0K extrapolates to the bandgap in both cases.

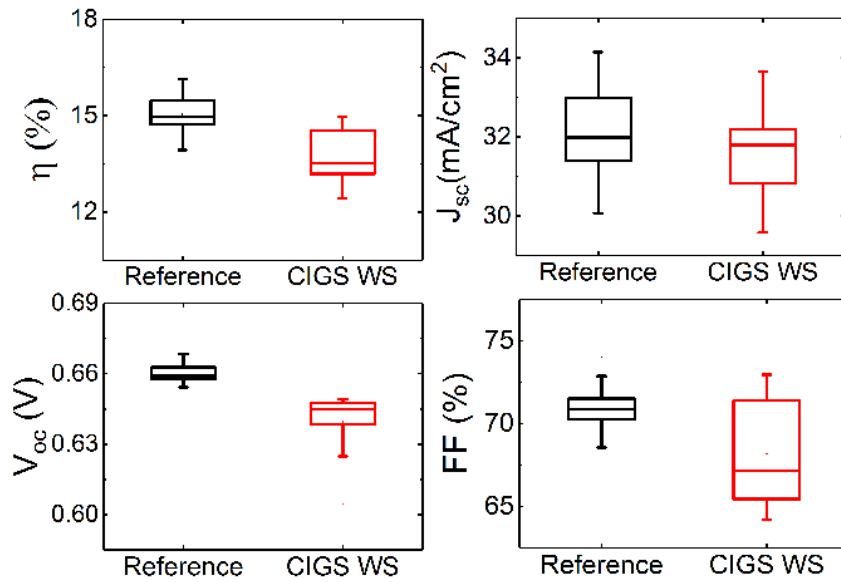


FIG. 73: Comparison of the device characteristics of the water-soaked CIGS film with the reference device.

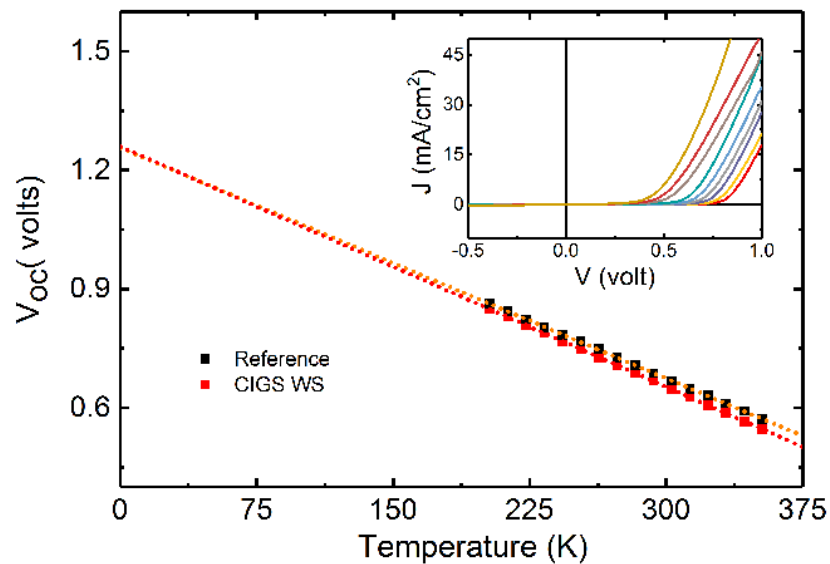


FIG. 74: Temperature dependence of the open circuit voltage for the WS sample and the reference sample (Insert: Dark current-voltage curve for a water-soaked sample measured in the temperature range  $-70^{\circ}\text{C}$  to  $80^{\circ}\text{C}$ ).

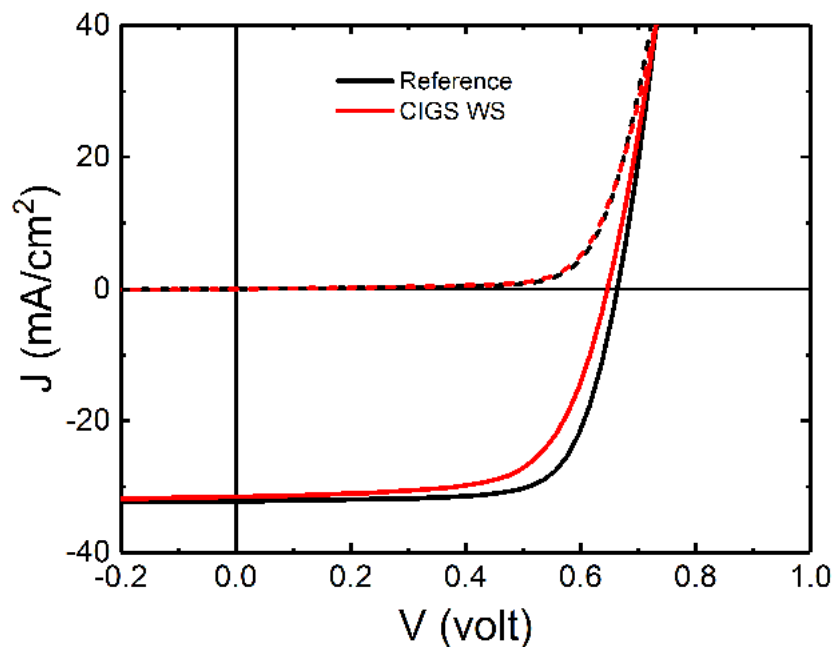


FIG. 75: Representative current density versus voltage curve of the reference and water-soaked CIGS solar cell device.

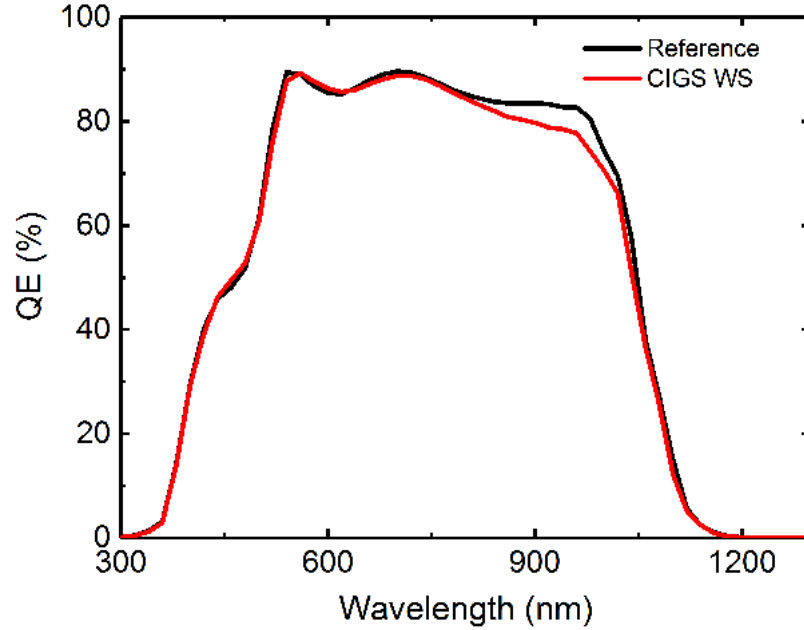


FIG. 76: Representative external quantum efficiency curves for the reference and water-soaked CIGS solar cell.

Looking first at the change in open circuit voltage, the expected decrease in  $V_{oc}$  value of  $\approx 12$  mV due solely to the decrease in hole concentration is lower than the experimentally measured  $V_{oc}$  decrease of  $\approx 20$  mV. Therefore, the decrease in hole concentration does not entirely explain the  $V_{oc}$  deterioration in the WS treated devices. The relatively high density of  $E_v+0.98$  eV trap center in water exposed sample, which was previously shown to act as a compensating center is a potential source for the reduction in the p-type conductivity[77]. Additionally, the higher concentration of  $E_v+0.65$  eV mid-bandgap trap in water exposed sample could contribute to the reduced minority carrier lifetime which in turn reduces the  $V_{oc}$  and  $J_{sc}$ . Next, the change in fill factor was identified as being due mostly to the change in series resistance and shunt conductance, but also to the voltage dependent current collection. After moisture and heat treatment, the decrease in the alkali leads effectively to a decrease in the majority carrier concentration (as seen by C-V measurements), which causes increase in recombination at the back of the cell, without leading to a roll-over (as seen in Figure 74).

## 7.4 SUMMARY

In case of CIGS water exposure, no structural or composition changes were observed, but the alkali distribution as well as the surface were altered. Different alkali metals behaved differently, as sodium diffused faster than potassium out of the layer. This redistribution of alkali metals had a profound effect on the electrical properties of the materials, with a decrease in majority carrier concentration and minority carrier lifetime, and an increase in trap densities. This, in turn, impacted the device parameters with a notable decrease in  $V_{oc}$  and FF, but did not modify the main recombination mechanism (SCR in the bulk) or create a back diode. Simulations indicate that most of the changes in  $V_{oc}$  can be attributed to the change in  $N_A$  (and therefore Na), while the changes in FF are due to the increase in  $R_S$  and decrease in  $R_{sh}$ . Finally, the slight decrease in  $J_{sc}$  was associated with a  $N_A$  gradient, whereby its value decreased below a threshold after water soaking leading to recombination at the back of the cell. Interestingly, even though we also observed modification of the surface, this did not seem to be a major factor to fit the device parameters. Once again, as is often the case with CIGS, it seems that its device properties after water soaking are controlled by its alkali profile. One could, therefore, think that it could be possible to address such deterioration by (i) assessing whether water exposure had an effect (most easily done by measuring  $N_A$ , directly or indirectly) and, if this is the case, by (ii) compensating for it by alkali post-exposure treatment.

## CHAPTER 8

### CONCLUSIONS

This thesis investigates the effects of selected alkali metals incorporated in a CIGS solar cell device on their efficiency and reliability. With the demonstration of higher than 22% efficient CIGS solar cells, enabled due to suitable addition of alkali metals, the importance of these alkali metals cannot be emphasized enough although a complete picture of the mechanisms through which this is achieved remain far from being clearly understood. Being a polycrystalline material, CIGS is considered to be dominated by trap states within the bandgap leading to non-radiative Shockley-Read-Hall recombination. It is plausible to expect that the passivation of these deep defect states contributes to improvement in the device performance, because of superior electronic quality of the absorber material. To enable the characterization of trap states in the CIGS treated with heavier alkali elements (KF and RbF) in addition to Na, we applied a carefully chosen sets of experimental conditions, characterization tools, and modeling. We showed that the increase in device efficiency due to the addition of potassium as well as rubidium by post-deposition annealing of the CIGS absorber layer is partly related to an apparent majority carrier concentration enhancement, an improvement in minority carrier lifetime and a reduction of the  $E_v+0.98$  eV trap concentration. The post-deposition annealing of CIGS with heavier alkali (KF, RbF) had no discernable effect on the concentration of the mid-band gap trap, observed around  $E_v+0.55$  eV. Interfaces and grain boundaries are recognized as locations where traps are present in higher density. By taking advantage of the capacity of scanning DLTS measurements, the locations of mid-bandgap traps at  $E_v+0.55$  eV were characterized. We observed these traps to show a higher response in certain grain boundaries compared to the intragrain regions, although the exact origin of this effect has not been identified. With the application of temperature dependent current-voltage measurements, we observed that the dominant recombination in the Rb treated device stayed in the space charge region as in the case of a device containing Na only.

Despite the positive effects in efficiency, alkali metal (such as sodium) was shown to participate in the device degradation caused by damp heat exposure. In the case

of oxidized Mo, sodium seemed to be accumulated in a relatively higher amount as noted in the secondary ion mass spectrometry profiles, when annealed at CIGS deposition temperature. Alternatively, sodium diffusion was observed to be hindered through Mo in the CIGS prepared on the damp heat exposed molybdenum layer. When devices were completed on oxidized Mo, a loss in performance was observed, mostly due to the limited sodium diffusion while the rest of the degradation was attributed to the deterioration of the Mo/CIGS interface. Additionally, the molybdenum layer was observed to be very sensitive to the moisture, resulting in micro-structural modifications, morphological changes, as well as loss of conductivity and reflectivity. While bare CIGS layers did not show notable micro-structural modifications within the scope of the experimental conditions used to study the effect of damp heat treatment, alkali migration was observed to occur leading mainly to a loss of open circuit voltage and fill factor in the solar cells prepared on those films. The surface modification was observed to be due mainly due to the oxidation of chemical species. We also observed a loss in the electronic quality of CIGS, in the form of reduced carrier concentration, increase in  $E_v+0.65/0.98$  eV trap level and reduced photoluminescence intensity. The negative impact of damp heat exposure on the device performance, either of Mo back contact or the CIGS layer, showed that CIGS devices are vulnerable to such treatment. Alternative solutions were offered, where additional alkali supplied to the layer can allow for nearly full recovery of the efficiency.

## REFERENCES

- [1] E. Kabir, P. Kumar, S. Kumar, A. A. Adelodun, and K.H. Kim, "Solar energy: Potential and future prospects," *Renewable and Sustainable Energy Reviews*, vol. 82, pp. 894-900, 2018.
- [2] Renewables 2018 Global status report, 2018. Available: <http://www.ren21.net/gsr-2018/>
- [3] T. D. Lee and A. U. Ebong, "A review of thin film solar cell technologies and challenges," *Renewable and Sustainable Energy Reviews*, vol. 70, pp. 1286-1297, 2017.
- [4] M. A. Green, Y. Hishikawa, E. D. Dunlop, D. H. Levi, J. Hohl-Ebinger, and A. W. Y. Ho-Baillie, "Solar cell efficiency tables (version 52)," *Progress in Photovoltaics: Research and Applications*, vol. 26, no. 7, pp. 427-436, 2018.
- [5] A. Polman, M. Knight, E. C. Garnett, B. Ehrler, and W. C. Sinke, "Photovoltaic materials: Present efficiencies and future challenges," *Science*, vol. 352, no. 6283, 2016.
- [6] G. Kavlak, J. McNerney, and J. E. Trancik, "Evaluating the causes of cost reduction in photovoltaic modules," *Energy Policy*, vol. 123, pp. 700-710, 2018.
- [7] G. Fisher, M. R. Seacrist, and R. Standley, "Silicon crystal growth and wafer technologies," *Proceedings of the IEEE*, 100(Special Centennial Issue), pp. 1454-1474, 2012.
- [8] M. Powalla et al., "Advances in cost-efficient thin-film photovoltaics based on Cu(In,Ga)Se<sub>2</sub>," *Engineering*, vol. 3, no. 4, pp. 445-451, 2017.
- [9] T. Feurer et al., "Progress in thin film CIGS photovoltaics – Research and development, manufacturing, and applications," *Progress in Photovoltaics: Research and Applications*, vol. 25, no. 7, pp. 645-667, 2017.
- [10] F. Meillaud et al., "Recent advances and remaining challenges in thin-film silicon photovoltaic technology," *Materials Today*, vol. 18, no. 7, pp. 378-384, 2015.



- [11] T. Zhang et al., "High efficiency solution-processed thin-film Cu(In,Ga)(Se,S)<sub>2</sub> solar cells," *Energy & Environmental Science*, vol. 9, no. 12, pp. 3674-3681, 2016.
- [12] T. Kato et.al., "Record Efficiency for Thin-Film Polycrystalline Solar Cells Up to 22.9% Achieved by Cs-Treated Cu(In,Ga)(Se,S)<sub>2</sub>," *IEEE Journal of Photovoltaics*, vol.9, no. 1, pp. 325-330, 2019.
- [13] T. Feurer et al., "RbF post deposition treatment for narrow bandgap Cu(In,Ga)Se<sub>2</sub> solar cells," *Thin Solid Films*, vol. 670, pp. 34-40, 2019.
- [14] W. Shockley and H. J. Queisser, "Detailed balance limit of efficiency of p-n junction solar cells," *Journal of Applied Physics*, vol. 32, no. 3, pp. 510-519, 1961.
- [15] P. Jackson et al., "High quality baseline for high efficiency, Cu(In<sub>1-x</sub>,Ga<sub>x</sub>)Se<sub>2</sub> solar cells," *Progress in Photovoltaics: Research and Applications*, vol. 15, no. 6, pp. 507-519, 2007.
- [16] S. Ishizuka, A. Yamada, P. J. Fons, H. Shibata, and S. Niki, "Structural tuning of wide-gap chalcopyrite CuGaSe<sub>2</sub> thin films and highly efficient solar cells: differences from narrow-gap Cu(In,Ga)Se<sub>2</sub>," *Progress in Photovoltaics: Research and Applications*, vol. 22, no. 7, pp. 821-829, 2014.
- [17] P. K. Paul, K. Aryal, S. Marsillac, S. A. Ringel, and A. R. Arehart, "Impact of the Ga/In ratio on defects in Cu(In, Ga)Se<sub>2</sub>," *IEEE 43<sup>rd</sup> Photovoltaic Specialists Conference (PVSC)*, pp. 2246-2249, 2016.
- [18] M. A. Contreras et al., "Wide bandgap Cu(In,Ga)Se<sub>2</sub> solar cells with improved energy conversion efficiency," *Progress in Photovoltaics: Research and Applications*, vol. 20, no. 7, pp. 843-850, 2012.
- [19] P. Jackson et al., "Properties of Cu(In,Ga)Se<sub>2</sub> solar cells with new record efficiencies up to 21.7%," *Physica Status Solidi (RRL) – Rapid Research Letters*, vol. 9, no. 1, pp. 28-31, 2015.
- [20] A. Chirila et al., "Highly efficient Cu (In, Ga)Se<sub>2</sub> solar cells grown on flexible polymer films," *Nature materials*, vol. 10, no. 11, pp. 857-861, 2011.

- [21] R. Scheer and H.W. Schock, "Chalcogenide photovoltaics: physics, technologies, and thin film devices", John Wiley & Sons, 2011.
- [22] J. Hedstrom et al., "ZnO/CdS/Cu(In,Ga)Se<sub>2</sub> thin film solar cells with improved performance," *IEEE Twenty Third Photovoltaic Specialists Conference*, pp. 364-371, 1993.
- [23] K. Granath, M. Bodegard, and L. Stolt, "The effect of NaF on Cu(In,Ga)Se<sub>2</sub> thin film solar cells," *Solar Energy Materials and Solar Cells*, vol. 60, no. 3, pp. 279-293, 2000.
- [24] M. Bodegard, K. Granath, and L. Stolt, "Growth of Cu (In,Ga)Se<sub>2</sub> thin films by coevaporation using alkaline precursors," *Thin Solid Films*, vol. 361, pp. 9-16, 2000.
- [25] S. Ishizuka et al., "Na-induced variations in the structural, optical, and electrical properties of Cu(In, Ga)Se<sub>2</sub> thin films," *Journal of Applied Physics*, vol. 106, no. 3, p. 034908, 2009.
- [26] D. Rudmann et al., "Efficiency enhancement of Cu(In,Ga)Se<sub>2</sub> solar cells due to post-deposition Na incorporation," *Applied Physics Letters*, vol. 84, no. 7, pp. 1129-1131, 2004.
- [27] P. Salom, V. Fjllstrm, A. Hultqvist, and M. Edoff, "Na Doping of CIGS Solar Cells Using Low Sodium-Doped Mo Layer," *IEEE Journal of Photovoltaics*, vol. 3, no. 1, pp. 509-513, 2013.
- [28] C.H. Hsu et al., "Na-induced efficiency boost for Se-deficient Cu(In,Ga)Se<sub>2</sub> solar cells," *Progress in Photovoltaics: Research and Applications*, vol. 23, no. 11, pp. 1621-1629, 2015.
- [29] D. Rudmann, G. Bilger, M. Kaelin, F. J. Haug, H. Zogg, and A. N. Tiwari, "Effects of NaF coevaporation on structural properties of Cu(In,Ga)Se<sub>2</sub> thin films," *Thin Solid Films*, vol. 431-432, pp. 37-40, 2003.
- [30] K. Granath, M. Bodegard, and L. Stolt, "The effect of NaF on Cu(In, Ga)Se<sub>2</sub> thin film solar cells," *Solar Energy Materials and Solar Cells*, vol. 60, no. 3, pp. 279-293, 2000.

- [31] T. Nakada, "Invited Paper: CIGS-based thin film solar cells and modules: Unique material properties," *Electronic Materials Letters*, vol. 8, no. 2, pp. 179-185, 2012.
- [32] O. Cojocaru-Mirédin, T. Schwarz, P.-P. Choi, M. Herbig, R. Wuerz, and D. Raabe, "Atom Probe Tomography Studies on the Cu(In,Ga)Se<sub>2</sub> Grain Boundaries," *Journal of Visualized Experiments : JoVE*, no. 74, p. 50376, 2013.
- [33] J. Keller et al., "Grain boundary investigations on sulfurized Cu(In,Ga)(S,Se)<sub>2</sub> solar cells using atom probe tomography," *Solar Energy Materials and Solar Cells*, vol. 117, pp. 592-598, 2013.
- [34] E. Cadel, N. Barreau, J. Kessler, and P. Pareige, "Atom probe study of sodium distribution in polycrystalline Cu(In,Ga)Se<sub>2</sub> thin film," *Acta Materialia*, vol. 58, no. 7, pp. 2634-2637, 2010.
- [35] D. Braunger, D. Hariskos, G. Bilger, U. Rau, and H. Schock, "Influence of sodium on the growth of polycrystalline Cu(In,Ga)Se<sub>2</sub> thin films," *Thin Solid Films*, vol. 361, pp. 161-166, 2000.
- [36] S. Karki et al., "In Situ and Ex Situ Investigations of KF Postdeposition Treatment Effects on CIGS Solar Cells," *IEEE Journal of Photovoltaics*, vol. 7, no. 2, pp. 665-669, 2017.
- [37] P. M. P. Salom et al., "Cu(In,Ga)Se<sub>2</sub> Solar Cells With Varying Na Content Prepared on Nominally Alkali-Free Glass Substrates," *IEEE Journal of Photovoltaics*, vol. 3, no. 2, pp. 852-858, 2013.
- [38] H. Stange et al., "Effect of Na presence during CuInSe<sub>2</sub> growth on stacking fault annihilation and electronic properties," *Applied Physics Letters*, vol. 107, no. 15, p. 152103, 2015.
- [39] S.H. Wei, S. Zhang, and A. Zunger, "Effects of Na on the electrical and structural properties of CuInSe<sub>2</sub>," *Journal of Applied Physics*, vol. 85, no. 10, pp. 7214-7218, 1999.
- [40] D. J. Schroeder and A. Rockett, "Electronic effects of sodium in epitaxial CIGS," *Journal of Applied Physics*, vol. 82, no. 10, pp. 4982-4985, 1997.

- [41] D. W. Niles, M. Al-Jassim and, K. Ramanathan, "Direct observation of Na and O impurities at grain surfaces of CuInSe<sub>2</sub> thin films," *Journal of Vacuum Science & Technology A: Vacuum, Surfaces, and Films*, vol. 17, no. 1, pp. 291-296, 1999.
- [42] Z.K. Yuan et al., "Na-Diffusion Enhanced p-type Conductivity in Cu(In,Ga)Se<sub>2</sub>: A New Mechanism for Efficient Doping in Semiconductors," *Advanced Energy Materials*, vol. 6, no. 24, pp. 1601191, 2016.
- [43] M. A. Contreras et al., "On the role of Na and modifications to Cu(In,Ga)Se<sub>2</sub> absorber materials using thin-MF (M= Na, K, Cs) precursor layers [solar cells]," *IEEE Twenty-Sixth Photovoltaic Specialists Conference*, pp. 359-362, 1997.
- [44] A. Chirila et al., "Potassium-induced surface modification of Cu(In,Ga)Se<sub>2</sub> thin films for high-efficiency solar cells," *Nature materials*, vol. 12, no. 12, pp. 1107-1111, 2013.
- [45] P. Jackson, R. Wuerz, D. Hariskos, E. Lotter, W. Witte, and M. Powalla, "Effects of heavy alkali elements in Cu(In,Ga)Se<sub>2</sub> solar cells with efficiencies up to 22.6%," *Physica Status Solidi (RRL) – Rapid Research Letters*, vol.10, no. 6, pp.583-586, 2016.
- [46] T. Lepetit, S. Harel, L. Arzel, G. Ouvrard, N. Barreau,"KF post deposition treatment in co-evaporated Cu(In, Ga)Se<sub>2</sub> thin film solar cells: Beneficial or detrimental effect induced by the absorber characteristics," *Progress in Photovoltaics: Research and Applications*, vol. 25, no. 12, pp. 1068-1076, 2017.
- [47] E. Avancini et al., "Effects of rubidium fluoride and potassium fluoride post deposition treatments on Cu(In,Ga)Se<sub>2</sub> thin films and solar cell performance," *Chemistry of Materials*, vol. 29, no. 22, pp. 9695-9704, 2017.
- [48] S. Kim, H. Tampo, H. Shibata, K. Matsubara, and S. Niki, "Effect of Combined Alkali (KF + CsF) Post-Deposition Treatment on Cu(In,Ga)Se<sub>2</sub> Solar Cells," *Physica Status Solidi (RRL)–Rapid Research Letters* vol. 12, no. 10, p. 1800372, 2018.
- [49] M. Malitckaya, H.P. Komsa, V. Havu, and M. J. Puska, "Effect of alkali metal atom doping on the CuInSe<sub>2</sub>-based solar cell absorber," *The Journal of Physical Chemistry C*, vol. 121, no. 29, pp. 15516-15528, 2017.

- [50] N. Taguchi, S. Tanaka, and S. Ishizuka, "Direct insights into RbInSe<sub>2</sub> formation at Cu(In,Ga)Se<sub>2</sub> thin film surface with RbF postdeposition treatment," *Applied Physics Letters*, vol. 113, no. 11, p. 113903, 2018.
- [51] N. Maticiuc et al., "In vacuo XPS investigation of Cu(In,Ga)Se<sub>2</sub> surface after RbF post-deposition treatment," *Thin Solid Films*, vol.665, pp.143-147, 2018.
- [52] E. Handick et al., "Potassium Postdeposition Treatment-Induced Band Gap Widening at Cu(In,Ga)Se<sub>2</sub> Surfaces—Reason for Performance Leap," *ACS applied materials & interfaces*, vol. 7, no. 49, pp. 27414-27420, 2015.
- [53] M. Theelen and F. Daume, "Stability of Cu(In, Ga)Se<sub>2</sub> solar cells: A literature review," *Solar Energy*, vol. 133, pp. 586-627, 2016.
- [54] C. P. Muzzillo et al., "Potential—Induced Degradation of Cu(In,Ga)Se<sub>2</sub> Solar Cells : Alkali Metal Drift and Diffusion Effects," *IEEE Journal of Photovoltaics*, no. 99, pp. 1-6, 2018.
- [55] V. Fjallstrom et al., "Potential-Induced Degradation of Cu(In<sub>1-x</sub>,Ga<sub>x</sub>)Se<sub>2</sub> Thin Film Solar Cells," *IEEE Journal of Photovoltaics*, vol. 3, no. 3, pp. 1090-1094, 2013.
- [56] M. Theelen, V. Hans, N. Barreau, H. Steijvers, Z. Vroon, and M. Zeman, "The impact of alkali elements on the degradation of CIGS solar cells," *Progress in Photovoltaics: Research and Applications*, vol. 23, no. 5, pp. 537-545, 2015.
- [57] N. Jiro et al., "Effects of long—term heat—light soaking on Cu(In,Ga)Se<sub>2</sub> solar cells with KF postdeposition treatment," *Applied Physics Express*, vol. 10, no. 9, pp. 092301, 2017.
- [58] S. Chen et al., "Light soaking induced doping increase and sodium redistribution in Cu(In,Ga)Se<sub>2</sub>-based thin film solar cells," *Thin Solid Films*, vol. 582, pp. 35-38, 2015.
- [59] F. Daume et al., "Damp Heat Treatment of Cu (In, Ga)Se<sub>2</sub> Solar Cells with Different Sodium Content," *Materials*, vol. 6, no. 12, pp. 5478-5489, 2013.
- [60] S. Lany and A. Zunger, "Light- and bias-induced metastabilities in Cu(In,Ga)Se<sub>2</sub> based solar cells caused by the (V<sub>Se</sub>-V<sub>Cu</sub>) vacancy complex," *Journal of Applied Physics*, vol. 100, no. 11, pp. 113725, 2006.

- [61] D.W. Lee et al., "Damp heat and thermal cycling-induced degradation mechanism of AZO and CIGS films in Cu(In,Ga)Se<sub>2</sub> photovoltaic modules," *Current Applied Physics*, vol. 15, no. 3, pp. 285-291, 2015.
- [62] U. Rau et al., "Oxygenation and air-annealing effects on the electronic properties of Cu(In,Ga)Se<sub>2</sub> films and devices," *Journal of Applied Physics*, vol. 86, no. 1, pp. 497-505, 1999.
- [63] D. Braunger, D. Hariskos, and H. Schock, "Na-related stability issues in highly efficient polycrystalline Cu(In,Ga)Se<sub>2</sub> solar cells," *IEEE 2nd World Conference on Photovoltaic Energy Conversion (WCPEC)*, vol. 1, pp. 511-514, 1998.
- [64] C. Heske et al., "Influence of Na and H<sub>2</sub>O on the surface properties of Cu(In,Ga)Se<sub>2</sub> thin films," *Journal of applied physics*, vol. 82, no. 5, pp. 2411-2420, 1997.
- [65] R. Würz et al., "In situ X-ray photoelectron spectroscopy study of the oxidation of CuGaSe<sub>2</sub>," *Surface Science*, vol. 580, no. 1, pp. 80-94, 2005.
- [66] W. K. Metzger, I. L. Repins, and M. Contreras, "Long lifetimes in high-efficiency Cu(In,Ga)Se<sub>2</sub> solar cells," *Applied Physics Letters*, vol. 93, no. 2, 2008.
- [67] W. K. Metzger et al., "Recombination kinetics and stability in polycrystalline Cu(In,Ga)Se<sub>2</sub> solar cells," *Thin Solid Films*, vol. 517, no. 7, pp. 2360-2364, 2009.
- [68] P. R. Elowe, M. A. Stempki, S. J. Rozeveld, and M. W. DeGroot, "Development of Direct Cell Inorganic Barrier Film Technology Providing Exceptional Device Stability for CIGS Solar Cells," *Chemistry of Materials*, vol. 23, no. 17, pp. 3915-3920, 2011.
- [69] M. Theelen et al., "In Situ Monitoring of the Accelerated Performance Degradation of Solar Cells and Modules: A Case Study for Cu(In,Ga)Se<sub>2</sub> Solar Cells," *Journal of visualized experiments: JoVE*, no. 140, 2018.
- [70] I. Khatri, K. Shudo, J. Matsuura, M. Sugiyama, and T. Nakada, "Impact of heat-light soaking on potassium fluoride treated CIGS solar cells with CdS buffer layer," *Progress in Photovoltaics: Research and Applications*, vol. 26, no.3, pp. 171-178, 2018.

- [71] R. Farshchi, B. Hickey, G. Zapalac, J. Bailey, D. Spaulding, and D. Poplavskyy, "Mechanisms for light-soaking induced carrier concentration changes in the absorber layer of Cu(In,Ga)Se<sub>2</sub> solar cells," *IEEE 44th Photovoltaic Specialist Conference (PVSC)*, pp. 1-4, 2017.
- [72] F. Daume et al., "Damp Heat Treatment of Cu(In,Ga)Se<sub>2</sub> Solar Cells with Different Sodium Content," *Materials* vol. 6, no. 12, p. 5478, 2013.
- [73] S. Karki et al., "Investigation of traps density and position in alkali treated Cu(In,Ga)Se<sub>2</sub> thin films and solar cells," *IEEE 44th Photovoltaic Specialist Conference (PVSC)*, pp. 2446-2448, 2017.
- [74] S. Karki et al., "Analysis of Recombination Mechanisms in RbF-Treated CIGS Solar Cells," *IEEE Journal of Photovoltaics*, vol. 9, no. 1, pp. 313-318, 2019.
- [75] S. Karki, P. Paul, G. Rajan, A. Rockett, A. Arehart, and S. Marsillac, "Characterization of electronic defects in RbF treated CIGS solar cells," " *IEEE 7th World Conference on Photovoltaic Energy Conversion (WCPEC) (A Joint Conference of 45th IEEE PVSC, 28th PVSEC & 34th EU PVSEC)*, pp. 1906-1908, 2018.
- [76] G. Rajan et al., "Study of Instabilities and Degradation due to Moisture Ingress in the Molybdenum back contact of Cu(In,Ga)Se<sub>2</sub> Solar Cells," *IEEE 7th World Conference on Photovoltaic Energy Conversion (WCPEC) (A Joint Conference of 45th IEEE PVSC, 28th PVSEC & 34th EU PVSEC)*, pp. 3037-3039, 2018.
- [77] P. K. Paul, S. Karki, G. Rajan, S. Marsillac, and A. R. Arehart, "Impact of moisture ingress on the degradation and trap spectrum in Cu(In,Ga)Se<sub>2</sub> solar cells," *IEEE 7th World Conference on Photovoltaic Energy Conversion (WCPEC) (A Joint Conference of 45th IEEE PVSC, 28th PVSEC & 34th EU PVSEC)*, pp. 2623-2626, 2018.
- [78] J. Nelson, " *The Physics of Solar Cells*," Imperial College Press, 2003.
- [79] A. Luque and S. Hegedus, " *Handbook of photovoltaic science and engineering*," John Wiley & Sons, 2011.
- [80] S. M. Sze and K. K. Ng, " *Physics of semiconductor devices*," John Wiley & Sons, 2006.

- [81] C. Honsberg and S. J. Bowden, "PV education," 2014. Available: <https://www.pveducation.org>
- [82] A. Freundlich, P. Verlinden, and W. van Sark, "Photovoltaic Solar Energy: From Fundamentals to Applications, John Wiley & Sons, 2017.
- [83] J.-P. Colinge and C. A. Colinge, "Physics of semiconductor devices," Springer Science & Business Media, 2005.
- [84] R. Wuerz, A. Eicke, F. Kessler, S. Paetel, S. Efimenko, and C. Schlegel, "CIGS thin-film solar cells and modules on enamelled steel substrates," *Solar Energy Materials and Solar Cells*, vol. 100, pp. 132-137, 2012.
- [85] P. Reinhard et al., "Review of progress toward 20% efficiency flexible CIGS solar cells and manufacturing issues of solar modules," *IEEE 38th Photovoltaic Specialists Conference (PVSC)*, vol.2, pp. 1-9, 2012.
- [86] J. E. Granata, J. R. Sites, S. Asher, and R. J. Matson, "Quantitative incorporation of sodium in  $\text{CuInSe}_2$  and  $\text{Cu(In,Ga)Se}_2$  photovoltaic devices," *IEEE Twenty-Sixth Photovoltaic Specialists Conference*, pp. 387-390, 1997.
- [87] J. M. Raguse, C. P. Muzzillo, J. R. Sites, and L. Mansfield, "Effects of Sodium and Potassium on the Photovoltaic Performance of CIGS Solar Cells," *IEEE Journal of Photovoltaics*, vol. 7, no. 1, pp. 303-306, 2017.
- [88] S. Nishiwaki, N. Kohara, T. Negami, and T. Wada, "MoSe<sub>2</sub> layer formation at Cu(In,Ga)Se<sub>2</sub>/Mo Interfaces in High Efficiency Cu(In<sub>1-x</sub>Ga<sub>x</sub>)Se<sub>2</sub> Solar Cells," *Japanese Journal of Applied Physics*, vol. 37, no. 1A, p. L71, 1998.
- [89] D. Abou-Ras et al., "Formation and characterisation of MoSe<sub>2</sub> for Cu(In,Ga)Se<sub>2</sub> based solar cells," *Thin Solid Films*, vol. 480-481, pp. 433-438, 2005.
- [90] S. A. Pethe, E. Takahashi, A. Kaul, and N. G. Dhere, "Effect of sputtering process parameters on film properties of molybdenum back contact," *Solar Energy Materials and Solar Cells*, vol. 100, pp. 1-5, 2012.
- [91] H. Khatri and S. Marsillac, "The effect of deposition parameters on radiofrequency sputtered molybdenum thin films," *Journal of Physics: Condensed Matter*, vol. 20, no. 5, p. 055206, 2008.



- [92] G. K. Rane, S. Menzel, T. Gemming, and J. Eckert, "Microstructure, electrical resistivity and stresses in sputter deposited W and Mo films and the influence of the interface on bilayer properties," *Thin Solid Films*, vol. 571, pp. 1-8, 2014.
- [93] J. H. Scofield, A. Duda, D. Albin, B. Ballard, and P. Predecki, "Sputtered molybdenum bilayer back contact for copper indium diselenide-based polycrystalline thin-film solar cells," *Thin solid films*, vol. 260, no. 1, pp. 26-31, 1995.
- [94] P. Salome, J. Malaquias, P. Fernandes, and A. Da Cunha, "Mo bilayer for thin film photovoltaics revisited," *Journal of Physics D: Applied Physics*, vol. 43, no. 34, p. 345501, 2010.
- [95] S. Ishizuka, A. Yamada, P. Fons, and S. Niki, "Texture and morphology variations in (In,Ga)<sub>2</sub>Se<sub>3</sub> and Cu(In,Ga)Se<sub>2</sub> thin films grown with various Se source conditions," *Progress in Photovoltaics: Research and Applications*, vol. 21, no. 4, pp. 544-553, 2013.
- [96] K. Orgassa, H. W. Schock, and J. H. Werner, "Alternative back contact materials for thin film Cu(In,Ga)Se<sub>2</sub> solar cells," *Thin Solid Films*, vol. 431-432, pp. 387-391, 2003.
- [97] B. J. Stanbery, "Copper indium selenides and related materials for photovoltaic devices," *Critical reviews in solid state and materials sciences*, vol. 27, no. 2, pp. 73-117, 2002.
- [98] J. S. Park, Z. Dong, S. Kim, and J. H. Perepezko, "CuInSe<sub>2</sub> phase formation during Cu<sub>2</sub>Se/In<sub>2</sub>Se<sub>3</sub> interdiffusion reaction," *Journal of Applied Physics*, vol. 87, no. 8, pp. 3683-3690, 2000.
- [99] M. I. Alonso, M. Garriga, C. D. Rincon, E. Hernandez, and M. Leon, "Optical functions of chalcopyrite CuGa<sub>x</sub>In<sub>1-x</sub>Se<sub>2</sub> alloys," *Applied Physics A*, vol. 74, no. 5, pp. 659-664, 2002.
- [100] P. Paulson, R. Birkmire, and W. Shafarman, "Optical characterization of CuIn<sub>1-x</sub>Ga<sub>x</sub>Se<sub>2</sub> alloy thin films by spectroscopic ellipsometry," *Journal of Applied Physics*, vol. 94, pp. 879-888, 2003.
- [101] P. Aryal et al., "Parameterized complex dielectric functions of CIGS applications in optical characterization of compositional non-uniformities and depth

- profiles in materials and solar cells," *Progress in Photovoltaics: Research and Applications*, vol. 24, no.9, pp. 1200-1213, 2016.
- [102] S. Minoura, K. Kodera, T. Maekawa, K. Miyazaki, S. Niki, and H. Fujiwara, "Dielectric function of Cu (In,Ga)Se<sub>2</sub>-based polycrystalline materials," *Journal of Applied Physics*, vol. 113, no. 6, pp. 063505, 2013.
- [103] M. I. Alonso, K. Wakita, J. Pascual, M. Garriga, and N. Yamamoto, "Optical functions and electronic structure of CuInSe<sub>2</sub>, CuGaSe<sub>2</sub>, CuInS<sub>2</sub>, and CuGaS<sub>2</sub>," *Physical Review B*, vol. 63, no. 7, p. 075203, 2001.
- [104] S. Minoura, T. Maekawa, K. Kodera, A. Nakane, S. Niki, and H. Fujiwara, "Optical constants of Cu(In,Ga)Se<sub>2</sub> for arbitrary Cu and Ga compositions," *Journal of Applied Physics*, vol. 117, no. 19, p. 195703, 2015.
- [105] J. E. Jaffe and A. Zunger, "Theory of the band-gap anomaly in ABC<sub>2</sub> chalcopyrite semiconductors," *Physical Review B*, vol. 29, no. 4, pp. 1882-1906, 1984.
- [106] S.H. Wei, S. B. Zhang, and A. Zunger, "Effects of Ga addition to CuInSe<sub>2</sub> on its electronic, structural, and defect properties," *Applied Physics Letters*, vol. 72, no. 24, pp. 3199-3201, 1998.
- [107] G. Hodes, "Chemical solution deposition of semiconductor films," *CRC press*, 2002.
- [108] Y. Hashimoto, N. Kohara, T. Negami, N. Nishitani and, N. Wada, "Chemical bath deposition of Cds buffer layer for GIGS solar cells," *Solar Energy Materials and Solar Cells*, vol. 50, no. 1-4, pp. 71-77, 1998.
- [109] W. Witte, D. Abou-Ras, and D. Hariskos, "Chemical bath deposition of Zn(O,S) and CdS buffers: Influence of Cu(In,Ga)Se<sub>2</sub> grain orientation," *Applied Physics Letters*, vol. 102, no. 5, p. 051607, 2013.
- [110] C.S. Jiang, R. Noufi, K. Ramanathan, H. Moutinho, and M. Al-Jassim, "Electrical modification in Cu(In,Ga)Se<sub>2</sub> thin films by chemical bath deposition process of CdS films," *Journal of applied physics*, vol. 97, no. 5, p. 053701, 2005.

- [111] J. Chantana, T. Kato, H. Sugimoto, and T. Minemoto, "20% Efficient  $\text{Zn}_{0.9}\text{Mg}_{0.10}:\text{Al}/\text{Zn}_{0.8}\text{Mg}_{0.20}/\text{Cu}(\text{In},\text{Ga})(\text{S},\text{Se})_2$  Solar Cell Prepared by All-Dry Process through a Combination of Heat-Light-Soaking and Light-Soaking Processes," *ACS Applied Materials & Interfaces*, vol. 10, no. 13, pp.11361-11368, 2018.
- [112] T. Kato et al., "Enhanced Efficiency of Cd-Free  $\text{Cu}(\text{In},\text{Ga})(\text{Se},\text{S})_2$  Minimodule Via  $(\text{Zn},\text{Mg})\text{O}$  Second Buffer Layer and Alkali Metal Post-Treatment," *IEEE Journal of Photovoltaics*, vol.7, no. 6, pp.1773-1780, 2017.
- [113] D. Hariskos, S. Spiering, and M. Powalla, "Buffer layers in  $\text{Cu}(\text{In},\text{Ga})\text{Se}_2$  solar cells and modules," *Thin Solid Films*, vol. 480-481, pp. 99-109, 2005.
- [114] R. Menner, S. Paetel, W. Wischmann, and M. Powalla, "Indium zinc oxide window layer for high-efficiency  $\text{Cu}(\text{In},\text{Ga})\text{Se}_2$  solar cells," *Thin Solid Films*, vol.634, pp.160-164, 2017.
- [115] C. P. Thompson, L. Chen, W. N. Shafarman, J. Lee, S. Fields, and R. W. Birkmire, "Bandgap gradients in  $(\text{Ag},\text{Cu})(\text{In},\text{Ga})\text{Se}_2$  thin film solar cells deposited by three-stage co-evaporation," *IEEE 42nd Photovoltaic Specialist Conference (PVSC)*, pp. 1-6, 2015.
- [116] M. A. Contreras et al., "High efficiency  $\text{Cu}(\text{In},\text{Ga})\text{Se}_2$ -based solar cells: processing of novel absorber structures," *IEEE Twenty Fourth Photovoltaic Specialists Conference*, vol. 1, pp. 68-75, 1994.
- [117] J. C. Vickerman and I. Gilmore, "Surface analysis: the principal techniques," John Wiley & Sons, 2011.
- [118] D. V. Lang, "Deep-level transient spectroscopy: A new method to characterize traps in semiconductors," *Journal of Applied Physics*, vol. 45, no. 7, pp. 3023-3032, 1974.
- [119] D. K. Schroder, "Semiconductor material and device characterization," John Wiley & Sons, 2006.
- [120] H. Fujiwara, "Spectroscopic ellipsometry: principles and applications," John Wiley & Sons, 2007.

- [121] A. Niemegeers, S. Gillis, and M. Burgelman, "A user program for realistic simulation of polycrystalline heterojunction solar cells: SCAPS-1D," *Proceedings of the IEEE 2nd World Conference on Photovoltaic Energy Conversion, JRC, European Commission*, pp. 672-675, 1998.
- [122] D. Rudmann et al., "Efficiency enhancement of Cu(In,Ga)Se<sub>2</sub> solar cells due to post-deposition Na incorporation," *Applied Physics Letters*, vol. 84, no. 7, pp. 1129-1131, 2004.
- [123] N. Tokio, I. Daisuke, O. Hiroki, and K. Akio, "Effects of Sodium on Cu(In,Ga)Se<sub>2</sub>-Based Thin Films and Solar Cells," *Japanese Journal of Applied Physics*, vol. 36, no. 2R, p. 732, 1997.
- [124] A. Laemmle, R. Wuerz, and M. Powalla, "Efficiency enhancement of Cu(In,Ga)Se<sub>2</sub> thin-film solar cells by a post-deposition treatment with potassium fluoride," *physica status solidi (RRL)-Rapid Research Letters*, vol. 7, no. 9, pp. 631-634, 2013.
- [125] A. Laemmle, R. Wuerz, and M. Powalla, "Investigation of the effect of potassium on Cu(In,Ga)Se<sub>2</sub> layers and solar cells," *Thin Solid Films*, vol. 582, pp. 27-30, 2015.
- [126] D. Abou-Ras, T. Kirchartz, and U. Rau, "Advanced Characterization Techniques for Thin Film Solar Cells," Wiley, 2016.
- [127] K. Naoki, N. Takayuki, N. Mikihiro, and W. Takahiro, "Preparation of Device-Quality Cu(In,Ga)Se<sub>2</sub> Thin Films Deposited by Coevaporation with Composition Monitor," *Japanese Journal of Applied Physics*, vol. 34, no. 9A, p. L1141, 1995.
- [128] P. Aryal et al., "Real-Time, In-Line, and Mapping Spectroscopic Ellipsometry for Applications in Cu(In<sub>1-x</sub>Ga<sub>x</sub>)Metrology," *IEEE Journal of Photovoltaics*, vol. 4, no. 1, pp. 333-339, 2014.
- [129] P. Pradhan et al., "Real time spectroscopic ellipsometry analysis of the three-stages of CuIn<sub>1-x</sub>Ga<sub>x</sub>Se<sub>2</sub> co-evaporation," *IEEE 40th Photovoltaic Specialist Conference (PVSC)*, pp. 2060-2065, 2014.

- [130] D. Attygalle et al., "Optical monitoring and control of three-stage coevaporated  $\text{Cu}(\text{In}_{1-x}\text{Ga}_x)\text{Se}_2$  by real-time spectroscopic ellipsometry," *IEEE 38th Photovoltaic Specialists Conference (PVSC)*, Volume 2, pp. 1-6, 2012.
- [131] S. B. Zhang, S.H. Wei, A. Zunger, and H. Katayama-Yoshida, "Defect physics of the  $\text{CuInSe}_2$  chalcopyrite semiconductor," *Physical Review B*, vol. 57, no. 16, pp. 9642-9656, 1998.
- [132] A. Arehart, S. Ringel, A. Corrion, C. Poblenz, J. Speck, and U. Mishra, "Deep level optical and thermal spectroscopy of traps in n-GaN grown by ammonia molecular beam epitaxy," *Applied Physics Letters*, vol. 93, no. 11, 2008.
- [133] G. Lucovsky, "On the photoionization of deep impurity centers in semiconductors," *Solid State Communications*, vol. 3, no. 9, pp. 299-302, 1965.
- [134] I. Repins et al., "Comparison of device performance and measured transport parameters in widely-varying  $\text{Cu}(\text{In}, \text{Ga})(\text{Se}, \text{S})$  solar cells," *Progress in Photovoltaics: Research and Applications*, vol. 14, no. 1, pp. 25-43, 2006.
- [135] R. Caballero et al., "Influence of Na on  $\text{Cu}(\text{In}, \text{Ga})\text{Se}_2$  solar cells grown on polyimide substrates at low temperature: impact on the  $\text{Cu}(\text{In}, \text{Ga})\text{Se}_2/\text{Mo}$  interface," *Applied Physics Letters*, vol. 96, no. 9, p. 092104, 2010.
- [136] N. Nicoara et al., "Evidence for Chemical and Electronic Nonuniformities in the Formation of the Interface of RbF-Treated  $\text{Cu}(\text{In}, \text{Ga})\text{Se}_2$  with CdS," *ACS Applied Materials & Interfaces*, vol. 9, no. 50, pp. 44173-44180, 2017.
- [137] M. Malitckaya, H.-P. Komsa, V. Havu, and M. Puska, "Effect of alkali metal atom doping on the  $\text{CuInSe}_2$ -based solar cell absorber," *The Journal of Physical Chemistry C*, vol. 121, no. 29, pp. 15516-15528, 2017.
- [138] S. Ishizuka, N. Taguchi, J. Nishinaga, Y. Kamikawa, S. Tanaka, and H. Shibata, "Group III Elemental Composition Dependence of RbF Postdeposition Treatment Effects on  $\text{Cu}(\text{In}, \text{Ga})\text{Se}_2$  Thin Films and Solar Cells," *The Journal of Physical Chemistry C*, vol. 122, no. 7, pp. 3809-3817, 2018.
- [139] D. Kreikemeyer-Lorenzo et al., "Rubidium Fluoride Post-Deposition Treatment: Impact on the Chemical Structure of the  $\text{Cu}(\text{In}, \text{Ga})\text{Se}_2$  Surface and

- CdS/Cu(In,Ga)Se<sub>2</sub> Interface in Thin-Film Solar Cells," *ACS applied materials & interfaces*, vol.10, no.43, pp.37602-37608, 2018.
- [140] M. Raghuwanshi et al., "Influence of RbF post deposition treatment on heterojunction and grain boundaries in high efficient (21.1%) Cu(In,Ga)Se<sub>2</sub> solar cells," *Nano Energy*,2019.
- [141] M. A. Contreras et al., "High efficiency Cu(In,Ga)Se<sub>2</sub> based solar cells: processing of novel absorber structures," *Proceedings of 1994 IEEE 1st World Conference on Photovoltaic Energy Conversion - WCPEC (A Joint Conference of PVSC, PVSEC and PSEC)*, vol. 1, pp. 68-75, 1994.
- [142] F. Pianezzi et al., "Unveiling the effects of post-deposition treatment with different alkaline elements on the electronic properties of CIGS thin film solar cells," *Physical Chemistry Chemical Physics*, vol. 16, no. 19, pp. 8843-8851, 2014.
- [143] M. Turcu, O. Pakma, and U. Rau, "Interdependence of absorber composition and recombination mechanism in Cu(In,Ga)(Se,S)<sub>2</sub> heterojunction solar cells," *Applied Physics Letters*, vol. 80, no. 14, pp. 2598-2600, 2002.
- [144] P. Paul, J. Bailey, G. Zapalac, and A. Arehart, "Fast CV method to mitigate effects of deep levels in CIGS doping profiles," arXiv preprint arXiv:1706.09946, 2017.
- [145] R. L. Garris, S. Johnston, J. V. Li, H. L. Guthrey, K. Ramanathan, and L. M. Mansfield, "Electrical characterization and comparison of CIGS solar cells made with different structures and fabrication techniques," *Solar Energy Materials and Solar Cells*, vol. 174, pp. 77-83, 2018.
- [146] P. K. Paul, K. Aryal, S. Marsillac, T. J. Grassman, S. A. Ringel, and A. R. Arehart, "Identifying the source of reduced performance in 1-stage-grown Cu(In, Ga)Se<sub>2</sub> solar cells," *IEEE 43rd Photovoltaic Specialists Conference (PVSC)*, pp. 3641-3644, 2016.
- [147] P. Paul et al., "Direct nm-scale spatial mapping of traps in CIGS," *IEEE Journal of Photovoltaics*, vol. 5, no. 5, pp. 1482-1486, 2015.

- [148] I.-H. Choi, C.-H. Choi, and J.-W. Lee, "Deep centers in a Cu(In,Ga)Se<sub>2</sub>/CdS/ZnO:B solar cell," *physica status solidi (a)*, vol. 209, no. 6, pp. 1192-1197, 2012.
- [149] P. Schöppe et al., "Rubidium segregation at random grain boundaries in Cu(In,Ga)Se<sub>2</sub> absorbers," *Nano Energy*, vol. 42, pp. 307-313, 2017.
- [150] H. Tampo, K. M. Kim, S. Kim, H. Shibata, and S. Niki, "Improvement of minority carrier lifetime and conversion efficiency by Na incorporation in Cu<sub>2</sub>ZnSnSe<sub>4</sub> solar cells," *Journal of Applied Physics*, vol. 122, no. 2, p. 023106, 2017.
- [151] K. Puech, S. Zott, K. Leo, M. Ruckh, and H. W. Schock, "Determination of minority carrier lifetimes in CuInSe<sub>2</sub> thin films," *Applied physics letters* vol. 69, no. 22, pp. 3375-3377, 1996.
- [152] T. M. Friedlmeier et al., "Improved photocurrent in Cu(In,Ga)Se<sub>2</sub> solar cells: from 20.8% to 21.7% efficiency with CdS buffer and 21.0% Cd-free," *IEEE Journal of Photovoltaics*, vol. 5, no. 5, pp. 1487-1491, 2015.
- [153] T. Kodalle et al., "Elucidating the Mechanism of an RbF Post Deposition Treatment in CIGS Thin Film Solar Cells," *Solar RRL*, vol.2, no.9, pp. 1800156, 2018.
- [154] S. Lin et al., "Adjustment of alkali element incorporations in Cu(In,Ga)Se<sub>2</sub> thin films with wet chemistry Mo oxide as a hosting reservoir," *Solar Energy Materials and Solar Cells*, vol. 174, pp. 16-24, 2018.
- [155] J.H. Yoon, T.Y. Seong, and J. Jeong, "Effect of a Mo back contact on Na diffusion in CIGS thin film solar cells," *Progress in Photovoltaics: Research and Applications*, vol. 21, no. 1, pp. 58-63, 2013.
- [156] K. Sakurai et al., "Adjusting the sodium diffusion into Cu(In,Ga)Se<sub>2</sub> absorbers by preheating of Mo/SLG substrates," *Journal of Physics and Chemistry of Solids*, vol. 64, no. 9-10, pp. 1877-1880, 2003.
- [157] M. Theelen, F. d. Graaf, F. Daume, N. Barreau, Z. Vroon, and M. Zeman, "Damp heat related degradation mechanisms within CIGS solar cells," *IEEE 43rd Photovoltaic Specialists Conference (PVSC)*, pp. 2292-2297, 2016.

- [158] R. Feist et al., "Examination of lifetime-limiting failure mechanisms in CIGS-based PV minimodules under environmental stress," *IEEE 33rd IEEE Photovoltaic Specialists Conference*, pp. 1-5, 2008.
- [159] A. Duchatelet, G. Savidand, R. N. Vannier, and D. Lincot, "Optimization of MoSe<sub>2</sub> formation for Cu(In,Ga)Se<sub>2</sub>-based solar cells by using thin superficial molybdenum oxide barrier layers," *Thin Solid Films*, vol. 545, pp. 94-99, 2013.
- [160] J. Pern and R. Noufi, "An investigation of stability issues of ZnO and Mo on glass substrates for CIGS solar cells upon accelerated weathering and damp heat exposures," *DOE SETP Review Meeting, Denver, CO*, vol. 4, pp. 17-19, 2007.
- [161] P. M. Salomé, V. Fjallstrom, A. Hultqvist, P. Szaniawski, U. Zimmermann, and M. Edoff, "The effect of Mo back contact ageing on Cu(In,Ga)Se<sub>2</sub> thin-film solar cells," *Progress in Photovoltaics: Research and Applications*, vol. 22, no. 1, pp. 83-89, 2014.
- [162] M. Theelen et al., "Influence of deposition pressure and selenisation on damp heat degradation of the Cu(In,Ga)Se<sub>2</sub> back contact molybdenum," *Surface and Coatings Technology*, vol. 252, pp. 157-167, 2014.
- [163] Y. Kamikawa, J. Nishinaga, S. Ishizuka, H. Shibata, and S. Niki, "Effects of Mo surface oxidation on Cu (In,Ga)Se<sub>2</sub> solar cells fabricated by three-stage process with KF postdeposition treatment," *Japanese Journal of Applied Physics*, vol. 55, no. 2, p. 022304, 2016.
- [164] R. Noufi et al., "Method of fabricating high-efficiency Cu(In,Ga)(Se,S)<sub>2</sub> thin films for solar cells," ed: Google Patents, 1995.
- [165] J. D. Walker, H. Khatri, V. Ranjan, J. Li, R. W. Collins, and S. Marsillac, "Electronic and structural properties of molybdenum thin films as determined by real-time spectroscopic ellipsometry," *Applied Physics Letters*, vol. 94, no. 14, p. 141908, 2009.
- [166] J. Li et al., "Density profiles in sputtered molybdenum thin films and their effects on sodium diffusion in cigs photovoltaics," *IEEE 37th IEEE Photovoltaic Specialists Conference*, pp. 002749-002752, 2011.



- [167] S. Lin et al., "Adjustment of alkali element incorporations in Cu(In,Ga)Se<sub>2</sub> thin films with wet chemistry Mo oxide as a hosting reservoir," *Solar Energy Materials and Solar Cells*, vol. 174, pp. 16-24, 2018.
- [168] M. Theelen et al., "Influence of Mo/MoSe<sub>2</sub> microstructure on the damp heat stability of the Cu(In,Ga)Se<sub>2</sub> back contact molybdenum," *Thin Solid Films*, vol. 612, pp. 381-392, 2016.
- [169] M. Bodegard, K. Granath, L. Stolt, A. J. S. E. M. Rockett, and S. Cells, "The behaviour of Na implanted into Mo thin films during annealing," *Solar Energy Materials and Solar Cells*, vol. 58, no. 2, pp. 199-208, 1999.
- [170] R. V. Forest, E. Eser, B. E. McCandless, R. W. Birkmire, and J. G. Chen, "Understanding the role of oxygen in the segregation of sodium at the surface of molybdenum coated soda-lime glass," *AIChE Journal*, vol. 60, no. 6, pp. 2365-2372, 2014.
- [171] S. Suckow, "2/3-Diode Fit," ed, 2014.
- [172] D. Rudmann, "Effects of sodium on growth and properties of Cu(In,Ga)Se<sub>2</sub> thin films and solar cells," 2004.
- [173] L. Kronik, U. Rau, J.F. Guillemoles, D. Braunger, H.W. Schock, and D.Cahen, "Interface redox engineering of Cu(In,Ga)Se<sub>2</sub>-based solar cells: oxygen, sodium, and chemical bath effects," *Thin Solid Films*, vol. 361, pp. 353-359, 2000.
- [174] D. Cahen and R. Noufi, "Surface passivation of polycrystalline, chalcogenide based photovoltaic cells," *Solar Cells*, vol. 30, no. 1-4, pp. 53-59, 1991.
- [175] D. Braunger, D. Hariskos, G. Bilger, U. Rau, and H. J. T. S. F. Schock, "Influence of sodium on the growth of polycrystalline Cu(In,Ga)Se<sub>2</sub> thin films," *Thin Solid Films*, vol. 361, pp. 161-166, 2000.
- [176] F. Pern et al., "A study on the humidity susceptibility of thin-film CIGS absorber," *IEEE 34th Photovoltaic Specialists Conference (PVSC)*, pp. 000287-000292, 2009.
- [177] N. Jiro, K. Yukiko, K. Takashi, S. Hajime, and N. Shigeru, "Degradation mechanism of Cu(In,Ga)Se<sub>2</sub> solar cells induced by exposure to air," *Japanese Journal of Applied Physics*, vol. 55, no. 7, p. 072301, 2016.

- [178] D.W. Lee et al., "Failure analysis of Cu(In,Ga)Se<sub>2</sub> photovoltaic modules: degradation mechanism of Cu(In,Ga)Se<sub>2</sub> solar cells under harsh environmental conditions," *Progress in Photovoltaics: Research and Applications*, vol. 23, no. 7, pp. 829-837, 2015.
- [179] T. J. McMahon, "Accelerated testing and failure of thin-film PV modules," *Progress in Photovoltaics: Research and Applications*, vol. 12, no. 2-3, pp. 235-248, 2004.
- [180] J. S. Britt, E. Kanto, S. Lundberg, and M. E. Beck, "CIGS Device Stability on Flexible Substrates," *IEEE 4th World Conference on Photovoltaic Energy Conference*, vol. 1, pp. 352-355, 2006.
- [181] G. Waitkins and C. J. C. R. Clark, "Selenium Dioxide: Preparation, Properties, and Use as Oxidizing Agent," *Chemical Reviews*, vol. 36, no. 3, pp. 235-289, 1945.
- [182] S. Shirakata and T. Nakada, "Time-resolved photoluminescence in Cu(In,Ga)Se<sub>2</sub> thin films and solar cells," *Thin Solid Films*, vol. 515, no. 15, pp. 6151-6154, 2007.
- [183] S. Shirakata, H. Ohta, K. Ishihara, T. Takagi, A. Atarashi, and S. Yodate, "Photoluminescence characterization of surface degradation mechanism in Cu(In, Ga)Se<sub>2</sub> thin films grown on Mo/soda lime glass substrate," *Japanese Journal of Applied Physics*, vol. 53, no. 5S1, p. 05FW11, 2014.
- [184] C. J. A. Albrecht and B. chemistry, "Joseph R. Lakowicz: Principles of fluorescence spectroscopy," vol. 390, no. 5, pp. 1223-1224, 2008.

## APPENDIX A

12/24/2018

Rightslink® by Copyright Clearance Center



RightsLink®

Home

Create Account

Help



**Title:** Impact of moisture ingress on the degradation and trap spectrum in Cu(In,Ga)Se<sub>2</sub> solar cells

**Conference Proceedings:** 2018 IEEE 7th World Conference on Photovoltaic Energy Conversion (WCPEC) (A Joint Conference of 45th IEEE PVSC, 28th PVSEC & 34th EU PVSEC)

**Author:** P. K. Paul

**Publisher:** IEEE

**Date:** June 2018

Copyright © 2018, IEEE

## LOGIN

If you're a **copyright.com** user, you can login to RightsLink using your copyright.com credentials. Already a **RightsLink user** or want to [learn more?](#)

**Thesis / Dissertation Reuse**

**The IEEE does not require individuals working on a thesis to obtain a formal reuse license, however, you may print out this statement to be used as a permission grant:**

*Requirements to be followed when using any portion (e.g., figure, graph, table, or textual material) of an IEEE copyrighted paper in a thesis:*

- 1) In the case of textual material (e.g., using short quotes or referring to the work within these papers) users must give full credit to the original source (author, paper, publication) followed by the IEEE copyright line © 2011 IEEE.
- 2) In the case of illustrations or tabular material, we require that the copyright line © [Year of original publication] IEEE appear prominently with each reprinted figure and/or table.
- 3) If a substantial portion of the original paper is to be used, and if you are not the senior author, also obtain the senior author's approval.

*Requirements to be followed when using an entire IEEE copyrighted paper in a thesis:*

- 1) The following IEEE copyright/ credit notice should be placed prominently in the references: © [year of original publication] IEEE. Reprinted, with permission, from [author names, paper title, IEEE publication title, and month/year of publication]
- 2) Only the accepted version of an IEEE copyrighted paper can be used when posting the paper or your thesis on-line.
- 3) In placing the thesis on the author's university website, please display the following message in a prominent place on the website: In reference to IEEE copyrighted material which is used with permission in this thesis, the IEEE does not endorse any of [university/educational entity's name goes here]'s products or services. Internal or personal use of this material is permitted. If interested in reprinting/republishing IEEE copyrighted material for advertising or promotional purposes or for creating new collective works for resale or redistribution, please go to [http://www.ieee.org/publications\\_standards/publications/rights/rights\\_link.html](http://www.ieee.org/publications_standards/publications/rights/rights_link.html) to learn how to obtain a License from RightsLink.

If applicable, University Microfilms and/or ProQuest Library, or the Archives of Canada may supply single copies of the dissertation.

BACK

CLOSE WINDOW

Copyright © 2018 [Copyright Clearance Center, Inc.](#) All Rights Reserved. [Privacy statement.](#) [Terms and Conditions.](#)  
Comments? We would like to hear from you. E-mail us at [customer care@copyright.com](mailto:customer care@copyright.com)

12/24/2018

Rightslink® by Copyright Clearance Center



RightsLink®

Home

Create Account

Help



**Title:** Investigation of traps density and position in alkali treated Cu(In,Ga)Se<sub>2</sub> thin films and solar cells

**Conference Proceedings:** 2017 IEEE 44th Photovoltaic Specialist Conference (PVSC)

**Author:** Shankar Karki

**Publisher:** IEEE

**Date:** June 2017

Copyright © 2017, IEEE

**LOGIN**

If you're a **copyright.com** user, you can login to RightsLink using your copyright.com credentials. Already a **RightsLink** user or want to [learn more?](#)

**Thesis / Dissertation Reuse**

**The IEEE does not require individuals working on a thesis to obtain a formal reuse license, however, you may print out this statement to be used as a permission grant:**

*Requirements to be followed when using any portion (e.g., figure, graph, table, or textual material) of an IEEE copyrighted paper in a thesis:*

- 1) In the case of textual material (e.g., using short quotes or referring to the work within these papers) users must give full credit to the original source (author, paper, publication) followed by the IEEE copyright line © 2011 IEEE.
- 2) In the case of illustrations or tabular material, we require that the copyright line © [Year of original publication] IEEE appear prominently with each reprinted figure and/or table.
- 3) If a substantial portion of the original paper is to be used, and if you are not the senior author, also obtain the senior author's approval.

*Requirements to be followed when using an entire IEEE copyrighted paper in a thesis:*

- 1) The following IEEE copyright/ credit notice should be placed prominently in the references: © [year of original publication] IEEE. Reprinted, with permission, from [author names, paper title, IEEE publication title, and month/year of publication]
- 2) Only the accepted version of an IEEE copyrighted paper can be used when posting the paper or your thesis on-line.
- 3) In placing the thesis on the author's university website, please display the following message in a prominent place on the website: In reference to IEEE copyrighted material which is used with permission in this thesis, the IEEE does not endorse any of [university/educational entity's name goes here]'s products or services. Internal or personal use of this material is permitted. If interested in reprinting/republishing IEEE copyrighted material for advertising or promotional purposes or for creating new collective works for resale or redistribution, please go to [http://www.ieee.org/publications\\_standards/publications/rights/rights\\_link.html](http://www.ieee.org/publications_standards/publications/rights/rights_link.html) to learn how to obtain a License from RightsLink.

If applicable, University Microfilms and/or ProQuest Library, or the Archives of Canada may supply single copies of the dissertation.

BACK

CLOSE WINDOW

Copyright © 2018 [Copyright Clearance Center, Inc.](#) All Rights Reserved. [Privacy statement](#). [Terms and Conditions](#).  
Comments? We would like to hear from you. E-mail us at [customercare@copyright.com](mailto:customercare@copyright.com)

12/24/2018

Rightslink® by Copyright Clearance Center



RightsLink®

Home

Create Account

Help



**Title:** In Situ and Ex Situ Investigations of KF Postdeposition Treatment Effects on CIGS Solar Cells

**Author:** Shankar Karki

**Publication:** Photovoltaics, IEEE Journal of

**Publisher:** IEEE

**Date:** March 2017

Copyright © 2017, IEEE

**LOGIN**

If you're a **copyright.com** user, you can login to RightsLink using your copyright.com credentials. Already a **RightsLink** user or want to [learn more?](#)

**Thesis / Dissertation Reuse**

**The IEEE does not require individuals working on a thesis to obtain a formal reuse license, however, you may print out this statement to be used as a permission grant:**

*Requirements to be followed when using any portion (e.g., figure, graph, table, or textual material) of an IEEE copyrighted paper in a thesis:*

- 1) In the case of textual material (e.g., using short quotes or referring to the work within these papers) users must give full credit to the original source (author, paper, publication) followed by the IEEE copyright line © 2011 IEEE.
- 2) In the case of illustrations or tabular material, we require that the copyright line © [Year of original publication] IEEE appear prominently with each reprinted figure and/or table.
- 3) If a substantial portion of the original paper is to be used, and if you are not the senior author, also obtain the senior author's approval.

*Requirements to be followed when using an entire IEEE copyrighted paper in a thesis:*

- 1) The following IEEE copyright/ credit notice should be placed prominently in the references: © [year of original publication] IEEE. Reprinted, with permission, from [author names, paper title, IEEE publication title, and month/year of publication]
- 2) Only the accepted version of an IEEE copyrighted paper can be used when posting the paper or your thesis on-line.
- 3) In placing the thesis on the author's university website, please display the following message in a prominent place on the website: In reference to IEEE copyrighted material which is used with permission in this thesis, the IEEE does not endorse any of [university/educational entity's name goes here]'s products or services. Internal or personal use of this material is permitted. If interested in reprinting/republishing IEEE copyrighted material for advertising or promotional purposes or for creating new collective works for resale or redistribution, please go to [http://www.ieee.org/publications\\_standards/publications/rights/rights\\_link.html](http://www.ieee.org/publications_standards/publications/rights/rights_link.html) to learn how to obtain a License from RightsLink.

If applicable, University Microfilms and/or ProQuest Library, or the Archives of Canada may supply single copies of the dissertation.

BACK

CLOSE WINDOW

Copyright © 2018 [Copyright Clearance Center, Inc.](#) All Rights Reserved. [Privacy statement](#). [Terms and Conditions](#). Comments? We would like to hear from you. E-mail us at [customercare@copyright.com](mailto:customercare@copyright.com)

12/24/2018

Rightslink® by Copyright Clearance Center



RightsLink®

Home

Create Account

Help



**Title:** Study of Instabilities and Degradation due to Moisture Ingress in the Molybdenum back contact of Cu(In,Ga)Se<sub>2</sub>Solar Cells

**Conference Proceedings:** 2018 IEEE 7th World Conference on Photovoltaic Energy Conversion (WCPEC) (A Joint Conference of 45th IEEE PVSC, 28th PVSEC & 34th EU PVSEC)

**Author:** Grace Rajan

**Publisher:** IEEE

**Date:** June 2018

Copyright © 2018, IEEE

**LOGIN**

If you're a **copyright.com user**, you can login to RightsLink using your copyright.com credentials. Already a **RightsLink user** or want to [learn more?](#)

**Thesis / Dissertation Reuse**

**The IEEE does not require individuals working on a thesis to obtain a formal reuse license, however, you may print out this statement to be used as a permission grant:**

*Requirements to be followed when using any portion (e.g., figure, graph, table, or textual material) of an IEEE copyrighted paper in a thesis:*

- 1) In the case of textual material (e.g., using short quotes or referring to the work within these papers) users must give full credit to the original source (author, paper, publication) followed by the IEEE copyright line © 2011 IEEE.
- 2) In the case of illustrations or tabular material, we require that the copyright line © [Year of original publication] IEEE appear prominently with each reprinted figure and/or table.
- 3) If a substantial portion of the original paper is to be used, and if you are not the senior author, also obtain the senior author's approval.

*Requirements to be followed when using an entire IEEE copyrighted paper in a thesis:*

- 1) The following IEEE copyright/ credit notice should be placed prominently in the references: © [year of original publication] IEEE. Reprinted, with permission, from [author names, paper title, IEEE publication title, and month/year of publication]
- 2) Only the accepted version of an IEEE copyrighted paper can be used when posting the paper or your thesis on-line.
- 3) In placing the thesis on the author's university website, please display the following message in a prominent place on the website: In reference to IEEE copyrighted material which is used with permission in this thesis, the IEEE does not endorse any of [university/educational entity's name goes here]'s products or services. Internal or personal use of this material is permitted. If interested in reprinting/republishing IEEE copyrighted material for advertising or promotional purposes or for creating new collective works for resale or redistribution, please go to [http://www.ieee.org/publications\\_standards/publications/rights/rights\\_link.html](http://www.ieee.org/publications_standards/publications/rights/rights_link.html) to learn how to obtain a License from RightsLink.

If applicable, University Microfilms and/or ProQuest Library, or the Archives of Canada may supply single copies of the dissertation.

BACK

CLOSE WINDOW

Copyright © 2018 [Copyright Clearance Center, Inc.](#) All Rights Reserved. [Privacy statement](#). [Terms and Conditions](#). Comments? We would like to hear from you. E-mail us at [customercare@copyright.com](mailto:customercare@copyright.com)

12/24/2018

Rightslink® by Copyright Clearance Center



RightsLink®

Home

Create Account

Help



**Title:** Characterization of Electronic Defects in RbF treated CIGS Solar cells

**Conference Proceedings:** 2018 IEEE 7th World Conference on Photovoltaic Energy Conversion (WCPEC) (A Joint Conference of 45th IEEE PVSC, 28th PVSEC & 34th EU PVSEC)

**Author:** Shankar Karki

**Publisher:** IEEE

**Date:** June 2018

Copyright © 2018, IEEE

**LOGIN**

If you're a **copyright.com** user, you can login to RightsLink using your copyright.com credentials. Already a **RightsLink** user or want to [learn more?](#)

**Thesis / Dissertation Reuse**

**The IEEE does not require individuals working on a thesis to obtain a formal reuse license, however, you may print out this statement to be used as a permission grant:**

*Requirements to be followed when using any portion (e.g., figure, graph, table, or textual material) of an IEEE copyrighted paper in a thesis:*

- 1) In the case of textual material (e.g., using short quotes or referring to the work within these papers) users must give full credit to the original source (author, paper, publication) followed by the IEEE copyright line © 2011 IEEE.
- 2) In the case of illustrations or tabular material, we require that the copyright line © [Year of original publication] IEEE appear prominently with each reprinted figure and/or table.
- 3) If a substantial portion of the original paper is to be used, and if you are not the senior author, also obtain the senior author's approval.

*Requirements to be followed when using an entire IEEE copyrighted paper in a thesis:*

- 1) The following IEEE copyright/ credit notice should be placed prominently in the references: © [year of original publication] IEEE. Reprinted, with permission, from [author names, paper title, IEEE publication title, and month/year of publication]
- 2) Only the accepted version of an IEEE copyrighted paper can be used when posting the paper or your thesis on-line.
- 3) In placing the thesis on the author's university website, please display the following message in a prominent place on the website: In reference to IEEE copyrighted material which is used with permission in this thesis, the IEEE does not endorse any of [university/educational entity's name goes here]'s products or services. Internal or personal use of this material is permitted. If interested in reprinting/republishing IEEE copyrighted material for advertising or promotional purposes or for creating new collective works for resale or redistribution, please go to [http://www.ieee.org/publications\\_standards/publications/rights/rights\\_link.html](http://www.ieee.org/publications_standards/publications/rights/rights_link.html) to learn how to obtain a License from RightsLink.

If applicable, University Microfilms and/or ProQuest Library, or the Archives of Canada may supply single copies of the dissertation.

BACK

CLOSE WINDOW

Copyright © 2018 [Copyright Clearance Center, Inc.](#) All Rights Reserved. [Privacy statement](#). [Terms and Conditions](#).  
Comments? We would like to hear from you. E-mail us at [customercare@copyright.com](mailto:customercare@copyright.com)

12/24/2018

Rightslink® by Copyright Clearance Center



RightsLink®

Home

Create Account

Help



**Title:** Analysis of Recombination Mechanisms in RbF-Treated CIGS Solar Cells

**Author:** Shankar Karki

**Publication:** Photovoltaics, IEEE Journal of

**Publisher:** IEEE

**Date:** Jan. 2019

Copyright © 2019, IEEE

**LOGIN**

If you're a **copyright.com** user, you can login to RightsLink using your copyright.com credentials. Already a **RightsLink** user or want to [learn more?](#)

**Thesis / Dissertation Reuse**

**The IEEE does not require individuals working on a thesis to obtain a formal reuse license, however, you may print out this statement to be used as a permission grant:**

*Requirements to be followed when using any portion (e.g., figure, graph, table, or textual material) of an IEEE copyrighted paper in a thesis:*

- 1) In the case of textual material (e.g., using short quotes or referring to the work within these papers) users must give full credit to the original source (author, paper, publication) followed by the IEEE copyright line © 2011 IEEE.
- 2) In the case of illustrations or tabular material, we require that the copyright line © [Year of original publication] IEEE appear prominently with each reprinted figure and/or table.
- 3) If a substantial portion of the original paper is to be used, and if you are not the senior author, also obtain the senior author's approval.

*Requirements to be followed when using an entire IEEE copyrighted paper in a thesis:*

- 1) The following IEEE copyright/ credit notice should be placed prominently in the references: © [year of original publication] IEEE. Reprinted, with permission, from [author names, paper title, IEEE publication title, and month/year of publication]
- 2) Only the accepted version of an IEEE copyrighted paper can be used when posting the paper or your thesis on-line.
- 3) In placing the thesis on the author's university website, please display the following message in a prominent place on the website: In reference to IEEE copyrighted material which is used with permission in this thesis, the IEEE does not endorse any of [university/educational entity's name goes here]'s products or services. Internal or personal use of this material is permitted. If interested in reprinting/republishing IEEE copyrighted material for advertising or promotional purposes or for creating new collective works for resale or redistribution, please go to [http://www.ieee.org/publications\\_standards/publications/rights/rights\\_link.html](http://www.ieee.org/publications_standards/publications/rights/rights_link.html) to learn how to obtain a License from RightsLink.

If applicable, University Microfilms and/or ProQuest Library, or the Archives of Canada may supply single copies of the dissertation.

BACK

CLOSE WINDOW

Copyright © 2018 [Copyright Clearance Center, Inc.](#) All Rights Reserved. [Privacy statement.](#) [Terms and Conditions.](#) Comments? We would like to hear from you. E-mail us at [customer-care@copyright.com](mailto:customer-care@copyright.com)



## VITA

Shankar Karki  
 Department of Physics  
 Old Dominion University  
 Norfolk, VA 23529

### EDUCATION

Ph.D. in Physics, Old Dominion University, Norfolk, VA, 2019  
 M.S. in Physics, Old Dominion University, Norfolk, VA, 2014

### PROFESSIONAL EXPERIENCE

Graduate teaching assistant, Old Dominion University, 2012-2017  
 Graduate research assistant, Old Dominion University, 2012-2019

### PUBLICATIONS

- S. Karki, P. K. Paul, G. Rajan, T. Ashrafee, K. Aryal, P. Pradhan, R. W. Collins, A. Rockett, T. J. Grassman, S. A. Ringel, A. R. Arehart, and S. Marsillac, "In Situ and Ex Situ Investigations of KF Postdeposition Treatment Effects on CIGS Solar Cells," *IEEE Journal of Photovoltaics*, vol. 7, no. 2, pp. 665-669, 2017.
- S. Karki, P. Paul, G. Rajan, B. Belfore, D. Poudel, A. Rockett, E. Danilov, F. Castellano, A. Arehart, and S. Marsillac, "Analysis of Recombination Mechanisms in RbF-Treated CIGS Solar Cells," *IEEE Journal of Photovoltaics*, vol. 9, no. 1, pp. 313-318, 2019.
- J. I. Deitz, S. Karki, S. Marsillac, T. J. Grassman, and D. W. McComb, "Bandgap profiling in CIGS solar cells via valence electron energy-loss spectroscopy," *Journal of Applied Physics*, vol. 123, no. 11, p. 115703, 2018.
- G. Rajan, K. Aryal, S. Karki, P. Aryal, R. W. Collins, and S. Marsillac, "Characterization and Analysis of Ultrathin CIGS Films and Solar Cells Deposited by 3-Stage Process," vol. 2018, 2018.